

# 1 A theory of brain-computer interface learning via 2 low-dimensional control

3 J. A. Menéndez, J. A. Hennig, M. D. Golub, E. R. Oby, P. T. Sadtler, A. P. Batista, S.  
4 M. Chase, B. M. Yu, P. E. Latham  
5

6 A remarkable demonstration of the flexibility of mammalian motor systems is primates' ability to  
7 learn to control brain-computer interfaces (BCIs). This constitutes a completely novel motor behavior,  
8 yet primates are capable of learning to control BCIs under a wide range of conditions. BCIs with  
9 carefully calibrated decoders, for example, can be learned with only minutes to hours of practice. With  
10 a few weeks of practice, even BCIs with randomly constructed decoders can be learned. What are the  
11 biological substrates of this learning process? Here, we develop a theory based on a re-aiming strategy,  
12 whereby learning operates within a low-dimensional subspace of task-relevant inputs driving the local  
13 population of recorded neurons. Through comprehensive numerical and formal analysis, we demonstrate  
14 that this theory can provide a unifying explanation for disparate phenomena previously reported in  
15 three different BCI learning tasks, and we derive a novel experimental prediction that we verify with  
16 previously published data. By explicitly modeling the underlying neural circuitry, the theory reveals an  
17 interpretation of these phenomena in terms of biological constraints on neural activity.

## Introduction

18

19 A core property of mammalian motor systems is their capacity to adapt to novel environments. Through  
20 learning, mammals are able to tailor their movements to an astonishing variety of previously unexpe-  
21 rienced tasks, often needing only minutes to hours of practice to do so.<sup>1-7</sup> A particularly remarkable  
22 demonstration of this is offered by brain-computer interfaces (BCIs), where the movement of a cursor on  
23 a screen is determined by cortical activity via an external decoder.<sup>8-10</sup> Despite the unfamiliarity of this  
24 motor task, human and non-human primates are capable of learning to control BCIs under a wide range  
25 of conditions, often with little practice. With a carefully calibrated BCI decoder, proficient control of  
26 the BCI cursor can be learned after only minutes of experience.<sup>11-14</sup> But even effectively random BCI  
27 decoders can be learned as well, provided the subject undergoes a more extensive training procedure  
28 (e.g. a few weeks).<sup>15,16</sup> The purpose of this study is to develop a theory of the algorithm(s) underlying  
29 this learning process.

30 Previous models of motor cortical BCI learning have postulated that synaptic plasticity within motor  
31 cortex underlies learning a BCI.<sup>17-20</sup> Indeed, models of the synaptic connectivity required for a recurrent  
32 network to solve a BCI reaching task<sup>19</sup> and the plasticity rules by which that connectivity might be  
33 learned<sup>20</sup> can account for slow and fast learning of different BCI decoders. However, a fundamental limi-  
34 tation of synaptic plasticity is the curse of dimensionality: motor cortex contains trillions of synapses, so  
35 learning via optimization of their weights would entail solving an extremely high-dimensional optimiza-  
36 tion problem. In the best of cases – when the objective function and its gradient are explicitly known –  
37 solving such problems typically requires vast amounts of training data. In the case of BCI learning, the  
38 subject’s motor system has no explicit access to the BCI decoder, so the relationship between internal  
39 neural activity and movement – and, by extension, task performance – is unknown. This means that  
40 gradients of task performance with respect to internal biological parameters must be estimated through  
41 trial and error,<sup>20,21</sup> which is notoriously slow in high dimensional spaces.<sup>22,23</sup> Moreover, this estimation  
42 problem is made even more difficult by the biological constraints of neurons and synapses, which impose  
43 noise in the learning signals available to each synapse<sup>24</sup> and preclude synaptic plasticity rules from back-  
44 propagating gradients through the many layers of neural circuitry.<sup>25-27</sup> These considerations suggest that  
45 BCI learning by synaptic plasticity in motor cortex should be slow and highly limited.

46 Such slow and limited learning is inconsistent with the strikingly fast and flexible learning observed in  
47 many BCI experiments, where non-human primates are observed to achieve proficient control after only  
48 a single session of 10’s to 100’s of trials of practice.<sup>11-14,28</sup> Moreover, the hypothesis that motor cortex  
49 undergoes substantial synaptic changes over learning is inconsistent with two additional observations.  
50 First, the statistical structure of motor cortical activity remains remarkably conserved after learning: the  
51 repertoire of activity patterns employed for BCI control is unchanged after training on a new decoder

52 for a few hours,<sup>18,29,30</sup> and single neuron tuning to manual reaches also remains largely unchanged after  
53 performing a BCI reaching task.<sup>31</sup> Second, learning a BCI task can occur without interfering with natural  
54 limb control<sup>31</sup> (but see<sup>32</sup>).

55 Together, these observations suggest that synaptic plasticity in motor cortex is not the primary  
56 mechanism underlying BCI learning, at least for the short timescales of learning observed in the studies  
57 cited above. Instead, they suggest that the brain might take a more parsimonious learning strategy, in  
58 which (1) learning is reduced to a low-dimensional optimization problem to enable data-efficient learning,  
59 and (2) the motor cortical machinery for natural movements is kept intact.

60 A learning strategy that satisfies these two criteria is that of “re-aiming”<sup>11,12,33</sup> or “intrinsic variable  
61 learning”.<sup>34,35</sup> Under this strategy, the animal exploits the pre-existing motor cortical circuitry by learn-  
62 ing an association between intended BCI movements and internal motor commands that would otherwise  
63 be used during natural motor behavior. For example, if the BCI decoder were such that motor cortical  
64 activity generated during a *leftward* arm reach would lead to an *upward* BCI movement, then the animal  
65 would learn to employ the motor command usually reserved for *leftward* arm reaches to achieve this  
66 *upward* BCI movement (fig. 1a). This strategy satisfies criteria 1 and 2 above: the dimensionality of the  
67 learning problem is kept low because both BCI movements – typically movements of a 2D or 3D cursor –  
68 and natural motor commands<sup>36–41</sup> are low-dimensional, and the motor cortical circuit can be kept intact  
69 because the patterns of activity used for manual and BCI control are the same.

70 Previous experimental results have suggested that re-aiming can account for some<sup>34,35</sup> but not  
71 all<sup>11,12,33</sup> of the changes in motor cortical activity that occur after learning a novel BCI decoder. How-  
72 ever, this evidence has typically been interpreted through the lens of a feed-forward spatial tuning curve  
73 model of motor cortex, which does not take into account the influence of additional motor variables  
74 beyond reach direction, and omits biological constraints on the dynamics of cortical circuits. Here, we  
75 address these limitations by modeling motor cortex as a non-linear recurrently connected network of  
76 neurons and modeling re-aiming as an optimization over low-dimensional motor commands driving this  
77 network. Via simulation and analysis, we derive predictions of this theory about how neural activity  
78 and behavior should change under a pure re-aiming learning strategy, for three distinct BCI learning  
79 tasks. These predictions reveal a potentially unifying explanation of disparate phenomena observed in  
80 BCI learning.

## Results

### 2.1 Re-aiming as optimization of low-dimensional inputs to motor cortex

We begin by modeling motor cortex as a recurrent neural network driven by an upstream population of neurons (fig. 1b),

$$\tau \frac{dx_i}{dt} = -x_i + \sum_{j=1}^N W_{ij}^{\text{rec}} r_j + \sum_{j=1}^M W_{ij}^{\text{in}} u_j, \quad (1a)$$

$$r_i = \phi(x_i) = \max(0, x_i), \quad (1b)$$

where  $r_1, r_2, \dots, r_N$  and  $u_1, u_2, \dots, u_M$  denote the firing rates of the motor cortical and upstream neurons, respectively. A rectified linear activation function  $\phi(\cdot)$  is used to ensure that firing rates are strictly non-negative. We assume that firing rates are low at the start of each trial of BCI control, and thus set the initial conditions to 0,  $x_i(t=0) = 0$ . The weights  $W_{ij}^{\text{rec}}$  and  $W_{ij}^{\text{in}}$  represent the strengths of the synaptic connections between neurons within motor cortex and from the upstream population to motor cortex, respectively. To avoid making any strong commitments about the structure of these connections, we use randomly connected networks throughout the main text; simulations with other, more realistic, connectivity patterns yield similar results (see Supplementary Figure S1).

Next, we consider the upstream inputs to motor cortex,  $\{u_i(t)\}$ . Inspired by recent models and theories of motor cortex,<sup>42–46</sup> we assume that the rich intrinsic dynamics of the local motor cortical circuit suffice to generate the complex patterns of cortical activity necessary to execute a given motor behavior. Which behavior is executed at a given time is selected by an upstream “motor command” that drives motor cortex via these upstream inputs. These inputs are therefore assumed to fluctuate on a much slower timescale than the motor cortical firing rates they drive. In the analysis presented below, we take these to be constant in time; results for more complex input dynamics are presented in Supplementary Materials Section S.1.6.

Motivated by the fact that motor behaviors are generally low-dimensional,<sup>36–41</sup> we assume that the motor commands setting these inputs also have low dimensionality. We formalize this by representing the motor command as a  $K$ -dimensional vector,  $\boldsymbol{\theta} \in \mathbb{R}^K$ , constituted by  $K \ll N$  *command variables*  $\theta_1, \theta_2, \dots, \theta_K$ . These command variables could correspond to extrinsic motor variables, such as reach speed or direction, or to more abstract motor-related information, such as parameters of prepared, observed, or imagined movements. Fundamentally, we make no commitments as to the nature of these intrinsic command variables beyond them influencing the upstream activity driving motor cortex. This assumption is formalized by having the upstream firing rates depend on the low-dimensional motor

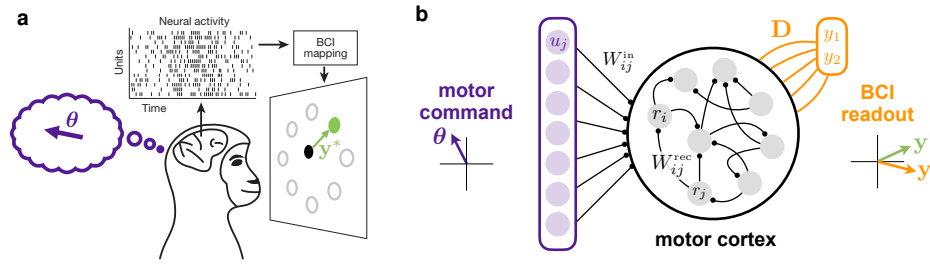


**Figure 1:** The re-aiming learning strategy.

**a.** Re-aiming strategy for BCI learning. If activity evoked by imagining a leftward planar movement moves the BCI cursor right, then the animal learns to use this motor command to move the cursor to the right. Critically, the space of imagined planar movements is low-dimensional.

**b.** Proposed model of re-aiming. Upstream inputs to motor cortex,  $u_j$ , depend on a low-dimensional motor command vector,  $\theta$  (depicted here as two-dimensional). The BCI readout,  $\mathbf{y}$ , is a 2D linear readout of motor cortical firing rates through a decoding matrix,  $\mathbf{D}$ . Re-aiming is formalized as identifying the motor command,  $\theta$ , that ensures the BCI readout gets as close as possible to a given target readout,  $\mathbf{y}^*$  (cf. equation 4).

107 command via a set of encoding weights,  $U_{ij}$ ,

$$u_i(\boldsymbol{\theta}) = \phi \left( \sum_{j=1}^K U_{ij} \theta_j \right). \quad (2)$$

108 The rectified linear activation function,  $\phi(\cdot)$ , is again used here to enforce non-negative firing rates. For  
109 simplicity, we set the encoding weights  $U_{ij}$  randomly.

110 During BCI control, motor cortical firing rates,  $\mathbf{r}(t) = (r_1(t) \cdots r_N(t)) \in \mathbb{R}^N$ , are directly translated  
111 to behavior of an external effector (e.g. a cursor on a screen) through a linear readout,

$$\mathbf{y}(t) = \mathbf{D}(\mathbf{r}(t) - \mathbf{c}). \quad (3)$$

112 As is typically done in BCI experiments with linear decoders, we include a constant offset  $\mathbf{c}$  to center  
113 the strictly positive firing rates (see Methods Section 4.8). The readout,  $\mathbf{y}(t)$ , determines behavior in  
114 the BCI task by specifying, for example, the position<sup>47,48</sup> or velocity<sup>11,12,14,15,49</sup> of a cursor. Regardless  
115 of how exactly how the readout maps to cursor movements, performing a given task (e.g. moving the  
116 cursor towards a target) demands a particular sequence of target readouts, which we denote by  $\mathbf{y}^*(t)$ .  
117 A subject learning to perform a BCI task with a given decoder must therefore find a way to generate  
118 motor cortical activity patterns that will produce these target readouts.

119 Our hypothesis is that subjects do so only by optimizing the upstream motor commands,  $\boldsymbol{\theta}$ . A key  
120 feature of this learning strategy is that it reduces the dimensionality of the learning problem. That  
121 reduction can be huge: from the number of synaptic weights to the number of command variables  
122 specifying the motor command,  $K$  – a factor that can easily reach  $10^9$ . Moreover, not all  $K$  command  
123 variables need to be optimized – we will argue below that, in certain settings, subjects may be optimizing  
124 only a subset of the task-relevant command variables, sometimes as few as 2. Such a reduction in the  
125 number of optimized parameters allows efficient learning in the absence of gradient information. However,

126 it also limits the space of available solutions to the BCI task. Here we develop a formal theory of re-aiming  
127 to understand the implications of these limitations, and, importantly, show that they are consistent with  
128 empirical data.

129 We analyze a simplified model of re-aiming in which the motor command,  $\theta$ , is optimized to produce  
130 a target readout,  $\mathbf{y}^*$ , at a single endpoint time,  $t_{\text{end}}$ ,

$$\hat{\theta}(\mathbf{y}^*) = \arg \min_{\theta_1, \theta_2, \dots, \theta_{\tilde{K}}} \|\mathbf{y}(t_{\text{end}}; \theta) - \mathbf{y}^*\|^2 + \frac{\gamma}{M} \sum_{i=1}^M u_i(\theta)^2. \quad (4)$$

131 The vector  $\mathbf{y}(t_{\text{end}}; \theta)$  is the BCI readout at time  $t_{\text{end}}$  resulting from driving the model motor cortical net-  
132 work with the motor command  $\theta$ . The integer  $\tilde{K}$  denotes the number of command variables optimized by  
133 re-aiming; for simplicity, the remaining command variables that are not optimized,  $\theta_{\tilde{K}+1}, \theta_{\tilde{K}+2}, \dots, \theta_K$ ,  
134 are set to 0. The second term on the right-hand side quantifies the metabolic cost of the upstream  
135 firing rates induced by the motor command,  $\theta$ , included in the objective function to ensure that only  
136 biologically plausible solutions are allowed.

137 Solutions to equation 4 constitute a concrete hypothesis about *what* subjects learn. In the following,  
138 we analyze these optimal motor commands to evaluate whether this hypothesis is consistent with empiri-  
139 cal observations from BCI learning experiments. The question of *how* subjects might learn these optimal  
140 motor commands is left for future work. We also briefly acknowledge here that equation 4 constitutes an  
141 incomplete description of the true BCI learning problem, since controlling the BCI effector’s movement  
142 typically requires specifying a whole sequence of readouts over time (rather than at just one target time,  
143  $t_{\text{end}}$ ) and relies on closed-loop feedback of the effector’s state.<sup>50–52</sup> That said, this simplified model of  
144 re-aiming will prove useful to intuit general principles of the re-aiming learning strategy, which, as we  
145 show in Supplementary Materials Section S.1.6, extend to more complex settings such as closed-loop  
146 control. After all, being able to produce a target readout at a fixed future time is, loosely, a pre-requisite  
147 to solving the full closed-loop control problem.

## 148 2.2 Re-aiming implies neural constraints on short-term learning

149 We begin by modelling the BCI experiment designed by Sadtler et al. (2014).<sup>14</sup> In this task, subjects learn  
150 to perform center-out movements with a 2D cursor on a screen, with the velocity of the cursor controlled  
151 by the readout from a linear BCI decoder, as in equation 3. Prior to learning, subjects first engage in  
152 a “calibration task”, in which neural activity is recorded while the subject passively views center-out  
153 cursor movements to eight radial targets (fig. 2a). Sadtler et al. observed that neural responses to these  
154 stimuli occupy a low-dimensional subspace, termed the “intrinsic manifold”. This subspace – identified  
155 via linear dimensionality reduction – is subsequently used to construct three types of BCI decoders.

156 First, a “baseline decoder” is constructed by fitting the decoding matrix,  $\mathbf{D}$ , to the neural responses

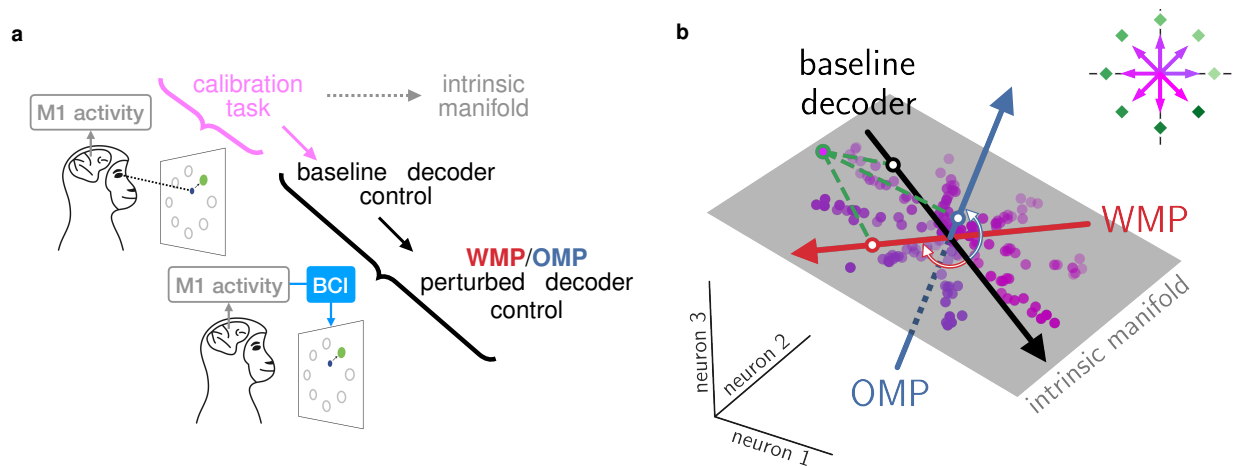


**Figure 2:** BCI learning task of Sadtler et al. (2014).

**a.** Schematic of task structure. Subjects first engage in a “calibration task” whereby they passively observe center-out cursor movements on a screen. Recorded neural activity in motor cortex is used to construct the baseline decoder and estimate the intrinsic manifold. Subjects are then instructed to perform center-out cursor movements under BCI control, first using the baseline decoder and then with a perturbed decoder, constructed by perturbing the baseline decoder. This perturbation can either preserve the baseline decoder’s alignment with the intrinsic manifold (a within-manifold perturbation, or WMP) or disrupt it (an outside-manifold perturbation, or OMP).

**b.** Low-dimensional illustration of the intrinsic manifold and its relationship to the decoders (defined in equation 3) used in this task. Colored dots represent activity patterns recorded during different trials of the calibration task, colored by the cursor velocity presented on that trial. The cursor velocities of these stimuli are depicted by color-matched arrows in the inset in the top right, with the cursor targets used in the subsequent cursor control task depicted by green diamonds. The evoked neural activity patterns reside predominantly within the two-dimensional plane depicted by the gray rectangle, the so-called intrinsic manifold. Three hypothetical one-dimensional decoders are depicted by colored arrows, labelled baseline decoder, WMP, and OMP. The corresponding component of the linear readouts,  $y_1$ , from these decoders can be visualized by projecting individual activity patterns onto the corresponding decoder vector. This is illustrated for one activity pattern marked in green, whose projections onto each of the three decoders is shown. Because this activity pattern resides close to the intrinsic manifold, it yields a large readout (i.e. far from the origin, at the intersection of the three decoders) from the baseline decoder and WMP, which are both well aligned with the intrinsic manifold. In contrast, this activity pattern’s readout through the OMP is much weaker (i.e. its projection onto this decoder is much closer to the origin), since this decoder is oriented away from the intrinsic manifold. It is important to keep in mind that this illustration is a simplified cartoon of the true task, in which the intrinsic manifold is higher-dimensional (8-12D instead of 2D) and the BCI task depends on two readouts ( $y_1, y_2$ ) rather than one.

157 from the calibration task such that these activity patterns suffice to move the cursor towards the cor-  
158 responding target in each trial. By construction, the baseline decoder is well aligned with the intrinsic  
159 manifold, such that activity patterns within this subspace can produce large readouts through this de-  
160 coder (fig. 2b). Sadtler et al. found that, with this baseline decoder, non-human primate subjects can  
161 easily perform center-out cursor movements to the targets instantly, with no learning time required.

162 Next, the decoding matrix of the baseline decoder is perturbed and the subject is prompted to perform  
163 the same center-out cursor movements with the perturbed decoder. Two types of perturbations are used,  
164 which either preserve or disrupt the baseline decoder’s alignment with the intrinsic manifold: *within-*  
165 *manifold perturbations* (WMPs) randomly re-orient the baseline decoder *within* the intrinsic manifold,  
166 whereas *outside-manifold perturbations* (OMPs) randomly re-orient the baseline decoder *outside* the  
167 intrinsic manifold (fig. 2b). WMPs alter how neural activity *within* the intrinsic manifold subspace gets  
168 mapped to readouts, such that activity patterns in this subspace suffice to perform the task. Under  
169 an OMP, on the other hand, activity patterns within the intrinsic manifold are limited in the extent  
170 of readouts they can produce, so new activity patterns *outside* of the intrinsic manifold are needed to

171 proficiently perform the task.

172 Sadtler et al. found that with 1-2 hours of practice (a few hundred trials), non-human primates  
173 can learn to successfully move the cursor to the targets with WMP decoders. In contrast, such short-  
174 term learning does not typically occur with OMP decoders, under which relatively little improvement is  
175 observed over this timespan. Here we argue that this limitation of short-term BCI learning is consistent  
176 with a re-aiming learning strategy. This low-dimensional learning strategy can account for the rapid  
177 learning achievable with WMPs, as well as the much slower learning exacted by OMPs.

178 To demonstrate this, we follow the experimental protocol outlined above, but with simulations of our  
179 motor cortical model (equations 1-2) rather than with animals. Our starting point, as with the experi-  
180 ments, is to estimate the intrinsic manifold from motor cortical firing rates recorded during the calibration  
181 task, in which the subject passively views center-out cursor movements to each of the eight radial tar-  
182 gets,  $\mathbf{y}_i^*$ . We simulated neural responses to these stimuli by driving the model network with command  
183 variables set to the cursor's constant velocity on each trial: the first two command variables,  $\theta_1$  and  $\theta_2$ ,  
184 set to the coordinates of the given target,  $\mathbf{y}_i^*$ , and the remaining command variables,  $\theta_3, \theta_4, \dots, \theta_K$ , set  
185 to 0. We then used Principal Components Analysis (PCA) to find the minimal subspace containing 95%  
186 of the variance over the resulting firing rates, which we found to be 8-dimensional (fig. 3g). We then  
187 defined the intrinsic manifold to be this subspace and used it to construct the baseline decoder and the  
188 two types of perturbed decoders (WMPs and OMPs), following the procedures of Sadtler et al. (see  
189 Methods Section 4.8).

190 Our hypothesis is that subjects learn to control the cursor by re-aiming with the same two command  
191 variables driving the calibration task responses,  $\theta_1$  and  $\theta_2$ . We thus model BCI learning by optimizing  $\theta_1$   
192 and  $\theta_2$  with respect to the re-aiming objection function (equation 4, with  $\tilde{K} = 2$ ), leaving the remaining  
193 command variables fixed to 0 as in the calibration task ( $\theta_3 = \theta_4 = \dots = \theta_K = 0$ ). As only two variables  
194 need to be optimized, learning should proceed very efficiently. The motor commands available for BCI  
195 control, however, are now severely constrained: only two command variables are free to change, and they  
196 are bounded by the metabolic cost incurred by the upstream firing rates (the second term in equation  
197 4).

198 To see how this affects performance in this BCI learning task, we simulate re-aiming for WMP and  
199 OMP decoders. For each decoder and target readout, we solve equation 4 with  $\tilde{K} = 2$  (setting  $t_{\text{end}} = 1000$   
200 ms, roughly matching the  $\sim 700$ - $1000$  ms target acquisition times observed in experiments, and setting  
201  $\gamma$  to its largest possible value guaranteeing good performance with the baseline decoder, cf. Methods  
202 Section 4.3) and drive the motor cortical network with the resulting optimal motor commands,  $\hat{\boldsymbol{\theta}}(\mathbf{y}_i^*)$ .  
203 The optimal motor commands for the baseline decoder and an example WMP and OMP are shown in  
204 fig. 3a, as vectors in  $\theta_1$ - $\theta_2$  space. The readouts produced by driving motor cortex with these motor  
205 commands,  $\mathbf{y}(t_{\text{end}}; \hat{\boldsymbol{\theta}}(\mathbf{y}_i^*))$ , are shown in adjacent panels to the right (fig. 3b), with the corresponding



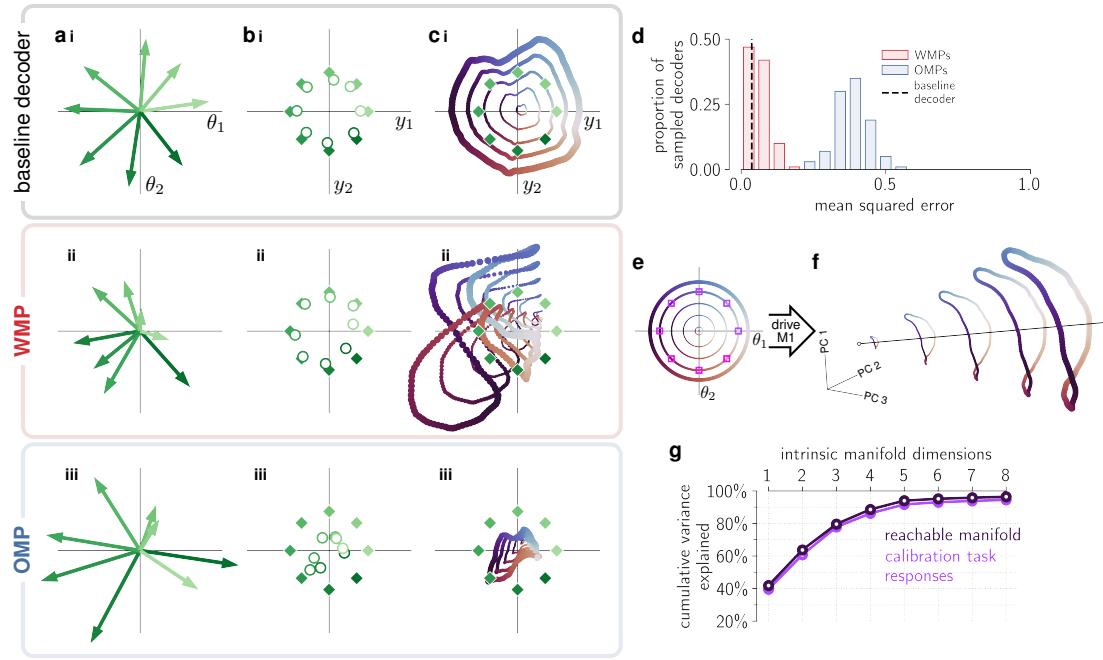


**Figure 3:** Re-aiming with two command variables suffices to learn good solutions for within- but not outside- manifold perturbations.

**a.** Optimal motor commands,  $\hat{\theta}(\mathbf{y}_i^*)$ , for the baseline decoder and one example WMP and OMP, plotted in  $\theta_1$ - $\theta_2$  space. The shade of green indexes the target readout,  $\mathbf{y}_i^*$ , that each motor command is optimized for, corresponding to the target readouts plotted in the adjacent panel (green diamonds in fig. 3b).

**b.** Readouts generated at time  $t_{\text{end}}$  by the optimal motor commands shown in the previous panel (fig. 3a), i.e.  $\mathbf{y}(t_{\text{end}}; \hat{\theta}(\mathbf{y}_i^*))$ . Green diamonds mark the eight target readouts for the center-out cursor control task, set to the directions of the eight radial cursor targets used by Sadtler et al. (2014).

**c.** Readouts from each of the reachable manifold activity patterns plotted in fig. 3f, with matched marker colors and sizes. The diamonds denote the eight target readouts as in fig. 3b. Note that the reachable readouts closest to the targets do not necessarily match the readouts produced by the optimal motor commands (fig. 3b), as the optimal motor commands are optimized to minimize the metabolic cost of the upstream input as well the readout error (cf. equation 4).

**d.** Distribution of mean squared error achieved by the optimal motor commands for 100 randomly sampled WMP's and OMP's. The mean squared error achieved by the optimal motor commands for the baseline decoder from which these perturbations are derived is marked by the vertical dashed black line. Target readouts are unit norm, so a mean squared error of 1.0 is equivalent to producing readouts at the origin.

**e.** Motor commands covering a range of angles on the  $\theta_1 - \theta_2$  plane and 5 norms,  $\|\theta\| \in \{0.1, 0.4, 0.7, 1.0, s_{\text{max}}\}$ , with  $s_{\text{max}} \approx 1.25$  (see Methods Section 4.4 for how this was chosen). The motor commands used to simulate the calibration task are indicated by the pink/purple squares. All other command variables,  $\theta_3, \theta_4, \dots, \theta_K$ , are fixed to 0.

**f.** Activity patterns in the reachable manifold at endpoint time  $t_{\text{end}} = 1000\text{ms}$ . Each ring of activity patterns is generated by the corresponding ring of color- and size- matched motor commands in the previous panel. This ensemble of  $N$ -dimensional activity patterns is projected onto its top three principal components. The black line is drawn to facilitate visualization of the 3D structure of this conical manifold. Note that the points in this plot should not be thought of as spatiotemporal trajectories of activity; rather, they depict activity patterns *at the same timepoint* generated by different motor commands.

**g.** Purple curve: cumulative variance in reachable manifold activity patterns along each intrinsic manifold dimension (equation 25). Gray curve: cumulative variance in calibration task neural responses. By construction, the intrinsic manifold contains 95% of the total variance of the calibration task neural responses (Methods Section 4.8).

206 target readouts underlaid. We find that, for the baseline decoder and WMP, most of these optimally  
 207 driven readouts reach their targets; for the OMP, on the other hand, most of them fall far short. In  
 208 fig. 3d, we repeat this simulation for 100 randomly sampled WMP and OMP decoders (see Methods  
 209 Section 4.8 for the sampling procedure, closely matching that used by Sadtler et al.), and in each case  
 210 quantify re-aiming success using the mean squared error between the optimally driven readouts and their  
 211 corresponding targets. We find that the mean squared error is consistently lower for WMP decoders than  
 212 for OMP decoders, as it was for the representative examples in fig. 3b.

213 Why does re-aiming fail to produce good readouts through OMPs? The answer lies in the constraints  
214 the re-aiming strategy imposes on the set activity patterns available in motor cortex for BCI control. To  
215 visualize and characterize these, we consider the *reachable manifold*: the set of all motor cortical activity  
216 patterns at a fixed endpoint time,  $\mathbf{r}(t_{\text{end}}; \boldsymbol{\theta})$ , that can be reached by a motor command,  $\boldsymbol{\theta}$ , accessible  
217 by re-aiming; that is, with  $\theta_k = 0$  for all  $k > 2$  and with its norm,  $\|\boldsymbol{\theta}\|$ , constrained by the quadratic  
218 metabolic cost (which we enforce here with a hard upper bound,  $\|\boldsymbol{\theta}\| \leq s_{\text{max}}$ , set to the maximum norm  
219 of the re-aiming solutions to all sampled decoder perturbations; cf. Methods Section 4.4). A large set  
220 of these accessible motor commands are shown in fig. 3e, and the corresponding activity patterns they  
221 generated are shown to the right in fig. 3f, projected down to three dimensions via PCA. Note that, despite  
222 the accessible motor commands being two-dimensional, the reachable manifold occupies more than two  
223 dimensions of state space, due to non-linearities in the dynamics of the motor cortical network. The  
224 three-dimensional projection in fig. 3f in fact contains about 80% of the variance over the  $N$ -dimensional  
225 activity patterns, revealing that the reachable manifold occupies in a moderately low-dimensional linear  
226 subspace – higher than that of the motor commands giving rise to it (two-dimensional) but significantly  
227 lower than that of its ambient state space ( $N$ -dimensional).

228 In fact, the reachable manifold is almost completely contained within the intrinsic manifold subspace.  
229 This is quantified in fig. 3g, which reveals that the eight dimensions of the intrinsic manifold subspace  
230 capture almost 100% of the variance in reachable activity patterns. This is unsurprising given that both  
231 the activity patterns in the reachable manifold and the activity patterns evoked by the calibration task  
232 – which define the intrinsic manifold – are generated by similarly low-dimensional motor commands  $\boldsymbol{\theta}$ ,  
233 in which only two command variables ( $\theta_1, \theta_2$ ) are non-zero. Fig. 3e shows this directly by overlaying the  
234 calibration task inputs on the accessible motor commands. Ultimately, what this entails is that there are  
235 virtually no reachable activity patterns outside of the intrinsic manifold; no activity patterns outside of  
236 the intrinsic manifold are accessible via re-aiming. This explains why this learning strategy would fail  
237 to produce large readouts through OMPs.

238 To confirm this, in fig. 3c we visualize the set of readouts reachable by re-aiming, for the baseline  
239 decoder, WMP, and OMP from fig. 3a and 3b. Specifically, we plot the readouts from each of the  
240 reachable activity patterns shown in fig. 3f, providing a comprehensive visualization of the space of  
241 readouts that can be reached through each decoder by re-aiming. As expected from the fact that the  
242 reachable manifold resides solely within the intrinsic manifold, we see that the readouts reachable under  
243 the baseline and WMP decoders cover a wider area than those reachable under the OMP decoder. The  
244 targets are thus enclosed by the baseline and WMP decoder reachable readouts, but remain out of reach  
245 of the OMP decoder. The re-aiming learning strategy therefore fails to solve the task with this OMP  
246 decoder, as none of the motor commands accessible under this learning strategy can reach the target  
247 readouts.

248 We conclude that re-aiming with only two variables ( $\theta_1$  and  $\theta_2$ ) can lead to successful BCI control  
249 with WMP decoders but not with OMP decoders. This offers an explanation for why only WMPs are  
250 learnable on the short timescale of a single experimental session. Because such low-dimensional re-aiming  
251 can't succeed for OMPs, subjects must resort to an alternative – and presumably higher-dimensional –  
252 learning strategy, explaining why it requires substantially more training to learn these.<sup>16</sup>

### 253 **2.3 Re-aiming predicts biases in short-term learning**

254 A close look at fig. 3c reveals an important difference between the baseline and the WMP decoders:  
255 the readouts reachable with the baseline decoder cover the readout space symmetrically while those  
256 reachable with the WMP decoder do not (compare figs. 3ci and 3cii). In other words, larger readouts  
257 are reachable in some directions than in others. Such biases in reachable readouts are not unique to this  
258 particular WMP decoder; fig. 4a reveals similar asymmetries in the readouts reachable through three  
259 other representative WMP decoders.

260 The direction of this bias is moreover predictable: typically, the largest reachable readouts are in the  
261 direction of  $\mathbf{D}\bar{\mathbf{r}}$  (arrow overlaid on each plot), where  $\bar{\mathbf{r}}$  is the centroid of the reachable manifold. This bias  
262 arises because of the non-negativity of firing rates, which permits the population firing rate,  $\mathbf{r}$ , to grow  
263 widely away from the origin, but shrink towards the origin only up to a point, where it is truncated by  
264 the non-negativity. It is this property that endows the reachable manifold its conical structure (fig. 3f),  
265 whose centroid,  $\bar{\mathbf{r}}$ , dictates the direction in which firing rates can grow the most under the re-aiming  
266 strategy. The projection of this direction through a given decoder,  $\mathbf{D}\bar{\mathbf{r}}$ , thus determines the direction  
267 in which the largest readouts can be reached by re-aiming (see Supplementary Materials Section S.1.2  
268 for a more detailed analysis). In Supplementary Figure S1d, we show that – as long as firing rates  
269 are constrained to be non-negative (Supplementary Materials Section S.1.3) – this bias arises across a  
270 large variety of motor cortical connectivity patterns and dynamics, suggesting that it is an unavoidable  
271 consequence of the re-aiming learning strategy. The absence of such a bias in experimental data would  
272 therefore provide strong evidence against this theory of BCI learning.

273 To quantify this experimental prediction, we used the “cursor progress” metric,  $\rho$ , introduced by  
274 Golub et al. (2018) to measure the degree to which a given readout,  $\mathbf{y}$ , pushes the BCI cursor in a given  
275 target direction,  $\mathbf{y}^*$ ,

$$\rho(\mathbf{y}; \mathbf{y}^*) = \mathbf{y} \cdot \frac{\mathbf{y}^*}{\|\mathbf{y}^*\|}. \quad (5)$$

We then predict the maximum achievable cursor progress in each target direction,

$$\rho^{\max}(\mathbf{y}^*) = \max_{\theta_1, \theta_2} \rho(\mathbf{y}(t_{\text{end}}; \boldsymbol{\theta}); \mathbf{y}^*), \quad (6)$$

subject to  $\|\boldsymbol{\theta}\| \leq s_{\max}$ ,

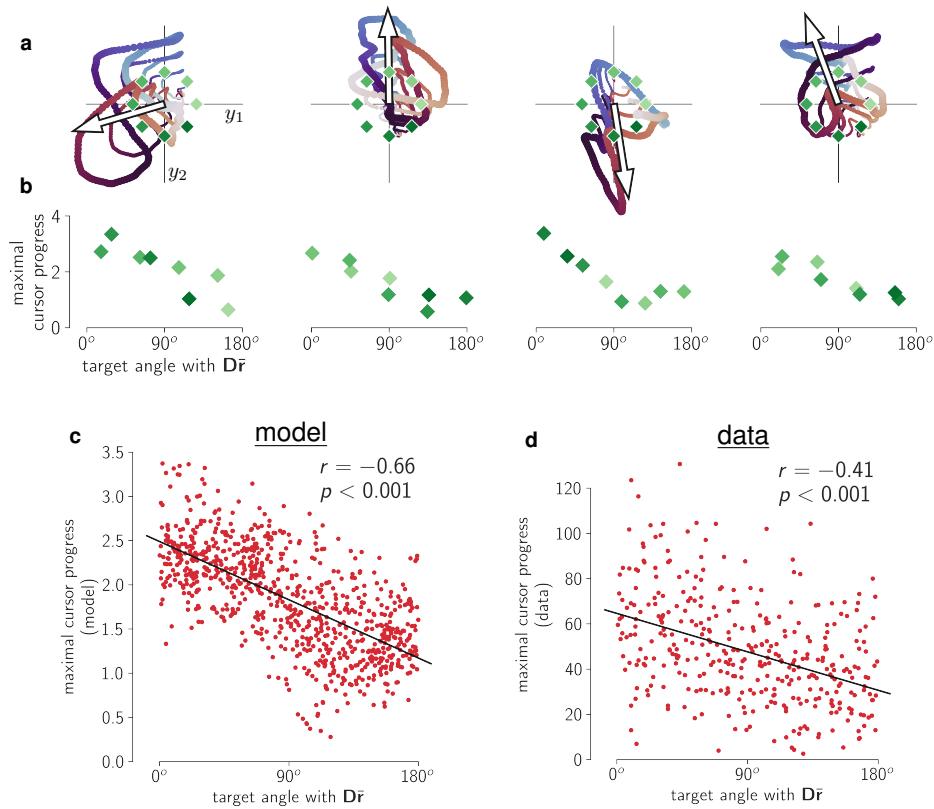


**Figure 4:** Re-aiming predicts biases in readouts after short-term learning of within-manifold perturbation (WMP) decoders.

**a.** Readouts reachable through four representative WMP decoders, using the same color conventions as in fig. 3c. In each case, the four loops correspond to four distinct motor command norms, chosen to aid visualization. The leftmost panel corresponds to the example WMP decoder shown in fig. 3cii. The projection of the reachable manifold centroid,  $D\bar{\mathbf{r}}$ , is overlaid as an open arrow, arbitrarily rescaled for visibility.

**b.** Maximal cursor progress in each target direction as a function of angle with  $D\bar{\mathbf{r}}$ , for the four example WMP decoders in panel a.

**c.** Maximal cursor progress in each target direction as a function of angle with  $D\bar{\mathbf{r}}$ , for all 100 sampled WMPs. As was done for the experimental data in the next panel, the reachable manifold centroid,  $\bar{\mathbf{r}}$ , is estimated using simulated mean firing rates during baseline decoder control (see Methods Section 4.6). A total of 8 target directions  $\times$  100 sampled WMPs = 800 points are plotted.

**d.** Maximal cursor progress in each target direction as a function of angle with  $D\bar{\mathbf{r}}$ , for all 46 sessions of WMP learning across three monkeys. Maximal cursor progress is estimated using the average cursor progress over the 50 contiguous trials with lowest acquisition times. The reachable manifold centroid,  $\bar{\mathbf{r}}$ , is estimated using mean firing rates over trials of baseline decoder control (see Methods Section 4.6). A total of 8 target directions  $\times$  46 experimental sessions = 368 points are plotted.

276 where, as above,  $\theta_1$  and  $\theta_2$  are the two command variables optimized by re-aiming and  $s_{\max}$  is the bound  
 277 on motor command norms imposed by the metabolic constraint in equation 4 (cf. Methods Section  
 278 4.4). In fig. 4b, we plot this maximal cursor progress for each target readout,  $\rho^{\max}(\mathbf{y}_i^*)$ , as a function  
 279 of the target readout's angle from  $D\bar{\mathbf{r}}$ , for each of the four example WMPs. The negative correlation  
 280 in each case confirms our above observation: higher cursor progress is reachable in target directions  
 281 more aligned with  $D\bar{\mathbf{r}}$ . In fig. 4c, we plot the maximal cursor progress in each target direction for all  
 282 100 sampled WMP decoders, revealing a statistically significant negative correlation across all sampled  
 283 decoders (Pearson  $r = -0.66, p < .001$ ).

284 Does this predicted negative correlation also hold in the empirical data? To test this, we estimated  
 285 the maximal cursor progress and reachable manifold centroid in each experimental session of WMP

control. Maximal cursor progress in each target direction,  $\rho^{\max}(\mathbf{y}_i^*)$ , was estimated using the average  
cursor progress in that target direction over the 50 contiguous WMP control trials with fastest target  
acquisition times (see Methods Section 4.6). The reachable manifold centroid,  $\bar{\mathbf{r}}$ , was estimated using  
mean motor cortical firing rates during the block of baseline decoder control (see Methods Section 4.6),  
which in our model is highly correlated with the true reachable manifold centroid. We then replicated  
fig. 4c by plotting the empirically measured maximal cursor progress for each target direction as a  
function of the angle between the target direction and  $\mathbf{D}\bar{\mathbf{r}}$ , using our empirical estimates of maximal  
cursor progress and  $\bar{\mathbf{r}}$  from each experimental session. The data over all sessions are plotted in fig. 4d,  
revealing a significant negative correlation (Pearson  $r = -0.41, p < .001$ ) akin to that observed in our  
model. This confirms the existence of a statistically significant bias in the same direction predicted by  
our model of re-aiming.

## 2.4 Long-term BCI learning by generalized re-aiming

Although non-human primates struggle to control OMP decoders within a single experimental session  
(a few hundred trials),<sup>14</sup> they can in fact learn to do so when trained over multiple days (thousands of  
trials).<sup>16</sup> In this long-term learning paradigm, new motor cortical activity patterns emerge that allow the  
subjects to achieve good performance with OMP decoders. Could re-aiming play a role in the emergence  
of novel activity patterns over these longer timescales?

Since re-aiming with the two command variables evoked by the calibration task,  $\theta_1$  and  $\theta_2$ , is not  
sufficient to produce the activity patterns required for OMP control, additional command variables will  
be required. We refer to a learning strategy that uses additional command variables as “generalized  
re-aiming”, and demonstrate below that this strategy can in fact achieve good performance with OMP  
decoders. Moreover, it can account for why learning is slower for these decoders: the search for optimal  
motor commands takes place in a higher-dimensional space beyond the narrow 2D space of command  
variables evoked by the calibration task.

To simulate generalized re-aiming, we simply increase the number of command variables used for  
re-aiming,  $\tilde{K}$ , and solve the resulting  $\tilde{K}$ -dimensional optimization problem in equation 4. In fig. 5a we  
plot the mean squared error achieved by the re-aiming solutions for each OMP decoder for each value  
of  $\tilde{K}$ . We find that as  $\tilde{K}$  increases, a lower mean squared error is achieved, demonstrating that this  
learning strategy can be effective for OMP learning. For this model motor cortical network, re-aiming  
with about 15-20 command variables suffice to achieve a mean squared error as low as that achievable  
with WMP decoders using  $\tilde{K} = 2$ . For other motor cortical models with different connectivity, fewer than  
10 command variables suffice (Supplementary Figure S1e). These values of  $\tilde{K}$  comfortably fall in the  
range of the total number of extrinsic motor variables known to influence motor cortical activity.<sup>53-59</sup>  
However, they may be too high for naïve gradient-free optimization to succeed in solving equation 4

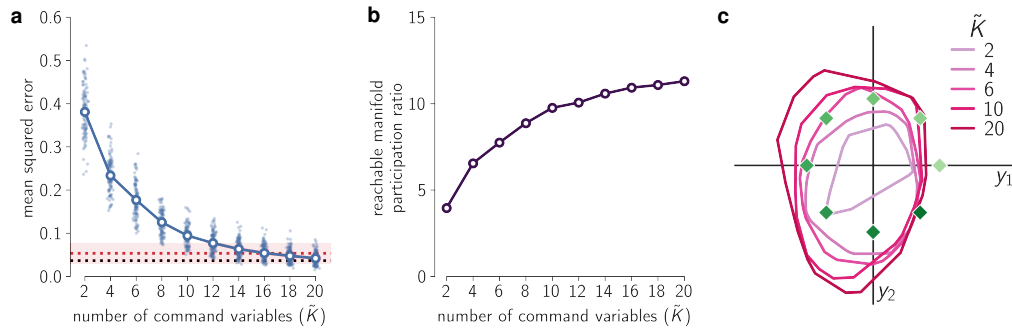


**Figure 5:** Generalized re-aiming produces good solutions for outside-manifold perturbations (OMPs).

**a.** Mean squared error achieved by generalized re-aiming solutions for all sampled OMP decoders, plotted as a function of the number of command variables used for re-aiming,  $\tilde{K}$ . Lighter blue points show the mean squared error for individual OMP decoders, darker open circles show the median over all sampled OMPs. For reference, dotted horizontal lines show the mean squared error achieved by re-aiming solutions with  $\tilde{K} = 2$  for the baseline decoder (black) and for WMP decoders (red); for WMP decoders, the median over all sampled decoders is shown with shading marking the upper and lower quartiles (corresponding to the values plotted in the red histogram in fig. 3d).

**b.** Participation ratio of the reachable manifold covariance (a measure of the effective dimensionality of the reachable manifold; see Methods Section 4.4, equation 16) as a function of the number of command variables used for re-aiming,  $\tilde{K}$ .

**c.** Convex hull of OMP readouts reachable with different number of command variables,  $\tilde{K}$ , for the same OMP decoder shown in fig. 3c. The innermost ring ( $\tilde{K} = 2$ ) corresponds to the convex hull of the reachable readouts plotted in fig. 3ciii.

320 under biological limitations (e.g. on memory, motivation, and noise), which might explain why primates  
 321 seem to only be able to learn to control OMP decoders when provided with a structured incremental  
 322 training paradigm.<sup>16</sup>

323 Why generalized re-aiming works can be understood by looking at how increasing  $\tilde{K}$  changes the  
 324 reachable manifold. A larger number of learnable command variables permits a more diverse set of  
 325 upstream inputs, which in turn implies that a more diverse set of activity patterns are reachable by re-  
 326 aiming. This diversity is quantified in fig. 5b by the participation ratio of the covariance of the reachable  
 327 manifold (see Methods Section 4.4, equation 17). The participation ratio measures the extent to which  
 328 variability is spread out over many dimensions (high participation ratio) or concentrated to only a few  
 329 (low participation ratio).<sup>60</sup> We find that as  $\tilde{K}$  rises, the participation ratio of the reachable manifold  
 330 covariance increases, indicating it occupies more and more dimensions of state space. That said, the  
 331 participation ratio does begin to saturate at around  $\tilde{K} = 20$ , reflecting the fact that the reachable  
 332 manifold is ultimately limited by the smooth dynamics of the motor cortical network.

333 This expansion in the reachable manifold leads to the inclusion of new activity patterns that are  
 334 useful for OMP control. We can see this in fig. 5c, which shows the readouts reachable through the same  
 335 OMP visualized in fig. 3ciii. The readouts reachable under different values of  $\tilde{K}$  are plotted with different  
 336 colors, revealing how re-aiming with a larger number of command variables allows the target readouts to  
 337 be reached. As the reachable manifold expands, more and more activity patterns occupying dimensions  
 338 relevant to OMP control become reachable, such that a wider set of readouts become reachable.

## 339 2.5 Illusory credit assignment by generalized re-aiming

340 We now turn to a different class of BCI decoder perturbation, termed the credit assignment rotation  
341 perturbation.<sup>61</sup> We can think of the readout from a linear BCI decoder (equation 3) as summing together  
342 the  $N$  columns of the decoding matrix  $\mathbf{D}$  (termed the “decoding vectors”), each one weighted by the  
343 activity of the corresponding neuron (fig. 6a, top). Under a credit assignment rotation perturbation,  
344 the decoding vectors of a random subset of neurons (the “rotated neurons”) are rotated by a given  
345 angle (fig. 6a, bottom). Errors induced by this decoder perturbation can be corrected by adjusting  
346 only the responses of the rotated neurons, while leaving the responses of the “non-rotated” neurons  
347 unchanged. But doing so requires solving the so-called credit assignment problem:<sup>62</sup> identifying which  
348 neurons’ decoding vectors were rotated – a tall order given that the subject has no explicit knowledge  
349 about the BCI decoder or the few motor cortical neurons (among millions) it records from.

350 Despite these challenges, multiple studies have shown that non-human primates can learn to control  
351 such decoder perturbations.<sup>11,12,61</sup> These studies used the same 2D cursor control task described above  
352 (fig. 2a), in which subjects first control a BCI cursor using a baseline decoder fit to motor cortical activity  
353 recorded during a calibration task, and then learn to control the cursor using a perturbed decoder with  
354 rotated decoding vectors. Subjects’ motor cortical activity changes after learning to control the perturbed  
355 decoder, and this can be characterized by the change in neurons’ tuning to cursor direction during BCI  
356 control with the baseline and perturbed decoders. Each of these studies found that, after learning,  
357 tuning curves of both rotated (fig. 6b) and non-rotated neurons (fig. 6c) shift in the same direction  
358 as the decoding vectors. For example, if the decoding vectors are rotated counter-clockwise, tuning  
359 curves also shift counter-clockwise. Notably, however, tuning curves of rotated neurons shift more on  
360 average than those of non-rotated neurons (compare the simulated examples in fig. 6b and fig. 6c). This  
361 observation could be interpreted to support the hypothesis that the motor system is able to solve the  
362 credit assignment problem, and in fact Hebbian synaptic learning rules have been shown to recapitulate  
363 these results by tuning individual neurons’ synapses.<sup>17</sup> Here we consider an alternate hypothesis: that  
364 these results could arise from generalized re-aiming, a global learning strategy entirely unconcerned with  
365 learning about individual neurons.

366 To test this, we follow the same procedure as above: we simulate motor cortical activity during the  
367 calibration task, use it to construct a baseline decoder, and then sample 100 random credit assignment  
368 rotation perturbations (Methods Section 4.9). Following the experimental procedures of Zhou et al.  
369 (2019), the perturbed decoders are constructed by rotating a random selection of 50% of the columns of  
370 the decoding matrix,  $\mathbf{D}$ , 75° counter-clockwise. For each decoder, we then compute the optimal motor  
371 commands for each target (equation 4) and drive the network with them to simulate center-out cursor  
372 movements learned by re-aiming. By comparing neurons’ directional tuning under the optimal motor

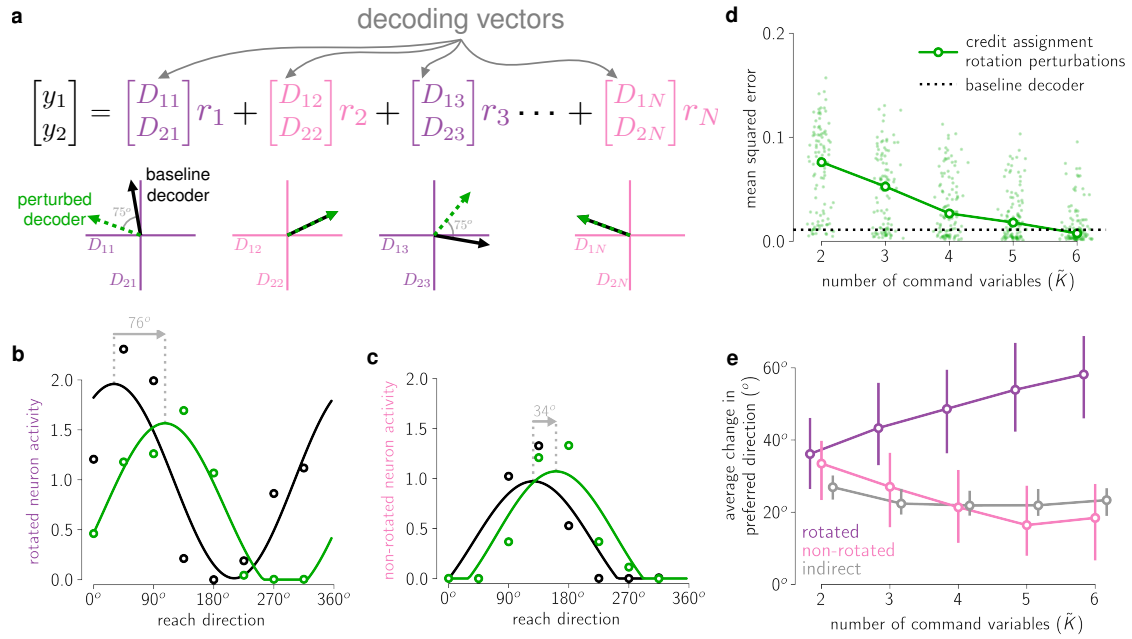


**Figure 6:** Generalized re-aiming solutions reproduce motor cortical tuning changes observed under credit assignment rotation perturbations.

**a.** A linear BCI readout (equation 3) can be interpreted as summing together columns of the decoding matrix  $D$ , each weighted by the firing rate of the corresponding neuron (the centering term  $c$  has been dropped here for simplicity). These columns are called the neurons' decoding vectors, and they are plotted on the axes below the equation. Under a credit assignment rotation perturbation, the decoding vectors of a subset of neurons (marked in purple) are rotated by a fixed angle (in this case  $75^\circ$  counter-clockwise). The neurons' decoding vectors under this perturbed decoder are shown by dashed green arrows. The neurons whose decoding vectors are rotated are termed "rotated" neurons (in purple), the rest of the neurons that are recorded by the BCI are termed "non-rotated" neurons (in pink). Neurons that are not recorded by the BCI (i.e. whose decoding vectors are just a vector of 0's, not depicted here) are termed "indirect" neurons.

**b.** Tuning curve of a representative example rotated neuron of our model, during cursor control with the baseline decoder (black) and with a credit assignment rotation perturbation (green). The dots show the time-averaged activity over  $t_{\text{end}} = 1000\text{ms}$  while the motor cortical network is driven by the re-aiming solutions for each respective decoder, using  $\tilde{K} = 2$  for the baseline decoder and  $\tilde{K} = 6$  for the perturbed decoder. Curves show tuning curves fit to these responses (Methods Section 4.9). The vertical dotted gray lines mark the preferred direction under each decoder, with an arrow labeling the change in preferred direction.

**c.** Tuning curve of a representative example non-rotated neuron of our model, under the same two decoders. All conventions exactly as in the previous panel. Note that this neuron's preferred direction changes less than that of the rotated neuron in the previous panel.

**d.** Mean squared error achieved by generalized re-aiming solutions for 100 random credit assignment rotation perturbations, plotted as a function of the number of command variables used for re-aiming,  $\tilde{K}$ . Light green dots denote individual decoder perturbations, overlaid darker open circles denote medians over all 100 sampled decoder perturbations. Black dotted horizontal line shows the mean squared error achieved by re-aiming solutions to the unperturbed baseline decoder with  $\tilde{K} = 2$ .

**e.** Average change in preferred direction of rotated, non-rotated, and indirect neurons between simulated cursor control with the baseline decoder and each perturbed decoder, plotted as a function of the number of command variables used for re-aiming,  $\tilde{K}$ . For each decoder perturbation, the changes in preferred direction are averaged over all neurons in each sub-population, and the median over all sampled perturbations is plotted. Error bars mark the upper and lower quartiles. Positive angles indicate a counter-clockwise rotation, consistent with the direction of rotation of the decoding vectors of the rotated neurons.

373 commands for the baseline decoder and for each perturbed decoder, we can determine how directional  
374 tuning would change after learning that decoder perturbation by re-aiming.

375 Reflecting the fact that the baseline decoder is easy to learn, we used  $\tilde{K} = 2$  to compute re-aiming  
376 solutions for it. For the perturbed decoders, we simulated generalized re-aiming with 2 to 6 command  
377 variables. We find that re-aiming with about  $\tilde{K} = 6$  command variables is necessary to achieve the same  
378 performance as with the baseline decoder (fig. 6d). That said, re-aiming with only  $\tilde{K} = 2$  suffices to  
379 achieve a relatively low mean squared error (around 0.1; compare to fig. 3d), suggesting ordinary 2D



380 re-aiming could still be a viable learning strategy for this task.

381 As in the experiments, we measured neurons' preferred directions (i.e. the direction at the tuning  
382 curve peak, cf. fig. 6b and fig. 6c) under the optimal motor commands for the baseline decoder and for  
383 each perturbed decoder, and calculated each neuron's change in preferred direction. We then averaged  
384 the change in preferred direction separately over rotated and non-rotated neurons. Figure 6e shows the  
385 median of this average change in preferred direction over all sampled perturbed decoders, as a function  
386 of the number of command variables used for re-aiming,  $\tilde{K}$ . Consistent with the experimental results, we  
387 find that re-aiming leads to a global counter-clockwise shift (a *positive* change in preferred direction) in  
388 motor cortical tuning curves congruent with the rotation of the decoding vectors. Importantly, we find  
389 that generalized re-aiming with  $\tilde{K} > 2$  command variables replicates the credit assignment effects seen  
390 in the experiments, whereby the preferred directions of rotated neurons shift on average more than their  
391 non-rotated counterparts. This is true despite the fact that the credit assignment problem was never  
392 truly solved: no neuron-specific parameters were modified under this learning strategy.

393 Because we have complete access to the full population of neurons in our motor cortical model, we  
394 can also measure tuning changes in the sub-population of "indirect" neurons not recorded by the BCI  
395 (i.e. neurons whose decoding vectors in  $\mathbf{D}$  comprise a vector of 0's). These are plotted in fig. 6e with a  
396 gray line. Under generalized re-aiming, indirect neurons' tuning curves shift less on average than rotated  
397 neurons'. Whether they shift more or less than non-rotated neurons' tuning curves, on the other hand,  
398 depends on the specific value of  $\tilde{K}$  and varies considerably across different random decoder perturbations.  
399 These two results are roughly consistent with the observations of Zhou et al. (2019), who found that,  
400 in two non-human primate subjects, the average change in indirect neuron tuning curves was smaller  
401 than that measured for the rotated neurons. However, this change was larger than that measured for  
402 the non-rotated neurons in one subject but smaller in the other, consistent with the variability observed  
403 in our simulations. To our knowledge, this is the only experimental study on indirect neurons' responses  
404 before and after learning a credit assignment rotation perturbation; more studies are needed to fully test  
405 the predictions of our model.

406 An important additional prediction of our model is that credit assignment effects do not arise under  
407 ordinary 2D re-aiming (fig. 6e,  $\tilde{K} = 2$ ). This is consistent with prior modeling work showing that  
408 two-dimensional re-aiming does not suffice to account for empirically observed changes in motor cortical  
409 tuning curves after learning a credit assignment perturbation.<sup>33</sup> Interestingly, it is also consistent with  
410 recent experimental work showing that differences between rotated and non-rotated neurons seem to arise  
411 gradually over multiple days of training.<sup>61</sup> Our model suggests that this timescale of learning reflects  
412 a change in learning strategy, whereby subjects initially engage in low-dimensional re-aiming to rapidly  
413 reduce gross cursor movement errors before turning to generalized re-aiming to further refine BCI control  
414 over a longer timescale, thus giving rise to more marked credit assignment effects later in learning. We

415 briefly remark, however, that Zhou et al. did not observe changes in the preferred directions of non-  
416 rotated neurons after the first day of training. In our simulation, on the other hand, the non-rotated  
417 neuron tuning curves shift back towards their starting values under the baseline decoder as the number of  
418 re-aimed command variables increases (see decreasing pink line in fig. 6e). This discrepancy between our  
419 model and the experimental data could be explained by subjects using suboptimal re-aiming solutions  
420 deviating from the optimal one (equation 4), possibly due to the difficulty of solving this optimization  
421 problem when  $\tilde{K} > 2$ , or due to the lack of pressure to find it. This possibility is also consistent with the  
422 fact that the amount of change in preferred directions is significantly larger in our simulation ( $30 - 60^\circ$ )  
423 than in the experimental data ( $20 - 40^\circ$ ).

## 424 2.6 Operant conditioning of individual neurons by re-aiming

425 The third and final BCI task we study is the operant conditioning of individual motor cortical neurons. In  
426 this task, subjects are rewarded for simply increasing the activity of one group of motor cortical neurons  
427 over another.<sup>28,63-66</sup> The fact that primates and rodents are capable of solving such tasks is often cited  
428 as evidence that the motor system can learn to specifically modulate the responses of individual neurons.  
429 Classical models of single-neuron operant conditioning have argued that these changes happen via reward-  
430 modulated plasticity at their synapses.<sup>18,67</sup> Here we explore the extent to which these observations could  
431 instead be explained by re-aiming.

432 We begin by considering the classic operant conditioning task of Fetz and Baker (1973). In this  
433 task, the subject is rewarded for increasing the firing rate of one neuron – termed the “target” neuron –  
434 while simultaneously decreasing that of another neuron – termed the “distractor” neuron. Remarkably,  
435 Fetz and Baker found that non-human primates are often able to do this with only minutes of practice.  
436 Moreover, the identity of the target and distractor neurons could be flipped midway through a recording  
437 session, and the subject would subsequently adapt to this new target assignment within tens of minutes,  
438 increasing the activity of the neuron whose activity was previously suppressed. Could low-dimensional  
439 re-aiming explain this behavior?

440 The answer depends on the reachable manifold. If the reachable manifold contains activity patterns  
441 in which neuron  $a$  is more active than neuron  $b$ , as well as activity patterns in which neuron  $b$  is more  
442 active than neuron  $a$ , then good re-aiming solutions will exist for both target assignments. This is  
443 illustrated in fig. 7a, which shows two neurons’ endpoint firing rates,  $r_i(t_{\text{end}})$ , at various points on the  
444 reachable manifold, following the same conventions as in fig. 3f. On this plane, activity patterns below  
445 the diagonal are rewarded when neuron  $a$  is the target neuron; activity patterns above the diagonal  
446 are rewarded when neuron  $b$  is the target neuron. Because there are reachable activity patterns on  
447 both sides of the diagonal, good re-aiming solutions exist for both target assignments. We calculated  
448 optimal re-aiming solutions for each target assignment by maximizing the firing rate difference between

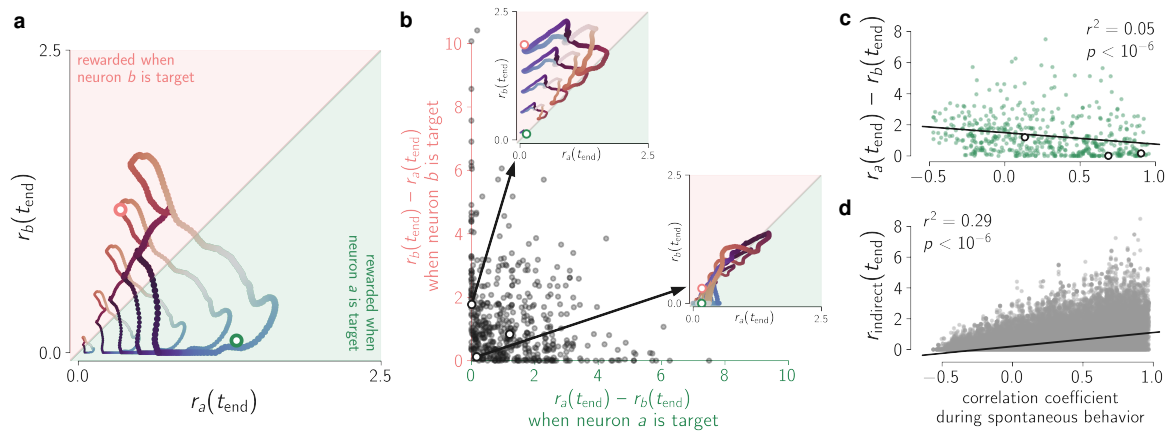


**Figure 7:** Operant conditioning of individual neurons by re-aiming.

**a.** Activity of two model neurons at various points on the reachable manifold, at  $t_{\text{end}} = 1000\text{ms}$  with  $\tilde{K} = 2$ , following the same conventions as fig. 3f. As in that figure, each ring of activity patterns is generated by the corresponding ring of color- and size- matched motor commands in fig. 3e. Activity patterns below the diagonal are ones where neuron  $a$  is more active than neuron  $b$ , satisfying the task demands when neuron  $a$  is the target neuron; the reverse holds for activity patterns above the diagonal. The green and orange open circles denote the activity patterns produced by the optimal re-aiming solutions for the two respective target assignments. Note that, due to the metabolic cost term in the re-aiming objective function, these do not necessarily correspond to the points on reachable manifold that are furthest away from the diagonal.

**b.** Difference in activity produced by re-aiming solutions for each target assignment (at time  $t_{\text{end}} = 1000\text{ms}$ , the endpoint time the re-aiming solutions were optimized for), for 500 random pairs of neurons from the same model motor cortical network used in previous simulations. Each dot corresponds to one pair of neurons. The pair of neurons shown in previous panel is marked by an open circle. Two additional examples are marked by open circles. Insets show the activity of those neuron pairs at various points on the reachable manifold, following same conventions as the previous panel.

**c.** Difference in activity (at  $t_{\text{end}} = 1000\text{ms}$ ) produced by the re-aiming solutions optimized for neuron  $a$  being the target, for the same 500 random pairs of neurons, plotted as a function of the correlation between the two neurons during simulated spontaneous behavior. The three example pairs of neurons highlighted in the previous panel are again highlighted here with open circles. A quantitatively similar trend is observed for  $r_b - r_a$  with re-aiming solutions optimized for neuron  $b$  being the target (data not shown).

**d.** Activity of indirect neurons (at  $t_{\text{end}} = 1000\text{ms}$ ) for the same neuron pairs and re-aiming solutions in previous panel, plotted as a function of correlation with neuron  $a$  during simulated spontaneous behavior. A quantitatively similar trend is observed for correlations with neuron  $b$  with re-aiming solutions optimized for neuron  $b$  being the target (data not shown).

449 the target and distractor neurons, subject to a metabolic cost (equation 29). The activity produced by  
 450 these optimal solutions are marked by the open red and green circles. These evidently satisfy each target  
 451 assignment, with neuron  $a$  achieving a higher firing rate under one re-aiming solution (green circle) and  
 452 neuron  $b$  achieving a higher firing rate under the other (red circle).

453 More generally, we can think of this plot as a particular two-dimensional projection of the reachable  
 454 manifold, specified by the pair of neurons  $a$  and  $b$ . A given neuron pair thus admits good re-aiming  
 455 solutions for this task whenever the corresponding projection of the reachable manifold covers the ap-  
 456 propriate side(s) of the diagonal. Framed in this way, it is easy to intuit that for most random pairs of  
 457 neurons a good solution will generally exist for at least one target assignment – random two-dimensional  
 458 projections of the reachable manifold are unlikely to lie exactly on the diagonal. We verify this intuition  
 459 by sampling 500 random pairs of neurons from our model motor cortical network (see Methods Section  
 460 4.10) and checking whether the re-aiming solutions for the two target assignments produce higher firing  
 461 rates for the target neuron than for the distractor neuron. The difference in the two neurons' firing rates  
 462 produced by the optimal re-aiming solutions are plotted in fig. 7b. For most neuron pairs, we see that  
 463 at least one of the two neurons can be activated more than the other. In many cases, both neurons can

464 be activated more than the other, meaning that both target assignments could be learned by re-aiming.

465 For some neuron pairs, however, the optimal re-aiming solutions do not produce a large difference  
466 in firing rates under either target assignment. These infelicitous neuron pairs are ones where the two  
467 neurons are highly correlated across all activity patterns on the reachable manifold, such that the relevant  
468 projection doesn't deviate strongly from the diagonal and no good re-aiming solutions exist. One such  
469 example is shown in the inset on the right, where the reachable manifold lies largely right on the diagonal,  
470 and thus both re-aiming solutions lead to near-0 difference in firing rates. A different kind of example is  
471 shown in the inset on the top, where the two neurons are correlated in such a way that the reachable  
472 manifold resides on only one side of the diagonal. In this case, a good re-aiming solution exists for one  
473 target assignment but not for the other. These observations reveals a tight relationship between neural  
474 correlations and operant conditioning performance: the more correlated a pair of neurons is across  
475 reachable activity patterns, the more difficult it should be to selectively activate one more than the other  
476 by re-aiming.

477 Is this prediction of our model consistent with experimental observations? Without empirical access  
478 to the reachable manifold, we cannot directly measure correlations across reachable activity patterns.  
479 But if we assume that neural activity during a prior “calibration task” is driven by the same command  
480 variables used subsequently for re-aiming – as we did in our simulation of WMP/OMP learning –, then  
481 we should expect neural correlations during this calibration task to approximately match correlations  
482 across the reachable manifold used for re-aiming. This predicts that neural correlations during a prior  
483 calibration task should be predictive of subsequent operant conditioning performance. This prediction  
484 is in fact consistent with observations from a study by Clancy et al. (2014), in which the conditioned  
485 neurons' correlation was measured during a period of spontaneous behavior (the “calibration task”) just  
486 prior to performing operant conditioning. Consistent with our model's prediction, they observed that  
487 the stronger the correlation during spontaneous behavior prior to operant conditioning, the worse the  
488 mouse tended to perform the subsequent operant conditioning task.

489 To quantify this prediction, we simulated the experiment of Clancy et al. We first simulated motor  
490 cortical activity during spontaneous behavior by driving the model motor cortical network with randomly  
491 sampled motor commands in which only two command variables,  $\theta_1$  and  $\theta_2$ , were allowed to vary (all  
492 other command variables were set to 0). We sampled 50 such motor commands to simulate 50 bouts  
493 of spontaneous activity (cf. Methods Section 4.10). For each conditioned pair of neurons, we measured  
494 their correlation coefficient over all activity across the 50 bouts, and then simulated re-aiming with the  
495 same two command variables,  $\theta_1$  and  $\theta_2$ . We quantified the efficacy of re-aiming with the firing rate  
496 difference between the target and distractor neurons at the optimized endpoint time,  $t_{\text{end}}$ . Mirroring  
497 the experimental results of Clancy et al., we find that the spontaneous activity correlations are weakly  
498 but significantly predictive of re-aiming efficacy (fig. 7c). We briefly remark here that the operant

499 conditioning task of Clancy et al. differs from our simulations in that pairs of ensembles of up to 11  
500 neurons were conditioned, rather than pairs of single neurons. In Supplementary Materials Section S.1.4,  
501 we show that the same results hold in this setting as well.

502 Finally, we consider what happens to the “indirect” neurons – neurons that are neither a target nor  
503 a distractor. Clancy et al. observed that, after learning, indirect neurons *strongly* correlated with the  
504 target neuron during spontaneous behavior remained highly active during performance of the subsequent  
505 operant conditioning task (supplementary figure 9a in<sup>65</sup>). This is consistent with our model of re-aiming,  
506 in which re-aiming tends to drive indirect neurons proportionally to their correlation with the target  
507 neuron during spontaneous behavior (fig. 7d). Our model is not, however, consistent with another  
508 observation by Clancy et al.: indirect neurons that were *moderately* correlated with the target neuron  
509 were highly active only in the early stages of learning, but by the end of learning became silent. A  
510 possible explanation for this inconsistency is that subjects re-aim with  $\tilde{K} > 2$  command variables. If  
511 spontaneous behavior during the calibration period were driven by more than 2 command variables, we  
512 would expect subjects to re-aim with more as well. Given the complexity of spontaneous behavior, this  
513 is a reasonable explanation, but we leave for future work a more comprehensive study of generalized  
514 re-aiming with  $\tilde{K} > 2$  command variables in operant conditioning tasks.

## 515 Discussion

516 In this study, we proposed and investigated the hypothesis that motor cortical BCI learning proceeds via  
517 a learning strategy we refer to as generalized re-aiming. Under this strategy, internal motor commands  
518 are manipulated to control the BCI using the same motor cortical circuitry used during natural motor  
519 behaviors. Because only a few command variables need to be manipulated to achieve this goal, learning  
520 can proceed rapidly and flexibly, and, because the motor cortical circuitry is conserved, the operation of  
521 motor cortex during natural motor control is conserved as well.

522 To study the neural and behavioral consequences of this learning strategy, we formulated a mechanistic  
523 model of re-aiming in which the internal command variables specify upstream inputs to motor cortex. By  
524 analyzing how these inputs get transformed into motor cortical activity patterns through the circuit’s  
525 nonlinear recurrent dynamics, we were able to demonstrate that re-aiming can in fact account for a  
526 wide range of experimental observations about BCI learning. This model can explain the different  
527 timescales of learning required for different BCI decoders,<sup>14,16</sup> selective changes in motor cortical tuning  
528 curves over learning,<sup>11,12,61</sup> and the seemingly astonishing ability of mammals to flexibly modulate the  
529 activity of single neurons via operant conditioning.<sup>28,63,65</sup> The model also makes a novel experimental  
530 prediction about behavioral biases during short-term learning (fig. 4), which we were able to corroborate  
531 in previously published data.<sup>14</sup> The success of this model at replicating these empirical phenomena  
532 provides an explanation in terms of the biological dynamics of neural circuits.

### 533 **3.1 Intrinsic variable learning vs. individual neuron learning**

534 An important debate in the BCI learning literature has been whether human and non-human primates are  
535 able to precisely learn and control the contribution of individual neurons to a given BCI decoder readout –  
536 the so-called “individual neuron learning” hypothesis. Several studies have been directly aimed at testing  
537 this hypothesis, leading to evidence in favor<sup>11,12,33,61</sup> and against it.<sup>34,35</sup> The alternative hypothesis is  
538 often referred to as “intrinsic variable learning”,<sup>9</sup> whereby subjects learn to control the BCI using the  
539 same constrained set of activity patterns usually used for natural motor control, unable to independently  
540 control the activity of single neurons. Our model of re-aiming is a particular formalization of this latter  
541 hypothesis, with the command variables  $\theta_1, \theta_2, \dots, \theta_{\tilde{K}}$  acting as the so-called intrinsic variables.

542 Our simulations of generalized re-aiming show that many experimental results traditionally attributed  
543 to some form of individual neuron learning<sup>17,67</sup> can be accounted for by intrinsic variable learning. In  
544 particular, even classical single neuron operant conditioning results can be reproduced by our model. Our  
545 simulations show that the dynamics of recurrently connected neural circuits are capable of generating  
546 the activity patterns required by these BCI tasks, without the need to optimize parameters specific  
547 to individual neurons or synapses.<sup>68</sup> This suggests caution in underestimating the role of macroscopic  
548 cognitive strategies<sup>69,70</sup> when observing what may look like highly specific, microscopic, changes to the  
549 activity of single neurons.

### 550 **3.2 The role of synaptic plasticity in BCI learning**

551 All the results we replicated here have been previously replicated by various models of synaptic plas-  
552 ticity within motor cortex. As argued in the introduction, however, learning by optimizing synaptic  
553 parameters entails solving an extremely high-dimensional optimization problem with no access to ex-  
554 plicit gradients, which would limit learning to be slow and brittle. Several of these previously proposed  
555 models worked around this problem by using small and simplified feed-forward models of motor cor-  
556 tex<sup>17,68</sup> or biologically implausible learning rules.<sup>19,20,71</sup> A few have demonstrated that, for simple tasks  
557 like operant conditioning, biologically plausible learning rules can in fact succeed in biologically relevant  
558 regimes despite these obstacles.<sup>18,67</sup> However, to our knowledge, none have comprehensively accounted  
559 for all three sets of experimental results considered here, including the observed effects on non-recorded  
560 neurons and the dependence of operant conditioning performance on neural correlations.

561 That said, the present study does not by any means rule out the possibility that synaptic plasticity  
562 within motor cortex may play an important role in BCI learning; rather, it reveals the surprising capa-  
563 bilities of a pure re-aiming strategy. The true mechanisms underlying BCI learning most likely comprise  
564 a mixture of both re-aiming as well as synaptic plasticity, and future work will be needed to tease apart  
565 the contributions of these two learning mechanisms and understand how they are coordinated.

566 One natural possibility is that synaptic plasticity operates on a much slower timescale than re-  
567 aiming.<sup>72</sup> This could help explain selective changes to motor cortical responses that only arise late in  
568 learning and are not replicated by our model. For example, Clancy et al. (2014) observed in their operant  
569 conditioning experiments that indirect neurons not strongly correlated with the target neuron become  
570 silent late in learning.<sup>65</sup> Ganguly et al. (2011) similarly observed that indirect neurons become less tuned  
571 to reach direction after days of practice with a given BCI decoder. Jarosiewicz et al. (2008) reported  
572 a similar effect in rotated neurons after a credit assignment rotation perturbation (although note that  
573 this effect seems to disappear when increasing the proportion of neurons rotated, see [12, 61]). These  
574 selective changes in tuning strength are not reproduced by our model of re-aiming (Supplementary Figure  
575 S5a), but previous theoretical work has demonstrated that they can be reproduced by reward-modulated  
576 Hebbian plasticity in a simplified model of motor cortex.<sup>17</sup>

577 An additional set of observations that are not well accounted for by our model come from a few  
578 recent studies demonstrating long-term changes in motor cortical activity after short-term learning.<sup>73,74</sup>  
579 In particular, Losey et al. (2024) found that motor cortical activity during baseline decoder control  
580 changed before and after learning a WMP within a single experimental session. Our model could account  
581 for this if the upstream population driving motor cortex encoded not only the motor commands relevant  
582 for control but also additional variables indexing the current behavioral context,<sup>73,75</sup> or a memory trace  
583 of the current task.<sup>74</sup>

### 584 **3.3 The “intrinsic manifold” of population activity**

585 A simple but important takeaway from this study is that the low-dimensional structure of activity in  
586 a population depends not only on the intrinsic dynamics and connectivity within that population, but  
587 also on the structure of its upstream input. The observation that population activity is confined to  
588 a low-dimensional subspace – often termed the “intrinsic manifold”<sup>14,19,76</sup> or the “neural modes”<sup>58</sup> –  
589 does not mean that the circuit connectivity prevents it from generating activity patterns outside of this  
590 subspace. It is likely that many more activity patterns outside of this subspace are accessible, but that  
591 only a low-dimensional subset are accessed by the inputs evoked by the subjects’ behavior during the  
592 recording session.<sup>60,77</sup>

593 This insight leads to a novel interpretation of the observation that outside-manifold perturbations  
594 require a longer time to learn than their within-manifold counterparts.<sup>14,16</sup> Previous models of this phe-  
595 nomenon have assumed that the longer learning time reflects the challenge of modifying the motor cortical  
596 connectivity to permit the production of activity patterns outside of the intrinsic manifold.<sup>19,20,68,71</sup> Our  
597 simulations demonstrate that this isn’t necessary, and that in many cases it may suffice to simply exploit  
598 additional input dimensions beyond those evoked by the calibration task (fig. 5a, Supplementary Figure  
599 S1e). Under this model of learning, the longer learning time required for OMPs reflects the fact that

600 these new input dimensions need to be discovered from scratch, as the calibration task provides little  
601 prior information about them.

602 Another important aspect of the intrinsic manifold that this study highlights is its nonlinear structure.  
603 Because firing rates are bounded from below by 0, activity patterns are confined to the positive orthant  
604 of state space. This constraint imposes a conical structure on population activity within the intrinsic  
605 manifold (fig. 3f, Supplementary Figure S2), which we show in Supplementary Materials Section S.1.3 is  
606 in fact necessary to account for experimentally observed behavioral biases in WMP learning. Given the  
607 strong behavioral repercussions this structure can have on BCI control, understanding and identifying  
608 such nonlinear structure in motor cortical activity may prove crucial both for understanding BCI learning  
609 as well as for designing better BCI decoders.

### 610 **3.4 The role of the calibration task in BCI learning**

611 From a more practical perspective, our theory of re-aiming highlights the role of the calibration task in  
612 BCI learning. The calibration task is typically seen as a way to calibrate the decoding parameters; that  
613 is, as a source of information for constructing the BCI *decoder*. Here we suggest that it additionally serves  
614 as a source of information for the subject itself, that is, for the BCI *learner*.<sup>78,79</sup> For example, in modeling  
615 WMP learning, we assumed that subjects re-aimed with the two command variables modulated by the  
616 calibration task; in modeling operant conditioning, we assumed that subjects re-aimed with the same  
617 command variables driving spontaneous behavior prior to the operant conditioning task. If any other  
618 two command variables had been optimized instead, the re-aiming strategy would not have succeeded  
619 in solving the task. It is the prior information provided by the calibration task that allows efficient  
620 learning by telling the subject which command variables to re-aim with. This hypothesis is consistent  
621 with various BCI learning studies demonstrating that subjects learn to control BCIs using the same  
622 patterns of activity evoked by the task they were engaged in just prior to BCI learning.<sup>18,29</sup>

623 Importantly, it predicts that the calibration task can influence subjects' ability to learn a given BCI  
624 decoder, and therefore that careful design of this task could help improve subjects' learning speed. For  
625 example, the calibration task should evoke changes in as few command variables as necessary, so that  
626 subjects subsequently re-aim by optimizing only those  $\tilde{K} < K$  command variables and avoid wasting  
627 time exploring modifications to other command variables. A prediction of our model is that learning  
628 should be slower when the calibration task evokes changes in more command variables.

### 629 **3.5 How are the re-aiming solutions learned?**

630 The theory presented here treats the question of *what* solutions subjects learn, and makes no claims  
631 about *how* they are learned and subsequently maintained. That said, a strong assumption we made in  
632 motivating the re-aiming learning strategy was that learning could operate within the low-dimensional



633 space of the command variables. It is this low dimensionality that we claimed would be critical for  
634 efficient learning; if the command variables were learned by simply optimizing the connectivity of an  
635 upstream circuit, then the limitations of learning by synaptic plasticity would also apply to learning by  
636 re-aiming.

637 One intriguing resolution to this problem would be that the command variables are stored and  
638 updated in the *activity* – rather than the *synapses* – of an upstream circuit, as in the pre-frontal cortex  
639 model of Wang et al. (2018).<sup>80</sup> In this model, a recurrent neural network implicitly stores a behavioral  
640 policy in its internal state, which, through the network’s dynamics, is updated over time as it interacts  
641 with the environment and observes which actions are rewarded in which states. A similar architecture  
642 might operate upstream of motor cortex, whereby an upstream circuit continually stores and updates a  
643 sensorimotor policy for selecting low-dimensional motor commands. This learning circuit would likely  
644 encompass additional populations beyond those directly driving motor cortex, such as the basal ganglia,  
645 which are well known to play an important role in BCI learning.<sup>64,81–83</sup>

646 We finally remark that the short timescale of WMP learning closely mirrors that of motor adaptation,  
647 in which subjects adapt their natural movements to a systematic environmental perturbation. Learning  
648 these tasks typically requires 100’s of trials of practice,<sup>2,6,7,73</sup> similar to the time it takes non-human  
649 primates to learn WMPs. Neural recordings during these tasks have suggested that changes in neural  
650 activity during motor adaptation are driven by changes in the preparatory input from dorsal pre-motor  
651 cortex to primary motor cortex.<sup>7,84</sup> Moreover, changes in the preparatory state of motor cortex (pre-  
652 sumably set by upstream inputs<sup>43,44,46</sup>) have been shown to play a critical role in motor adaptation  
653 tasks under manual control<sup>73</sup> as well as BCI control.<sup>32</sup> These results are consistent with the idea that,  
654 much like in our model of re-aiming, motor adaptation involves modifications to the inputs driving motor  
655 cortex while motor cortex itself remains unchanged. Our model of re-aiming may thus be relevant to  
656 more general and naturalistic forms of sensorimotor learning beyond BCIs.

## Methods

657

### 4.1 Motor cortical dynamics

658

659 Motor cortical activity was simulated by integrating equation 1 using a standard 4th order Runge-Kutta  
660 method with step size 0.1ms, implemented with the torchdiffeq Python package.<sup>85</sup> Reachable activity  
661 patterns,  $\mathbf{r}(t_{\text{end}}; \boldsymbol{\theta})$ , were computed by integrating this equation from the initial condition at time  $t = 0$   
662 to the endpoint time  $t = t_{\text{end}}$ , with constant inputs determined by the given motor command,  $\boldsymbol{\theta}$ , using  
663 equation 2. We assumed silent initial conditions,  $x_i(0) = 0$ , to enable a computationally efficient solution  
664 to the re-aiming objective function (see equation 12). Decoding from the reachable activity patterns using  
665 equation 3 yields the reachable readouts,  $\mathbf{y}(t_{\text{end}}; \boldsymbol{\theta})$ .

666 In all simulations in the main text, sparse random recurrent weights,  $W_{ij}^{\text{rec}}$  were used: only 10% of  
667 these weights were set to non-zero values, which were independently sampled from a zero-mean Gaussian,  
668  $\mathcal{N}(0, 1/N)$ , where  $N$  is the total number of motor cortical neurons in the network. Input weights were  
669 all sampled from a zero-mean Gaussian,  $W_{ij}^{\text{in}} \sim \mathcal{N}(0, 1/M)$ , where  $M$  is the total number of inputs.  
670 Encoding weights were sampled randomly from the standard Gaussian distribution,  $U_{ij} \sim \mathcal{N}(0, 1)$  (any  
671 normalization is taken care of by the metabolic cost term in equation 4 when computing re-aiming  
672 solutions). Other connectivity patterns are considered in Supplementary Figure S1. We used  $\tau = 200\text{ms}$ ,  
673 as in the motor cortical model of Hennequin et al. (2014). To enable efficient numerical simulation,  
674 network size was set to  $N = M = 256$ . Simulations with larger networks (up to  $N = M = 2048$  neurons)  
675 produced similar results (data not shown).

### 4.2 Computing re-aiming solutions

676

677 Concatenating the command variables into a  $\tilde{K}$ -dimensional vector that contains only the command  
678 variables being optimized,  $\tilde{\boldsymbol{\theta}} = \begin{bmatrix} \theta_1 & \theta_2 & \dots & \theta_{\tilde{K}} \end{bmatrix}$ , we can treat equation 4 as an optimization over all  
679  $\tilde{K}$ -dimensional vectors  $\tilde{\boldsymbol{\theta}}$  in  $\mathbb{R}^{\tilde{K}}$ . We can simplify this optimization problem by first analytically solving  
680 for the optimal magnitude of  $\tilde{\boldsymbol{\theta}}$ ,  $\|\tilde{\boldsymbol{\theta}}\|$ , given its direction. Once we have this optimal magnitude, all that  
681 remains is an optimization over its direction – an optimization over unit vectors on the  $\tilde{K}$ -dimensional  
682 unit hypersphere. This is a  $(\tilde{K} - 1)$ -dimensional manifold that, importantly, is bounded, so we can  
683 hope to find the optimal direction efficiently by brute-force search, avoiding the difficulties of non-convex  
684 gradient-based optimization in high dimensions.

Formally, we decompose the re-aiming optimization (equation 4) into an optimization of the norm,

$s$ , and direction,  $\tilde{\boldsymbol{\theta}}_0$ , of  $\tilde{\boldsymbol{\theta}}$ ,

$$\hat{s}, \hat{\tilde{\boldsymbol{\theta}}}_0 = \arg \min_{s, \tilde{\boldsymbol{\theta}}_0} \|\mathbf{y}(t_{\text{end}}; s\tilde{\boldsymbol{\theta}}_0) - \mathbf{y}^*\|^2 + \frac{\gamma}{M} \sum_{i=1}^M u_i(s\tilde{\boldsymbol{\theta}}_0)^2, \quad (7)$$

subject to  $s > 0$ ,  $\|\tilde{\boldsymbol{\theta}}_0\| = 1$ .

685 We can analytically solve for the optimal magnitude,  $\hat{s}$ , by exploiting two simplifications afforded to us  
 686 by the rectified linear activation function  $\phi(\cdot)$  of the motor cortical dynamics (equation 1b). The first is  
 687 the scale-invariance of the activation function ( $\phi(sx) = s\phi(x)$  for any  $s \geq 0$ ), which accordingly endows  
 688 the motor cortical dynamics with scale invariance,

$$\mathbf{r}(t; s\boldsymbol{\theta}) = s\mathbf{r}(t; \boldsymbol{\theta}), \quad s > 0, \quad (8)$$

689 whenever  $x_i(0) = 0$  (see Supplementary Materials Section S.2.1 for a formal proof), which we assumed  
 690 to be the case in our simulations. The second simplification is to approximate the quadratic cost term  
 691 by its large  $M$  limit

$$\frac{1}{M} \sum_{i=1}^M u_i(\boldsymbol{\theta})^2 \approx \lim_{M \rightarrow \infty} \frac{1}{M} \sum_{i=1}^M u_i(\boldsymbol{\theta})^2 = \frac{\|\boldsymbol{\theta}\|^2}{2}. \quad (9)$$

The equality holds whenever the encoding weights ( $U_{ij}$  in equation 2) are independent and identically distributed with zero mean and unit variance, as they are here, so that the law of large numbers can be invoked to replace the sum with an expectation over the encoding weight distribution (the factor of 1/2 arises from the fact that only half of each axis counts towards the expectation due to the linear rectification, see Supplementary Materials Section S.2.2 for a formal proof). Inserting these two equations into equation 7 together with the BCI readout equation 3, we obtain

$$\hat{s}, \hat{\tilde{\boldsymbol{\theta}}}_0 = \arg \min_{s, \tilde{\boldsymbol{\theta}}_0} \|s\mathbf{D}\mathbf{r}(t_{\text{end}}; \tilde{\boldsymbol{\theta}}_0) - \mathbf{D}\mathbf{c} - \mathbf{y}^*\|^2 + \frac{\gamma}{2}s^2 \quad (10)$$

subject to  $s > 0$ ,  $\|\tilde{\boldsymbol{\theta}}_0\| = 1$ .

It is then straightforward to solve for  $\hat{s}$  in terms of  $\tilde{\boldsymbol{\theta}}_0$ , yielding the following closed set of equations:

$$\hat{s}(\tilde{\boldsymbol{\theta}}_0) = \phi \left( \frac{(\mathbf{D}\mathbf{c} + \mathbf{y}^*) \cdot \mathbf{D}\mathbf{r}(t_{\text{end}}; \tilde{\boldsymbol{\theta}}_0)}{\|\mathbf{D}\mathbf{r}(t_{\text{end}}; \tilde{\boldsymbol{\theta}}_0)\|^2 + \frac{\gamma}{2}} \right) \quad (11)$$

$$\hat{\tilde{\boldsymbol{\theta}}}_0 = \arg \min_{\tilde{\boldsymbol{\theta}}_0} \|\hat{s}(\tilde{\boldsymbol{\theta}}_0)\mathbf{D}\mathbf{r}(t_{\text{end}}; \tilde{\boldsymbol{\theta}}_0) - \mathbf{D}\mathbf{c} - \mathbf{y}^*\|^2 + \frac{\gamma}{2}\hat{s}(\tilde{\boldsymbol{\theta}}_0)^2 \quad (12)$$

subject to  $\|\tilde{\boldsymbol{\theta}}_0\| = 1$ ,

692 where the  $\cdot$  notation denotes the Euclidean dot product. We have thus reduced what was an optimization  
 693 over all vectors in  $\mathbb{R}^{\tilde{K}}$  (equation 4) to an optimization over all vectors living on the  $\tilde{K}$ -dimensional unit

694 hypersphere (equation 12).

695 We can therefore approximately solve this new optimization problem via brute-force search, by simply  
696 uniformly sampling a large number of  $\tilde{\theta}_0$ 's on the unit hypersphere and identifying the one that produces  
697 the smallest value of the loss function in equation 12. Evaluating  $\mathbf{r}(t_{\text{end}}, \tilde{\theta}_0)$  for a large number of  $\tilde{\theta}_0$ 's  
698 can be done efficiently by using a GPU to integrate in parallel the dynamics driven by each  $\tilde{\theta}_0$ . Note  
699 that, once these activity patterns have been calculated, they can be re-used to perform the brute-force  
700 search optimization for any given value of  $\gamma$ , without having to again integrate the dynamics.

701 For simulations with  $\tilde{K} = 2$ , this brute-force search algorithm sufficed to produce good re-aiming  
702 solutions. In this case, the relevant hypersphere is the unit circle, from which it is straightforward to  
703 sample densely and uniformly. For simulations of generalized re-aiming, however, we took an additional  
704 step to ensure the obtained solutions were as good as they could be even for the larger values of  $\tilde{K}$ ,  
705 where it becomes more difficult to sample densely from the corresponding unit hypersphere. We first  
706 performed a brute-force search over  $2^{17}$  vectors sampled uniformly from the unit hypersphere, as just  
707 described, to obtain an initial estimate of the re-aiming solution. This initial estimate was then used  
708 as a starting point for the L-BFGS algorithm,<sup>86</sup> which we then applied to minimize the re-aiming loss  
709 function (equation 4) with respect to the raw command variables  $\theta_1, \theta_2, \dots, \theta_{\tilde{K}}$ . We found that this  
710 additional step was essential when  $\tilde{K} \geq 10$ .

711 In all simulations in the main text, we used an endpoint time of  $t_{\text{end}} = 1000$  ms, reflecting the typical  
712 time it takes for trained primates to complete center-out reaches under BCI control.<sup>11,14</sup> The results of  
713 simulations with other endpoint times are shown in Supplementary Figure S1b. To simulate a center-out  
714 reaching task, the target readouts  $\mathbf{y}^*$  were set to eight equally spaced unit vectors on the unit circle (cf.  
715 fig. 3c). Mean squared error is calculated as

$$\text{mean squared error} = \frac{1}{8} \sum_{i=1}^8 \|\mathbf{y}(t_{\text{end}}; \hat{\theta}(\mathbf{y}_i^*)) - \mathbf{y}_i^*\|^2, \quad (13)$$

716 where  $\mathbf{y}_1^*, \mathbf{y}_2^*, \dots, \mathbf{y}_8^*$  correspond to the eight radial target readouts. Because the targets are unit norm,  
717 a mean squared error of 1.0 corresponds to that achieved by readouts at the origin.

718 In the case of operant conditioning, there is no “target readout” per se, as subjects are simply  
719 instructed to modulate firing rates as much as possible in a given direction. In this case, a different  
720 re-aiming objective was used, see the section “Simulation of operant conditioning” for details.

### 721 4.3 Setting the metabolic cost weight

722 The metabolic cost weight parameter  $\gamma$  was picked to ensure that low mean squared error would be  
723 achieved under the baseline decoder with  $\tilde{K} = 2$ . We calculated re-aiming solutions with  $\tilde{K} = 2$  for the  
724 baseline decoder under a wide range of values of  $\gamma$ . We took advantage of the fact that the brute-force

725 search algorithm outlined above allows us to easily evaluate solutions for different values of  $\gamma$  with only  
726 a single forward pass of the model. Once we had re-aiming solutions for each value of  $\gamma$ , we calculated  
727 the error achieved by these re-aiming solutions for each target readout, and found the largest value of  
728  $\gamma$  that permitted a squared error of less than .05 for each of the eight targets.  $\gamma$  was then fixed to this  
729 value for simulations with all the decoder perturbations.

#### 730 4.4 Characterizing the reachable manifold

731 The reachable manifold is the set of activity patterns at time  $t_{\text{end}}$  that can be generated by any motor  
732 command allowable under the re-aiming strategy. We assume that these allowable motor commands  
733 are bounded, reflecting the fact that (i) actual extrinsic motor variables are finite and bounded and (ii)  
734 upstream firing rates are bounded. Formally, we enforce this by assuming an upper bound on the motor  
735 command norm,  $\|\boldsymbol{\theta}\| \leq s_{\text{max}}$ . In our simulations of short-term learning of WMP's and OMP's, we set the  
736 value of this bound to the maximum norm over all 2D re-aiming solutions to all decoders. Specifically,  
737 we computed re-aiming solutions for each target readout and decoder perturbation (8 target readouts  
738  $\times$  (100 WMP's + 100 OMP's + baseline decoder) = 1,608 re-aiming solutions) with  $\tilde{K} = 2$ , calculated  
739 their norms, and set  $s_{\text{max}}$  to their maximum. For the randomly connected network presented in the main  
740 text, we found this value to be approximately 1.25.

741 In figure 3f, we drove the motor cortical network with motor command vectors with five distinct  
742 norms,  $\|\boldsymbol{\theta}\| \in \{0.1, 0.4, 0.7, 1.0, s_{\text{max}}\}$ , chosen to aid visualization of the reachable manifold. We picked  
743 256 equally spaced angles between 0 and  $2\pi$  and constructed 2D vectors with each angle and each norm  
744 to obtain the command variable pairs,  $\theta_1, \theta_2$ , shown in fig. 3e (all other command variables were set to  
745 zero). We then simulated the motor cortical network with each of these motor commands to obtain a  
746 large ensemble of activity patterns on the reachable manifold,  $\mathbf{r}(t_{\text{end}}; \boldsymbol{\theta})$ , and projected these onto their  
747 top three principal components to obtain the visualization in figure 3f. Figure 3c plots the readouts of  
748 each of these activity patterns from three different decoders. Figure 4a plots the readouts from four  
749 different WMP decoders, in this case using activity patterns generated from motor commands with four  
750 different norms equally spaced between 0.1 and  $s_{\text{max}}$  (thus producing four loops of readouts instead of  
751 five). In figure 7a, five motor command norms equally spaced between .1 and the maximum norm of the  
752 re-aiming solutions for that pair of neurons were used. These choices were all made to aid visualization  
753 of the reachable manifold's structure.

To obtain the centroid,  $\bar{\mathbf{r}}$ , and covariance,  $\boldsymbol{\Sigma}_r$ , of the reachable manifold for  $\tilde{K} = 2$ , we computed expectations over a uniform distribution on the reachable manifold. Note that an expectation over uniformly distributed activity patterns on the reachable manifold is not the same as an expectation over activity patterns generated by uniformly distributed command variables. These two distributions of activity patterns are related via the Jacobian of the mapping from command variables,  $\theta_1, \theta_2$ , to

activity patterns,  $\mathbf{r}(t_{\text{end}}; \boldsymbol{\theta})$ , which was used to derive the following two expressions for  $\bar{\mathbf{r}}$  and  $\boldsymbol{\Sigma}_r$  (see Supplementary Materials Section S.2.3 for full mathematical derivation):

$$\bar{\mathbf{r}} = \frac{2}{3} s_{\text{max}}^2 \frac{\int_0^{2\pi} \mathbf{r}_0(\varphi) \|\mathbf{r}_0(\varphi)\| \|\mathbf{r}'_0(\varphi)\| \sin \omega(\varphi) d\varphi}{\int_0^{2\pi} \|\mathbf{r}_0(\varphi)\| \|\mathbf{r}'_0(\varphi)\| \sin \omega(\varphi) d\varphi} \quad (14)$$

$$\boldsymbol{\Sigma}_r = \frac{1}{2} s_{\text{max}}^2 \frac{\int_0^{2\pi} \mathbf{r}_0(\varphi) \mathbf{r}_0(\varphi)^T \|\mathbf{r}_0(\varphi)\| \|\mathbf{r}'_0(\varphi)\| \sin \omega(\varphi) d\varphi}{\int_0^{2\pi} \|\mathbf{r}_0(\varphi)\| \|\mathbf{r}'_0(\varphi)\| \sin \omega(\varphi) d\varphi} - \bar{\mathbf{r}} \bar{\mathbf{r}}^T, \quad (15)$$

754 where  $\mathbf{r}_0(\varphi)$  is the population activity at time  $t_{\text{end}}$  generated by a pair of non-zero command variables  
 755  $\theta_1, \theta_2$  with angle  $\varphi$  and unit norm,  $\mathbf{r}'_0(\varphi)$  is its derivative with respect to  $\varphi$ , and  $\omega(\varphi)$  is the angle between  
 756  $\mathbf{r}_0(\varphi)$  and  $\mathbf{r}'_0(\varphi)$ . We used a finite-differences approximation for the derivative  $\mathbf{r}'_0(\varphi)$  and computed these  
 757 integrals numerically by summing over a dense range of values of  $\varphi \in [0, 2\pi]$ . This estimate of the  
 758 reachable manifold centroid,  $\bar{\mathbf{r}}$ , is plotted in figures 4a, 4b, and S2a. This estimate of the reachable  
 759 manifold covariance,  $\boldsymbol{\Sigma}_r$ , is used for the variance explained curve plotted in figure 3g.

Analogous calculations for  $\tilde{K} > 2$  quickly become numerically intractable, as the derivatives and integrals become multivariate as the number of polar coordinates increases. We thus chose to characterize the dimensionality of the reachable manifold under *generalized* re-aiming by the covariance over activity patterns produced by uniformly distributed motor commands, which we denote by  $\boldsymbol{\Sigma}_\theta$ . As already noted, this is not the same as the covariance over activity patterns uniformly distributed on the reachable manifold manifold, but these two covariances are strongly related. This covariance is given by (see Supplementary Materials Section S.2.4 for derivation)

$$\boldsymbol{\Sigma}_\theta = \frac{s_{\text{max}}^2}{3} \left\langle \mathbf{r}(t_{\text{end}}; \tilde{\boldsymbol{\theta}}_0) \mathbf{r}(t_{\text{end}}; \tilde{\boldsymbol{\theta}}_0)^T \right\rangle_{\tilde{\boldsymbol{\theta}}_0} - \frac{s_{\text{max}}^2}{4} \left\langle \mathbf{r}(t_{\text{end}}; \tilde{\boldsymbol{\theta}}_0) \right\rangle_{\tilde{\boldsymbol{\theta}}_0} \left\langle \mathbf{r}(t_{\text{end}}; \tilde{\boldsymbol{\theta}}_0) \right\rangle_{\tilde{\boldsymbol{\theta}}_0}^T, \quad (16)$$

760 where  $\langle \cdot \rangle_{\tilde{\boldsymbol{\theta}}_0}$  denotes an expectation over a uniform distribution on the unit-norm  $(\tilde{K} - 1)$ -sphere. These  
 761 expectations were estimated numerically by uniformly sampling  $2^{17}$  vectors  $\tilde{\boldsymbol{\theta}}_0 \in \mathbb{R}^{\tilde{K}}$  from the unit  
 762 hypersphere, setting the  $\tilde{K}$  non-zero command variables to these values, calculating the activity patterns  
 763 generated by these motor commands at time  $t_{\text{end}} = 1000\text{ms}$ ,  $\mathbf{r}(t_{\text{end}}; \tilde{\boldsymbol{\theta}}_0)$ , and then averaging over the  
 764 resulting ensemble of activity patterns.

765 This estimate of the reachable manifold covariance,  $\boldsymbol{\Sigma}_\theta$ , is used to compute the participation ratio  
 766 plotted in figure 5b as a function of  $\tilde{K}$ , using the formula

$$\text{participation ratio of } \boldsymbol{\Sigma}_\theta = \frac{\text{Tr}[\boldsymbol{\Sigma}_\theta]^2}{\text{Tr}[\boldsymbol{\Sigma}_\theta^2]} = \frac{\left(\sum_{i=1}^N \lambda_i\right)^2}{\sum_{i=1}^N \lambda_i^2}, \quad (17)$$

767 where  $\lambda_1, \lambda_2, \dots, \lambda_N$  are the eigenvalues of  $\boldsymbol{\Sigma}_\theta$ .

## 768 4.5 Quantifying biases in BCI readouts

To quantify behavioral biases, we used the maximal cursor progress metric defined in equation 6. This equation was solved by again exploiting the same re-parameterization of the motor commands we used for calculating re-aiming solutions (equation 7). Specifically, we decompose the vector of non-zero command variables,  $\tilde{\boldsymbol{\theta}} = [\theta_1 \ \theta_2 \ \dots \ \theta_{\tilde{K}}]$ , into a magnitude and direction,  $\tilde{\boldsymbol{\theta}} = s\tilde{\boldsymbol{\theta}}_0$ , where  $s > 0$  and  $\|\tilde{\boldsymbol{\theta}}_0\| = 1$ . Plugging in the readout equation (equation 3) into the definition of cursor progress (equation 5) and exploiting the scale invariance of the motor cortical dynamics (equation 8), we have that the maximal cursor progress is given by

$$\rho^{\max}(\mathbf{y}^*) = \max_{\tilde{\boldsymbol{\theta}}_0} \left\{ \mathbf{D} \left( \hat{s}_\rho(\tilde{\boldsymbol{\theta}}_0) \mathbf{r}(t_{\text{end}}; \tilde{\boldsymbol{\theta}}_0) - \mathbf{c} \right) \cdot \mathbf{y}^* \right\} \quad (18)$$

subject to  $\|\tilde{\boldsymbol{\theta}}_0\| = 1$ ,

where

$$\hat{s}_\rho(\tilde{\boldsymbol{\theta}}_0) := \arg \max_s \left\{ s \mathbf{D} \mathbf{r}(t_{\text{end}}; \tilde{\boldsymbol{\theta}}_0) \cdot \mathbf{y}^* \right\} = \begin{cases} s_{\max} & \text{if } \mathbf{D} \mathbf{r}(t_{\text{end}}; \tilde{\boldsymbol{\theta}}_0) \cdot \mathbf{y}^* > 0 \\ 0 & \text{else} \end{cases} \quad (19)$$

subject to  $0 < s < s_{\max}$

769 Since  $\tilde{K} = 2$  in these simulations (and thus  $\tilde{\boldsymbol{\theta}}_0$  is just a 2D unit vector), we were able to effectively solve  
 770 the optimization problem in equation 18 by brute-force search over densely and uniformly sampled  $\tilde{\boldsymbol{\theta}}_0$ 's  
 771 from the unit circle.

## 772 4.6 Re-analysis of data from Sadtler et al. (2014)

773 To quantify behavioral biases in the experimental data, we estimated the maximal cursor progress in  
 774 each experimental session by using the cursor progress values observed in the window of 50 contiguous  
 775 trials of WMP control with shortest average reach completion times. At each timestep in each trial, we  
 776 calculated the cursor progress in the direction of the target relative to the cursor's position at that time.  
 777 We then binned the per-timestep relative target directions into  $45^\circ$  bins centered at the eight radial reach  
 778 target angles, and averaged the cursor progresses in each bin to obtain an average cursor progress for  
 779 each target direction. We take these averages to be estimates of the subject's *maximal* cursor progress  
 780 with that session's WMP decoder, as they are taken from the 50 trials with fastest reaches.

781 To predict the maximal cursor progress in each session from the target direction angle with  $\mathbf{D}\bar{\mathbf{r}}$ , we  
 782 sought an estimate of the reachable manifold centroid,  $\bar{\mathbf{r}}$ , that could be empirically measured from the  
 783 recorded neural activity, without access to the underlying reachable manifold. To do this, we noticed

784 that, in our model, the time- and trial- averaged population activity generated by the re-aiming solutions  
785 for the baseline decoder – which we denote by  $\hat{\mathbf{r}}$  – was highly correlated with the true reachable manifold  
786 centroid,  $\bar{\mathbf{r}}$ . We therefore used  $\hat{\mathbf{r}}$  to estimate  $\bar{\mathbf{r}}$ , since  $\hat{\mathbf{r}}$  can be easily estimated in the experimental data  
787 by simply averaging motor cortical activity during the baseline decoder control block in each session.  
788 We calculated target-specific means by averaging motor cortical activity over all trials and time during  
789 reaches to each target, and then averaged these target-specific means over targets to obtain  $\hat{\mathbf{r}}$ . This  
790 was the estimate of the reachable manifold centroid – and its projection through the respective WMP  
791 decoder in each session,  $\mathbf{D}\hat{\mathbf{r}}$  – used in the analysis presented in figure 4d.

792 To keep the analysis of the data and the model consistent, we also used an analogous estimate of  
793 the reachable manifold centroid for the analysis of the model in figure 4c. In this case,  $\hat{\mathbf{r}}$  was measured  
794 by simulating reaches to each target by driving the motor cortical network dynamics with the re-aiming  
795 solutions for the baseline decoder, and then averaging the motor cortical firing rates over all time and  
796 over all eight reach directions. We found that the resulting negative correlation was similar regardless of  
797 whether the true reachable manifold centroid,  $\bar{\mathbf{r}}$ , (data not shown) or its estimate,  $\hat{\mathbf{r}}$ , was used.

#### 798 4.7 Simulation of the calibration task

799 The calibration task was simulated by setting the first two command variables  $\theta_1, \theta_2$  to the coordinates  
800 of the reach direction  $\mathbf{y}_i^*$  being presented in each trial (a 2D unit vector pointing in one of eight equally  
801 spaced angles), and setting all other command variables to zero ( $\theta_3 = \theta_4 = \dots = \theta_K = 0$ ). To simulate  
802 noise in the neural responses, we added noise in the dynamics, in the motor commands, and in the  
803 initial conditions on each trial. At each timestep, zero mean Gaussian noise with standard deviation 0.05  
804 was sampled and added to the single neuron potentials  $x_i(t)$  and to the two command variables  $\theta_1, \theta_2$ .  
805 Initial conditions in each trial were sampled randomly from a 0-mean isotropic Gaussian with standard  
806 deviation 0.1. The network was driven for 1000ms in each trial, matching the duration of each trial in  
807 the experiment.

808 For simulations with WMPs and OMPs, we simulated 10 trials of each reach direction, replicating the  
809 structure of the calibration task used by Sadtler et al. (2014). For simulations with credit assignment  
810 rotation perturbations (fig. 6), the calibration task was identical except that only a single trial of each  
811 reach direction was simulated, to mimic the decoder initialization procedure of Zhou et al. (2019). Note  
812 that in all cases re-aiming with  $\tilde{K} = 2$  command variables implies re-aiming with the same two command  
813 variables driving the calibration task neural responses,  $\theta_1$  and  $\theta_2$ .

#### 814 4.8 Within- and outside- manifold perturbations

815 In the BCI system used by Sadtler et al. (2014) and Oby et al. (2019), 96-channel microelectrode arrays  
816 were used to record neural activity. Spikes were detected by threshold crossings in the recorded voltage



817 signals at each electrode, resulting in a series of spike trains at each electrode. Spike trains at each  
 818 electrode could therefore contain spikes from multiple neurons near the electrode site, as no spike sorting  
 819 was performed. In total, about 100 neurons were likely to have been recorded, constituting a small  
 820 fraction of the total population of neurons in motor cortex. To simulate this, we ensured that the BCI  
 821 decoder in our simulations only had access to a linear mixture of firing rates from  $N_r = 99$  neurons (so  
 822 as to be divisible by  $\ell + 1 = 9$ , to group neurons by modulation depth, see below). This was done by first  
 823 multiplying the firing rates with a  $N_r \times N$  “recording matrix”,  $\mathbf{H}$ , which had the following tri-diagonal  
 824 structure

$$H_{ij} = \begin{cases} 0 & \text{if } j > N_r \\ \xi_{ij} \sim \text{Unif}(0, 1) & \text{if } j \leq N_r \text{ and } i - 3 \leq j \leq i + 3 \\ 0 & \text{else} \end{cases} \quad (20)$$

825 Thus, each “neural unit” in the vector  $\mathbf{H}\mathbf{r}$  is composed of a linear mixture of seven neurons, with “neural  
 826 units” with adjacent indices mixing together overlapping sets of neurons.

827 Following Sadtler et al., we next z-scored the activity recorded by each neural unit with respect to  
 828 its statistics during the calibration task,

$$\mathbf{y} = \underbrace{\mathbf{D}_0 \mathbf{S}_r^{-1}}_{\mathbf{D}} \mathbf{H}(\mathbf{r} - \mathbf{c}) \quad (21)$$

829 where  $\mathbf{c}$  is an  $N$ -dimensional vector with the mean firing rate of each neuron and  $\mathbf{S}_r$  is an  $N_r \times N_r$   
 830 diagonal matrix with the standard deviation of each “neural unit”, measured from the simulated activity  
 831 during the calibration task. Readouts,  $\mathbf{y}$ , were obtained by decoding from the  $N_r$ -dimensional vectors  
 832 of z-scored mixed firing rates. It is the  $2 \times N_r$  *effective* decoding matrix,  $\mathbf{D}_0$ , that is perturbed by the  
 833 WMP and OMP decoder perturbations (see below). Note that the full  $2 \times N$  decoding matrix,  $\mathbf{D}$ , is such  
 834 that only its first  $N_r$  columns are non-zero, reflecting the fact that only a subset of the full population  
 835 of motor cortical neurons is recorded by the BCI.

836 For the baseline decoder, the effective decoding matrix  $\mathbf{D}_0$  was constructed following the methods of  
 837 Sadtler et al., with the exception that we used Principal Components Analysis instead of Factor Analysis  
 838 to estimate the intrinsic manifold. This choice was made purely for the sake of numerical convenience, as  
 839 Principal Components Analysis has a closed-form solution that can be computed more efficiently. The  
 840 full procedure for estimating the intrinsic manifold and constructing the baseline decoder is outlined in  
 841 detail in Supplementary Materials Section S.3. In short, the baseline decoder effective decoding matrix  
 842 can be expressed as a product of a  $2 \times \ell$  matrix  $\mathbf{K}$  and an  $\ell \times N_r$  matrix  $\mathbf{L}$ , where  $\ell$  is the dimensionality  
 843 of the intrinsic manifold,

$$\mathbf{D}_0^{\text{base}} = \mathbf{K}\mathbf{L}. \quad (22)$$

844 The matrix  $\mathbf{L}$  projects  $N_r$ -dimensional activity patterns down to the  $\ell$ -dimensional intrinsic manifold;  
845 its rows span the subspace defined by the intrinsic manifold (Supplementary Materials Section S.3.2,  
846 equation 71). In our simulations we used  $\ell = 8$ , as we found that the top 8 principal components contained  
847 95% of the variance in the simulated calibration task responses. The matrix  $\mathbf{K}$  then translates the  
848 resulting  $\ell$ -dimensional dimensionality-reduced activity patterns into 2-dimensional BCI readouts. This  
849 matrix is fit to the calibration task data, by fitting a Kalman filter that accurately decodes the calibration  
850 task stimuli from the dimensionality-reduced calibration task neural responses at each timestep and trial  
851 (Supplementary Materials Section S.3.2, equation 72).

852 Within-manifold perturbations (WMPs) perturb the baseline decoder in such a way that the row  
853 space of  $\mathbf{L}$  remains intact, so as to conserve the decoder's relationship with the intrinsic manifold. This  
854 is done by simply shuffling the rows of  $\mathbf{L}$  without modifying them, via pre-multiplication with a random  
855  $\ell \times \ell$  permutation matrix  $\mathbf{P}$ ,

$$\mathbf{D}_0^{\text{WMP}} = \mathbf{KPL}. \quad (23)$$

856 Outside-manifold decoders, on the other hand, directly disrupt the row space of  $\mathbf{L}$ . This is done by  
857 randomly shuffling the components of each of its rows, via post-multiplication with a random  $N_r \times N_r$   
858 permutation matrix  $\mathbf{P}$ ,

$$\mathbf{D}_0^{\text{OMP}} = \mathbf{KLP}. \quad (24)$$

859 It is important to keep in mind that both WMPs and OMPs can change the readouts in complex ways,  
860 beyond a simple rotation like that depicted by the cartoon in figure 2b (for examples, see fig. 4a here  
861 and supplementary figure 2 in<sup>29</sup>). Once the baseline decoder was constructed, we randomly sampled 100  
862 within-manifold and 100 outside-manifold perturbations by randomly selecting 100  $\ell \times \ell$  and  $N_r \times N_r$   
863 permutation matrices, respectively.

864 To minimize any differences between these two types of decoder perturbations that would go beyond  
865 their opposing relationship to the intrinsic manifold, we imposed several restrictions on the selected  
866 permutation matrices, as was done by Sadtler et al. (see Supplementary Materials Section S.3.3 for  
867 details). First, we enforced that the mean principal angle between the row space of the baseline effective  
868 decoding matrix and the row space of each perturbed effective decoding matrix was between  $60^\circ$  and  
869  $80^\circ$ . Second, we enforced that population activity produced by the re-aiming solutions for the baseline  
870 decoder would produce readouts through each perturbed decoder that resulted in a mean squared error  
871 between 0.6 and 0.8. Finally, we fit tuning curves to the neural activity generated by the re-aiming  
872 solutions for the baseline decoder, and asked how much the preferred directions would need to change  
873 to produce the same readouts under the perturbed decoder, following the same procedure employed by  
874 Sadtler et al. We enforced that this change be between  $30^\circ$  and  $45^\circ$ . We typically found that about  
875 100-200 permutations out of all possible permutation matrices satisfied these criteria. We then randomly

876 sampled 100 of them.

877 Following the procedure used by Sadtler et al. with monkey L, we did not consider all possible  
878  $N_r \times N_r$  permutation matrices for OMPs (as there are 99! of them). Rather, we grouped all  $N_r$  neural  
879 units into  $\ell$  groups, and then considered all  $\ell$ -dimensional permutations of these groups (of which there  
880 are 8!). In other words, rather than permuting all  $N_r$  columns of  $\mathbf{L}$ ,  $\ell$  groups of columns were permuted.  
881 This ensured that the total number of possible decoder perturbations was the same for WMPs and  
882 OMPs. The  $\ell$  groups were assigned as follows: for each neural unit in  $\mathbf{H}\mathbf{r}$ , we fit a cosine tuning curve  
883 to its calibration task responses to obtain its modulation depth (equation 26), assigned the  $N_r/(\ell + 1)$   
884 neurons with smallest modulation depths to a small-modulation group not to be permuted, and randomly  
885 assigned the remaining neurons to  $\ell$  high-modulation groups to be permuted; following Sadtler et al., the  
886 small-modulation group was never permuted to avoid cases in which an inactive or noisy neuron could  
887 get assigned a large decoding weight.

888 In figure 3g, we define the “dimensions” of the intrinsic manifold as a set of orthonormal basis vectors  
889  $\mathbf{f}_1, \mathbf{f}_2, \dots, \mathbf{f}_\ell$  spanning the intrinsic manifold (Supplementary Materials Section S.3.1). We then calculated  
890 the variance explained by each dimension by

$$\text{variance explained by dimension } i = \frac{\mathbf{f}_i^T \boldsymbol{\Sigma} \mathbf{f}_i}{\text{Tr}[\boldsymbol{\Sigma}]}. \quad (25)$$

891 For the gray curve,  $\boldsymbol{\Sigma}$  was set to the sample covariance of the simulated calibration task responses. For  
892 the purple curve,  $\boldsymbol{\Sigma}$  was set to the reachable manifold covariance  $\boldsymbol{\Sigma}_r$  (defined in equation 15). In each  
893 case, the cumulative variance explained was calculated by ordering the dimensions by variance explained  
894 and then summing them in that order.

## 895 4.9 Credit assignment rotation perturbations

896 In the BCI system used by Zhou et al. (2019), recorded activity was sorted by matching spike waveforms  
897 to identify spikes from single neurons, resulting in the identification of 10–12 individual neurons. Import-  
898 tantly, each neuron had reliable tuning to reach direction during the calibration task. In our simulation,  
899 we modelled this by randomly choosing 80 neurons, fitting tuning curves to their activity during the  
900 calibration task, and selecting only those with modulation depth greater than 0.5 (see below for how  
901 modulation depth is measured). This typically resulted in 10–15 neurons being included in the BCI  
902 decoder (i.e. being assigned non-zero weights in the decoding matrix  $\mathbf{D}$ ); no “recording matrix”  $\mathbf{H}$  was  
903 used in these simulations. For the particular network model used in the simulations reported in the main  
904 text, this selection procedure resulted in  $N_r = 11$  neurons being included.

905 Tuning curves were fit to time-averaged simulated firing rates in the calibration task,  $\bar{\mathbf{r}}_1, \dots, \bar{\mathbf{r}}_8$ , in  
906 response to presentation of each of the eight radial reach targets,  $\mathbf{y}_1^*, \dots, \mathbf{y}_8^*$  (cf. section “Simulation of

907 the calibration task”). An  $N \times 3$  matrix of tuning weights,  $\mathbf{T}$ , was fit to predict these average responses  
 908 from the respective reach target coordinates,

$$\hat{\mathbf{T}} = \arg \min_{\mathbf{T}} \sum_{j=1}^8 \|\bar{\mathbf{r}}_j - \mathbf{T}\tilde{\mathbf{y}}_j\|^2 = \left( \sum_{j=1}^8 \bar{\mathbf{r}}_j \tilde{\mathbf{y}}_j^T \right) \left( \sum_{j=1}^8 \tilde{\mathbf{y}}_j \tilde{\mathbf{y}}_j^T \right)^{-1}, \quad (26)$$

909 where  $\tilde{\mathbf{y}}_j$  is a 3D vector with the coordinates of the direction of the  $j$ th reach target,  $\mathbf{y}_j^*$ , as its first two  
 910 components and a constant 1 in its third component, included to model baseline tonic firing rates of each  
 911 neuron. Thus, only the first two columns of the tuning weight matrix  $\mathbf{T}$  model how the  $i$ th neuron’s  
 912 firing rate depends on the reach target’s direction, whereas its third column models activity independent  
 913 of the reach target. To extract from these weights the directional tuning of neuron  $i$ , we take the 2D  
 914 vector comprising the first two components of the  $i$ th row of  $\hat{\mathbf{T}}$ . We denote this 2D vector by  $m_i \mathbf{p}_i$ , where  
 915  $\mathbf{p}_i$  is a unit vector pointing in its direction and  $m_i$  is its norm. The angle of  $\mathbf{p}_i$  is neuron  $i$ ’s preferred  
 916 direction, and  $m_i$  is its modulation depth.

917 Following the methods of Zhou et al. (2019), the baseline decoder was constructed as follows. First,  
 918 raw firing rates were baseline-subtracted and normalized by their modulation depths,

$$\mathbf{r}^{\text{norm}} = \mathbf{M}(\mathbf{r} - \mathbf{c}), \quad (27)$$

919 where  $\mathbf{c}$  is given by the third column of  $\hat{\mathbf{T}}$ , containing the baseline firing rates estimated from the linear  
 920 regression fit (equation 26), and  $\mathbf{M}$  is an  $N_r \times N$  diagonal rectangular matrix containing the inverse  
 921 modulation depths  $m_i^{-1}$  for each of the  $N_r$  neurons recorded by the BCI on the diagonal across the first  
 922  $N_r$  columns 0 everywhere else. These normalized firing rates were then transformed into 2D readouts by  
 923 a  $2 \times N_r$  effective decoding matrix  $\mathbf{D}_0^{\text{base}}$  containing the preferred direction vectors  $\mathbf{p}_i$  of each of the  $N_r$   
 924 recorded neurons in their corresponding columns. More precisely, the  $i$ th column of  $\mathbf{D}_0^{\text{base}}$ ,  $\mathbf{d}_i$ , is given  
 925 by

$$\mathbf{d}_i = \begin{cases} \frac{k}{N_r} \mathbf{p}_i & \text{if neuron } i \text{ is recorded by BCI} \\ \mathbf{0} & \text{else,} \end{cases} \quad (28)$$

926 where the scaling constant  $k$  is chosen to minimize the mean squared error between the readouts from  
 927 the calibration task activity and the target readouts. This is the classic population vector algorithm  
 928 (PVA).<sup>87</sup> The full  $2 \times N$  decoding matrix of the baseline decoder was thus  $\mathbf{D} = \mathbf{D}_0^{\text{base}} \mathbf{M}$ , which has  
 929 non-zero weights only in the  $N_r$  columns corresponding to the  $N_r$  recorded neurons.

930 Credit assignment rotation perturbations were constructed by simply picking a random subset of the  
 931 columns of  $\mathbf{D}_0^{\text{base}}$  and rotating them. In our simulations, we picked a random 50% of these columns  
 932 and rotated them  $75^\circ$  counter-clockwise, as was done in the decoder perturbations used by Zhou et al.  
 933 (2019). We sampled 100 random perturbations in this way, in each case rotating a different subset of

934 columns. The normalization matrix  $\mathbf{M}$  and baseline subtraction parameters  $\mathbf{c}$  are kept the same for all  
 935 decoders.

936 To measure the tuning changes predicted by re-aiming, we simulated cursor reaches with each decoder  
 937 by driving the motor cortical network with the re-aiming solutions for that decoder. In each case, noise  
 938 was applied to the dynamics, exactly as in the calibration task. We then fit tuning curves to each neuron's  
 939 time-averaged activity, using linear regression exactly as described in equation 26, and extracted the  
 940 preferred direction of each rotated, non-rotated, and indirect neuron. For each perturbed decoder, we  
 941 then determined each neuron's change in preferred direction by calculating the difference between its  
 942 preferred direction under the re-aiming solutions for the perturbed decoder and its preferred direction  
 943 under the re-aiming solutions for the baseline decoder (cf. figures 6b, 6c). These changes were then  
 944 averaged over all neurons in each sub-population (rotated, non-rotated, or indirect). Figure 6e shows the  
 945 percentiles (median and quartiles), over all 100 sampled decoder perturbations, of this average tuning  
 946 change. An analogous analysis of the changes in modulation depth is shown in Supplementary Figure  
 947 S5a.

#### 948 4.10 Simulation of operant conditioning

949 In an operant conditioning task, there is no “target readout” per se. The objective is to simply increase  
 950 the activity of one neuron over another, as much as possible. We can thus express the objective as  
 951 maximizing the difference in firing rate between the two neurons, which can be thought of as a one-  
 952 dimensional linear readout from the population. Formally, we calculate readouts in this task by a dot  
 953 product between the firing rate vector  $\mathbf{r}$  and a decoding vector  $\mathbf{d}$  which has a +1 for the target neuron,  
 954 a -1 for the distractor neuron, and 0's everywhere else. This one-dimensional readout indicates how  
 955 much more active the target neuron is than the distractor neuron. The goal in an operant conditioning  
 956 task is to maximize this readout.

957 Adding in a metabolic cost, the objective function we use for re-aiming is

$$\hat{\boldsymbol{\theta}} = \arg \max_{\theta_1, \theta_2, \dots, \theta_{\bar{K}}} \left\{ \mathbf{d} \cdot \mathbf{r}(t_{\text{end}}; \boldsymbol{\theta}) - \frac{\gamma}{M} \sum_{i=1}^M u_i(\boldsymbol{\theta})^2 \right\}. \quad (29)$$

Letting  $\tilde{\boldsymbol{\theta}} = \begin{bmatrix} \theta_1 & \theta_2 & \dots & \theta_{\bar{K}} \end{bmatrix}$  denote the non-zero command variables, we again re-parameterize this optimization problem into an optimization over the magnitude,  $s$ , and direction,  $\tilde{\boldsymbol{\theta}}_0$ , of  $\tilde{\boldsymbol{\theta}}$ ,

$$\hat{s}, \tilde{\boldsymbol{\theta}}_0 = \arg \max_{s, \tilde{\boldsymbol{\theta}}_0} \left\{ \mathbf{d} \cdot \mathbf{r}(t_{\text{end}}; s\tilde{\boldsymbol{\theta}}_0) - \frac{\gamma}{M} \sum_{i=1}^M u_i(s\tilde{\boldsymbol{\theta}}_0)^2 \right\} \quad \text{subject to } s > 0, \|\tilde{\boldsymbol{\theta}}_0\| = 1 \quad (30)$$

$$\approx \arg \max_{s, \tilde{\boldsymbol{\theta}}_0} \left\{ s\mathbf{d} \cdot \mathbf{r}(t_{\text{end}}; \tilde{\boldsymbol{\theta}}_0) - \frac{\gamma}{2}s^2 \right\} \quad \text{subject to } s > 0, \|\tilde{\boldsymbol{\theta}}_0\| = 1, \quad (31)$$

where the approximation follows from the application of the scale invariance of the network dynamics (equation 8) and the mean-field approximation of the metabolic cost (equation 9). This approximation allows us to analytically solve for the optimal magnitude  $\hat{s}$ ,

$$\hat{s}(\tilde{\theta}_0) = \arg \max_s \left\{ s \mathbf{d} \cdot \mathbf{r}(t_{\text{end}}; \tilde{\theta}_0) - \frac{\gamma}{2} s^2 \right\} = \frac{1}{\gamma} \phi \left( \mathbf{d} \cdot \mathbf{r}(t_{\text{end}}; \tilde{\theta}_0) \right), \quad (32)$$

subject to  $s > 0$

which in turn allows us to solve for the optimal direction,  $\hat{\theta}_0$ , via optimization over the  $\tilde{K}$ -dimensional unit hypersphere,

$$\hat{\theta}_0 = \arg \max_{\tilde{\theta}_0} \left\{ \hat{s}(\tilde{\theta}_0) \mathbf{d} \cdot \mathbf{r}(t_{\text{end}}; \tilde{\theta}_0) - \frac{\gamma}{2} \hat{s}(\tilde{\theta}_0)^2 \right\} \quad \text{subject to } \|\tilde{\theta}_0\| = 1 \quad (33)$$

$$= \arg \max_{\tilde{\theta}_0} \left\{ \phi \left( \mathbf{d} \cdot \mathbf{r}(t_{\text{end}}; \tilde{\theta}_0) \right) \right\} \quad \text{subject to } \|\tilde{\theta}_0\| = 1, \quad (34)$$

958 where the second equality follows from plugging in equation 32 and simplifying. In all our operant  
 959 conditioning simulations, we used  $\tilde{K} = 2$ , which enabled us to easily solve this optimization problem via  
 960 brute force search over the unit circle. As in other simulations, we used  $t_{\text{end}} = 1000\text{ms}$ .

961 Note that the optimal readout achieved by the re-aiming solution is

$$\mathbf{d} \cdot \mathbf{r}(t_{\text{end}}; \hat{\theta}_0) = \mathbf{d} \cdot \mathbf{r}(t_{\text{end}}; \hat{s}(\hat{\theta}_0) \hat{\theta}_0) = \hat{s}(\hat{\theta}_0) \left( \mathbf{d} \cdot \mathbf{r}(t_{\text{end}}; \hat{\theta}_0) \right) = \frac{1}{\gamma} \phi \left( \mathbf{d} \cdot \mathbf{r}(t_{\text{end}}; \hat{\theta}_0) \right)^2. \quad (35)$$

962 Thus, changing the exact value of  $\gamma$  only re-scales the re-aiming solutions and the readouts they produce.  
 963 We thus simply set it to  $\gamma = 1$  in all our simulations of this task.

964 In classic operant conditioning experiments,<sup>28</sup> neurons selected for operant conditioning had to be  
 965 active prior to the conditioning task to be identified by the recording electrode. We imposed a similar  
 966 constraint in our simulation by first driving the network with 50 random  $K = 100$ -dimensional motor  
 967 commands for  $t_{\text{end}} = 1000\text{ms}$ , and identifying the 50% of neurons with highest average firing rate over  
 968 motor commands and time. The neuron pairs used for operant conditioning were sampled from this  
 969 sub-population.

970 To simulate neural activity during a baseline period of spontaneous behavior prior to operant con-  
 971 ditioning, we used a similar procedure but now driving the network with 50 random  $\tilde{K}$ -dimensional  
 972 motor commands, with  $\tilde{K} = 2$ . This allowed us to ask whether operant conditioning performance under  
 973 re-aiming could be predicted from correlations arising during spontaneous behavior driven by the same  
 974 command variables used subsequently for re-aiming. In figure 7c, correlations were measured by cor-  
 975 relation coefficient between the two conditioned neurons. In figure 7d, correlation coefficients between  
 976 each indirect neuron and the target neuron are plotted against the firing rate of the indirect neuron at

977  $t_{\text{end}} = 1000\text{ms}$  when driving the network with the re-aiming solution.

978 **4.11 Table of simulation parameters**

Parameter name/description	Notation	Value
<b><i>Recurrent neural network dynamics</i></b>		
number of neurons in motor cortical network	$N$	256
number of neurons in upstream population	$M$	256
recurrent weights	$W_{ij}^{\text{rec}}$	$\overset{\text{i.i.d.}}{\sim} \mathcal{N}(0, 1/N)$
input weights	$W_{ij}^{\text{in}}$	$\overset{\text{i.i.d.}}{\sim} \mathcal{N}(0, 1/M)$
encoding weights	$U_{ij}$	$\overset{\text{i.i.d.}}{\sim} \mathcal{N}(0, 1)$
network dynamics time constant	$\tau$	200ms
<b><i>WMP and OMP decoders</i></b>		
calibration task network dynamics noise	-	$\overset{\text{i.i.d.}}{\sim} \mathcal{N}(0, 0.05^2)$
calibration task command variable noise	-	$\overset{\text{i.i.d.}}{\sim} \mathcal{N}(0, 0.05^2)$
calibration task initial condition noise	-	$\overset{\text{i.i.d.}}{\sim} \mathcal{N}(0, 0.1^2)$
calibration task trial duration	-	1000ms
number of recorded neurons used to fit the decoders	$N_r$	99
979 dimensionality of intrinsic manifold	$\ell$	8
bounds on principal angle between perturbed decoders and baseline decoder	-	$[60^\circ, 80^\circ]$
bounds on mean squared error of perturbed decoder readouts	-	$[0.6, 0.8]$
bounds on preferred direction change imposed by perturbed decoders	-	$[30^\circ, 45^\circ]$
<b><i>Re-aiming optimization</i></b>		
endpoint time	$t_{\text{end}}$	1000ms
maximum baseline decoder squared error, which sets $\gamma$ (Methods Section 4.3)	-	.05
<b><i>Credit assignment rotation perturbations</i></b>		
minimum modulation depth for neuron to be recorded	-	0.5
number of recorded neurons	$N_r$	11
fraction of decoding vectors rotated	-	50%
decoding vector rotation angle	-	$75^\circ$ CCW
<b><i>Operant conditioning</i></b>		
command variables driving bouts spontaneous activity	$\theta_1, \theta_2$	$\overset{\text{i.i.d.}}{\sim} \mathcal{N}(0, 1/2)$
duration of bouts of spontaneous activity	-	1000ms

## References

- 980
- 981 [1] R. Shadmehr and F. A. Mussa-Ivaldi. “Adaptive Representation of Dynamics during Learning of a  
982 Motor Task”. en. In: **Journal of Neuroscience** 14.5 (May 1994), pp. 3208–3224. ISSN: 0270-6474,  
983 1529-2401. DOI: [10.1523/JNEUROSCI.14-05-03208.1994](https://doi.org/10.1523/JNEUROSCI.14-05-03208.1994).
- 984 [2] Chiang-Shan Ray Li, Camillo Padoa-Schioppa, and Emilio Bizzi. “Neuronal Correlates of Motor  
985 Performance and Motor Learning in the Primary Motor Cortex of Monkeys Adapting to an External  
986 Force Field”. en. In: **Neuron** 30.2 (May 2001), pp. 593–607. ISSN: 0896-6273. DOI: [10.1016/S0896-  
987 6273\(01\)00301-4](https://doi.org/10.1016/S0896-6273(01)00301-4).
- 988 [3] Rony Paz et al. “Acquisition and Generalization of Visuomotor Transformations by Nonhuman  
989 Primates”. en. In: **Experimental Brain Research** 161.2 (Feb. 2005), pp. 209–219. ISSN: 1432-  
990 1106. DOI: [10.1007/s00221-004-2061-4](https://doi.org/10.1007/s00221-004-2061-4).
- 991 [4] Gonçalo Lopes et al. “A Robust Role for Motor Cortex”. en. In: **bioRxiv** (May 2017), p. 058917.  
992 DOI: [10.1101/058917](https://doi.org/10.1101/058917).
- 993 [5] Risa Kawai et al. “Motor Cortex Is Required for Learning but Not for Executing a Motor Skill”. en.  
994 In: **Neuron** 86.3 (May 2015), pp. 800–812. ISSN: 0896-6273. DOI: [10.1016/j.neuron.2015.03.024](https://doi.org/10.1016/j.neuron.2015.03.024).
- 995 [6] Mackenzie Weygandt Mathis, Alexander Mathis, and Naoshige Uchida. “Somatosensory Cortex  
996 Plays an Essential Role in Forelimb Motor Adaptation in Mice”. en. In: **Neuron** 93.6 (Mar. 2017),  
997 1493–1503.e6. ISSN: 0896-6273. DOI: [10.1016/j.neuron.2017.02.049](https://doi.org/10.1016/j.neuron.2017.02.049).
- 998 [7] Matthew G. Perich, Juan A. Gallego, and Lee E. Miller. “A Neural Population Mechanism for  
999 Rapid Learning”. en. In: **Neuron** 100.4 (Nov. 2018), 964–976.e7. ISSN: 0896-6273. DOI: [10.1016/  
1000 j.neuron.2018.09.030](https://doi.org/10.1016/j.neuron.2018.09.030).
- 1001 [8] Matthew D Golub et al. “Brain–Computer Interfaces for Dissecting Cognitive Processes Underly-  
1002 ing Sensorimotor Control”. In: **Current Opinion in Neurobiology**. Neurobiology of Cognitive  
1003 Behavior 37 (Apr. 2016), pp. 53–58. ISSN: 0959-4388. DOI: [10.1016/j.conb.2015.12.005](https://doi.org/10.1016/j.conb.2015.12.005). (Visited  
1004 on 04/27/2020).
- 1005 [9] Richard A. Andersen, Tyson Aflalo, and Spencer Kellis. “From Thought to Action: The Brain–Machine  
1006 Interface in Posterior Parietal Cortex”. In: **Proceedings of the National Academy of Sciences**  
1007 116.52 (Dec. 2019), pp. 26274–26279. ISSN: 0027-8424, 1091-6490. DOI: [10.1073/pnas.1902276116](https://doi.org/10.1073/pnas.1902276116).  
1008 (Visited on 02/26/2020).
- 1009 [10] Emily R. Oby et al. “Intracortical Brain–Machine Interfaces”. In: **Neural Engineering**. Ed. by  
1010 Bin He. Cham: Springer International Publishing, 2020, pp. 185–221. ISBN: 978-3-030-43395-6. DOI:  
1011 [10.1007/978-3-030-43395-6\\_5](https://doi.org/10.1007/978-3-030-43395-6_5). (Visited on 07/30/2021).



- 1012 [11] Beata Jarosiewicz et al. “Functional Network Reorganization during Learning in a Brain-Computer  
1013 Interface Paradigm”. In: **Proceedings of the National Academy of Sciences** 105.49 (Dec.  
1014 2008), pp. 19486–19491. ISSN: 0027-8424, 1091-6490. DOI: [10.1073/pnas.0808113105](https://doi.org/10.1073/pnas.0808113105). (Visited on  
1015 02/04/2020).
- 1016 [12] Steven M. Chase, Robert E. Kass, and Andrew B. Schwartz. “Behavioral and Neural Correlates of  
1017 Visuomotor Adaptation Observed through a Brain-Computer Interface in Primary Motor Cortex”.  
1018 In: **Journal of Neurophysiology** 108.2 (Apr. 2012), pp. 624–644. ISSN: 0022-3077. DOI: [10.1152/  
1019 jn.00371.2011](https://doi.org/10.1152/jn.00371.2011). (Visited on 02/16/2020).
- 1020 [13] Vikash Gilja et al. “A High-Performance Neural Prosthesis Enabled by Control Algorithm Design”.  
1021 In: **Nature Neuroscience** 15.12 (Dec. 2012), pp. 1752–1757. ISSN: 1546-1726. DOI: [10.1038/nn.  
1022 3265](https://doi.org/10.1038/nn.3265). (Visited on 04/27/2020).
- 1023 [14] Patrick T. Sadtler et al. “Neural Constraints on Learning”. In: **Nature** 512.7515 (Aug. 2014),  
1024 pp. 423–426. ISSN: 1476-4687. DOI: [10.1038/nature13665](https://doi.org/10.1038/nature13665). (Visited on 02/13/2020).
- 1025 [15] Karunesh Ganguly and Jose M. Carmena. “Emergence of a Stable Cortical Map for Neuroprosthetic  
1026 Control”. In: **PLOS Biology** 7.7 (July 2009), e1000153. ISSN: 1545-7885. DOI: [10.1371/journal.  
1027 pbio.1000153](https://doi.org/10.1371/journal.pbio.1000153). (Visited on 04/27/2020).
- 1028 [16] Emily R. Oby et al. “New Neural Activity Patterns Emerge with Long-Term Learning”. In: **Pro-  
1029 ceedings of the National Academy of Sciences** 116.30 (2019), pp. 15210–15215.
- 1030 [17] Robert Legenstein et al. “A Reward-Modulated Hebbian Learning Rule Can Explain Experimen-  
1031 tally Observed Network Reorganization in a Brain Control Task”. In: **Journal of Neuroscience**  
1032 30.25 (June 2010), pp. 8400–8410. ISSN: 0270-6474, 1529-2401. DOI: [10.1523/JNEUROSCI.4284-  
1033 09.2010](https://doi.org/10.1523/JNEUROSCI.4284-09.2010). (Visited on 03/13/2020).
- 1034 [18] Ben Engelhard et al. “Neuronal Activity and Learning in Local Cortical Networks Are Modulated  
1035 by the Action-Perception State”. In: **bioRxiv** (Feb. 2019), p. 537613. DOI: [10.1101/537613](https://doi.org/10.1101/537613).  
1036 (Visited on 07/29/2020).
- 1037 [19] Emil Wärnberg and Arvind Kumar. “Perturbing Low Dimensional Activity Manifolds in Spiking  
1038 Neuronal Networks”. In: **PLOS Computational Biology** 15.5 (May 2019), e1007074. ISSN: 1553-  
1039 7358. DOI: [10.1371/journal.pcbi.1007074](https://doi.org/10.1371/journal.pcbi.1007074). (Visited on 04/27/2020).
- 1040 [20] Barbara Feulner and Claudia Clopath. “Neural Manifold under Plasticity in a Goal Driven Learning  
1041 Behaviour”. In: **PLOS Computational Biology** 17.2 (Feb. 2021), e1008621. ISSN: 1553-7358. DOI:  
1042 [10.1371/journal.pcbi.1008621](https://doi.org/10.1371/journal.pcbi.1008621). (Visited on 03/06/2021).

- 1043 [21] Rodolphe Héliot et al. “Learning in Closed-Loop Brain–Machine Interfaces: Modeling and Exper-  
1044 imental Validation”. In: **IEEE Transactions on Systems, Man, and Cybernetics, Part B**  
1045 **(Cybernetics)** 40.5 (Oct. 2010), pp. 1387–1397. ISSN: 1941-0492. DOI: [10.1109/TSMCB.2009.](https://doi.org/10.1109/TSMCB.2009.2036931)  
1046 [2036931](https://doi.org/10.1109/TSMCB.2009.2036931).
- 1047 [22] Justin Werfel, Xiaohui Xie, and H. Sebastian Seung. “Learning Curves for Stochastic Gradient  
1048 Descent in Linear Feedforward Networks”. In: **Advances in Neural Information Processing**  
1049 **Systems**. 2004, pp. 1197–1204.
- 1050 [23] Naoki Hiratani et al. “On the Stability and Scalability of Node Perturbation Learning”. In: **Ad-**  
1051 **vances in Neural Information Processing Systems** 35 (Dec. 2022), pp. 31929–31941. (Visited  
1052 on 05/24/2023).
- 1053 [24] A. Aldo Faisal, Luc P. J. Selen, and Daniel M. Wolpert. “Noise in the Nervous System”. In: **Nat**  
1054 **Rev Neurosci** 9.4 (Apr. 2008), pp. 292–303. ISSN: 1471-0048. DOI: [10.1038/nrn2258](https://doi.org/10.1038/nrn2258). (Visited on  
1055 10/15/2023).
- 1056 [25] Francis Crick. “The Recent Excitement about Neural Networks”. In: **Nature** 337.6203 (Jan. 1989),  
1057 pp. 129–132. ISSN: 1476-4687. DOI: [10.1038/337129a0](https://doi.org/10.1038/337129a0). (Visited on 07/22/2020).
- 1058 [26] Sergey Bartunov et al. “Assessing the Scalability of Biologically-Motivated Deep Learning Algo-  
1059 rithms and Architectures”. In: **Advances in Neural Information Processing Systems** 31.  
1060 Ed. by S. Bengio et al. Curran Associates, Inc., 2018, pp. 9368–9378. (Visited on 07/22/2020).
- 1061 [27] Timothy P. Lillicrap et al. “Backpropagation and the Brain”. In: **Nature Reviews Neuroscience**  
1062 21.6 (June 2020), pp. 335–346. ISSN: 1471-0048. DOI: [10.1038/s41583-020-0277-3](https://doi.org/10.1038/s41583-020-0277-3). (Visited on  
1063 07/22/2020).
- 1064 [28] E E Fetz and M A Baker. “Operantly Conditioned Patterns on Precentral Unit Activity and Corre-  
1065 lated Responses in Adjacent Cells and Contralateral Muscles.” In: **Journal of Neurophysiology**  
1066 36.2 (Mar. 1973), pp. 179–204. ISSN: 0022-3077. DOI: [10.1152/jn.1973.36.2.179](https://doi.org/10.1152/jn.1973.36.2.179). (Visited on  
1067 07/14/2020).
- 1068 [29] Matthew D. Golub et al. “Learning by Neural Reassociation”. In: **Nature Neuroscience** 21.4  
1069 (Apr. 2018), pp. 607–616. ISSN: 1546-1726. DOI: [10.1038/s41593-018-0095-3](https://doi.org/10.1038/s41593-018-0095-3). (Visited on  
1070 11/11/2019).
- 1071 [30] Jay A Hennig et al. “Constraints on Neural Redundancy”. In: **eLife** 7 (Aug. 2018). Ed. by Eric  
1072 Shea-Brown and Timothy E Behrens, e36774. ISSN: 2050-084X. DOI: [10.7554/eLife.36774](https://doi.org/10.7554/eLife.36774).  
1073 (Visited on 02/16/2020).
- 1074 [31] Karunesh Ganguly et al. “Reversible Large-Scale Modification of Cortical Networks during Neu-  
1075 roprosthetic Control”. In: **Nature Neuroscience** 14.5 (May 2011), pp. 662–667. ISSN: 1546-1726.  
1076 DOI: [10.1038/mn.2797](https://doi.org/10.1038/mn.2797). (Visited on 04/13/2020).

- 1077 [32] Saurabh Vyas et al. “Neural Population Dynamics Underlying Motor Learning Transfer”. In: **Neuron** 97.5 (Mar. 2018), 1177–1186.e3. ISSN: 0896-6273. DOI: [10.1016/j.neuron.2018.01.040](https://doi.org/10.1016/j.neuron.2018.01.040).  
1078  
1079 (Visited on 02/16/2020).
- 1080 [33] Steven M. Chase, Andrew B. Schwartz, and Robert E. Kass. “Latent Inputs Improve Estimates  
1081 of Neural Encoding in Motor Cortex”. In: **Journal of Neuroscience** 30.41 (Oct. 2010), pp. 13873–  
1082 13882. ISSN: 0270-6474, 1529-2401. DOI: [10.1523/JNEUROSCI.2325-10.2010](https://doi.org/10.1523/JNEUROSCI.2325-10.2010). (Visited on 07/14/2020).
- 1083 [34] Eun Jung Hwang, Paul M. Bailey, and Richard A. Andersen. “Volitional Control of Neural Activity  
1084 Relies on the Natural Motor Repertoire”. In: **Current Biology** 23.5 (Mar. 2013), pp. 353–361.  
1085 ISSN: 0960-9822. DOI: [10.1016/j.cub.2013.01.027](https://doi.org/10.1016/j.cub.2013.01.027). (Visited on 02/04/2020).
- 1086 [35] Sofia Sakellaridi et al. “Intrinsic Variable Learning for Brain-Machine Interface Control by Human  
1087 Anterior Intraparietal Cortex”. In: **Neuron** 102.3 (May 2019), 694–705.e3. ISSN: 0896-6273. DOI:  
1088 [10.1016/j.neuron.2019.02.012](https://doi.org/10.1016/j.neuron.2019.02.012). (Visited on 02/16/2020).
- 1089 [36] A. d’Avella and E. Bizzi. “Low Dimensionality of Supraspinally Induced Force Fields”. en. In:  
1090 **Proceedings of the National Academy of Sciences** 95.13 (June 1998), pp. 7711–7714. ISSN:  
1091 0027-8424, 1091-6490. DOI: [10.1073/pnas.95.13.7711](https://doi.org/10.1073/pnas.95.13.7711).
- 1092 [37] Andrea d’Avella, Philippe Saltiel, and Emilio Bizzi. “Combinations of Muscle Synergies in the  
1093 Construction of a Natural Motor Behavior”. en. In: **Nature Neuroscience** 6.3 (Mar. 2003),  
1094 pp. 300–308. ISSN: 1546-1726. DOI: [10.1038/nn1010](https://doi.org/10.1038/nn1010).
- 1095 [38] Yuri P. Ivanenko et al. “Temporal Components of the Motor Patterns Expressed by the Hu-  
1096 man Spinal Cord Reflect Foot Kinematics”. In: **Journal of Neurophysiology** 90.5 (Nov. 2003),  
1097 pp. 3555–3565. ISSN: 0022-3077. DOI: [10.1152/jn.00223.2003](https://doi.org/10.1152/jn.00223.2003).
- 1098 [39] Emanuel Todorov. “Optimality Principles in Sensorimotor Control”. en. In: **Nature Neuro-**  
1099 **science** 7.9 (Sept. 2004), pp. 907–915. ISSN: 1546-1726. DOI: [10.1038/nn1309](https://doi.org/10.1038/nn1309).
- 1100 [40] Jason J. Kutch and Francisco J. Valero-Cuevas. “Challenges and New Approaches to Proving the  
1101 Existence of Muscle Synergies of Neural Origin”. en. In: **PLOS Computational Biology** 8.5  
1102 (May 2012), e1002434. ISSN: 1553-7358. DOI: [10.1371/journal.pcbi.1002434](https://doi.org/10.1371/journal.pcbi.1002434).
- 1103 [41] Naveen Kuppaswamy and Christopher M. Harris. “Do Muscle Synergies Reduce the Dimensionality  
1104 of Behavior?” English. In: **Frontiers in Computational Neuroscience** 8 (2014). ISSN: 1662-  
1105 5188. DOI: [10.3389/fncom.2014.00063](https://doi.org/10.3389/fncom.2014.00063).
- 1106 [42] Mark M. Churchland et al. “Neural Population Dynamics during Reaching”. en. In: **Nature**  
1107 487.7405 (July 2012), pp. 51–56. ISSN: 1476-4687. DOI: [10.1038/nature11129](https://doi.org/10.1038/nature11129).

- 1108 [43] Guillaume Hennequin, Tim P. Vogels, and Wulfram Gerstner. “Optimal Control of Transient Dy-  
1109 namics in Balanced Networks Supports Generation of Complex Movements”. en. In: **Neuron** 82.6  
1110 (June 2014), pp. 1394–1406. ISSN: 0896-6273. DOI: [10.1016/j.neuron.2014.04.045](https://doi.org/10.1016/j.neuron.2014.04.045).
- 1111 [44] David Sussillo et al. “A Neural Network That Finds a Naturalistic Solution for the Production of  
1112 Muscle Activity”. In: **Nature Neuroscience** 18.7 (July 2015), pp. 1025–1033. ISSN: 1546-1726.  
1113 DOI: [10.1038/nn.4042](https://doi.org/10.1038/nn.4042). (Visited on 04/22/2020).
- 1114 [45] Abigail A. Russo et al. “Motor Cortex Embeds Muscle-like Commands in an Untangled Population  
1115 Response”. en. In: **Neuron** 97.4 (Feb. 2018), 953–966.e8. ISSN: 0896-6273. DOI: [10.1016/j.neuron.  
1116 2018.01.004](https://doi.org/10.1016/j.neuron.2018.01.004).
- 1117 [46] Ta-Chu Kao, Mahdieh S. Sadabadi, and Guillaume Hennequin. “Optimal Anticipatory Control as  
1118 a Theory of Motor Preparation: A Thalamo-Cortical Circuit Model”. en. In: **Neuron** 109.9 (May  
1119 2021), 1567–1581.e12. ISSN: 0896-6273. DOI: [10.1016/j.neuron.2021.03.009](https://doi.org/10.1016/j.neuron.2021.03.009).
- 1120 [47] Mijail D. Serruya et al. “Instant Neural Control of a Movement Signal”. In: **Nature** 416.6877  
1121 (Mar. 2002), pp. 141–142. ISSN: 1476-4687. DOI: [10.1038/416141a](https://doi.org/10.1038/416141a). (Visited on 08/16/2020).
- 1122 [48] Leigh R. Hochberg et al. “Neuronal Ensemble Control of Prosthetic Devices by a Human with  
1123 Tetraplegia”. In: **Nature** 442.7099 (July 2006), pp. 164–171. ISSN: 1476-4687. DOI: [10.1038/  
1124 nature04970](https://doi.org/10.1038/nature04970). (Visited on 08/16/2020).
- 1125 [49] Meel Velliste et al. “Cortical Control of a Prosthetic Arm for Self-Feeding”. In: **Nature** 453.7198  
1126 (June 2008), pp. 1098–1101. ISSN: 1476-4687. DOI: [10.1038/nature06996](https://doi.org/10.1038/nature06996). (Visited on 08/16/2020).
- 1127 [50] Matthew D Golub, Byron M Yu, and Steven M Chase. “Internal Models for Interpreting Neu-  
1128 ral Population Activity during Sensorimotor Control”. In: **eLife** 4 (Dec. 2015). Ed. by Timothy  
1129 Behrens, e10015. ISSN: 2050-084X. DOI: [10.7554/eLife.10015](https://doi.org/10.7554/eLife.10015). (Visited on 01/21/2020).
- 1130 [51] Sergey D. Stavisky et al. “Motor Cortical Visuomotor Feedback Activity Is Initially Isolated  
1131 from Downstream Targets in Output-Null Neural State Space Dimensions”. In: **Neuron** 95.1  
1132 (July 2017), 195–208.e9. ISSN: 0896-6273. DOI: [10.1016/j.neuron.2017.05.023](https://doi.org/10.1016/j.neuron.2017.05.023). (Visited on  
1133 04/28/2020).
- 1134 [52] Maryam M. Shanechi et al. “Rapid Control and Feedback Rates Enhance Neuroprosthetic Con-  
1135 trol”. In: **Nature Communications** 8.1 (Jan. 2017), p. 13825. ISSN: 2041-1723. DOI: [10.1038/  
1136 ncomms13825](https://doi.org/10.1038/ncomms13825). (Visited on 10/27/2020).
- 1137 [53] W. T. Thach. “Correlation of Neural Discharge with Pattern and Force of Muscular Activity, Joint  
1138 Position, and Direction of Intended next Movement in Motor Cortex and Cerebellum”. In: **Journal  
1139 of Neurophysiology** 41.3 (May 1978), pp. 654–676. ISSN: 0022-3077. DOI: [10.1152/jn.1978.41.  
1140 3.654](https://doi.org/10.1152/jn.1978.41.3.654).

- 1141 [54] Eberhard E. Fetz. “Are Movement Parameters Recognizably Coded in the Activity of Single Neu-  
1142 rons?” en. In: **Behavioral and Brain Sciences** 15.4 (Dec. 1992), pp. 679–690. ISSN: 1469-1825,  
1143 0140-525X. DOI: [10.1017/S0140525X00072599](https://doi.org/10.1017/S0140525X00072599).
- 1144 [55] Eberhard E. Fetz. “Volitional Control of Neural Activity: Implications for Brain–Computer In-  
1145 terfaces”. In: **The Journal of Physiology** 579.3 (2007), pp. 571–579. ISSN: 1469-7793. DOI:  
1146 [10.1113/jphysiol.2006.127142](https://doi.org/10.1113/jphysiol.2006.127142). (Visited on 07/14/2020).
- 1147 [56] Stephen H. Scott. “Inconvenient Truths about Neural Processing in Primary Motor Cortex”. en.  
1148 In: **The Journal of Physiology** 586.5 (2008), pp. 1217–1224. ISSN: 1469-7793. DOI: [10.1113/  
1149 jphysiol.2007.146068](https://doi.org/10.1113/jphysiol.2007.146068).
- 1150 [57] Mohsen Omrani et al. “Perspectives on Classical Controversies about the Motor Cortex”. In: **Jour-  
1151 nal of Neurophysiology** 118.3 (June 2017), pp. 1828–1848. ISSN: 0022-3077. DOI: [10.1152/jn.  
1152 00795.2016](https://doi.org/10.1152/jn.00795.2016).
- 1153 [58] Juan A. Gallego et al. “Neural Manifolds for the Control of Movement”. en. In: **Neuron** 94.5 (June  
1154 2017), pp. 978–984. ISSN: 0896-6273. DOI: [10.1016/j.neuron.2017.05.025](https://doi.org/10.1016/j.neuron.2017.05.025).
- 1155 [59] Francis R. Willett et al. “Hand Knob Area of Premotor Cortex Represents the Whole Body in a  
1156 Compositional Way”. en. In: **Cell** 181.2 (Apr. 2020), 396–409.e26. ISSN: 0092-8674. DOI: [10.1016/  
1157 j.cell.2020.02.043](https://doi.org/10.1016/j.cell.2020.02.043).
- 1158 [60] Peiran Gao et al. “A Theory of Multineuronal Dimensionality, Dynamics and Measurement”. en.  
1159 In: **bioRxiv** (Nov. 2017), p. 214262. DOI: [10.1101/214262](https://doi.org/10.1101/214262).
- 1160 [61] Xiao Zhou et al. “Distinct Types of Neural Reorganization during Long-Term Learning”. In: **Jour-  
1161 nal of Neurophysiology** 121.4 (Feb. 2019), pp. 1329–1341. ISSN: 0022-3077. DOI: [10.1152/jn.  
1162 00466.2018](https://doi.org/10.1152/jn.00466.2018). (Visited on 03/13/2020).
- 1163 [62] Marvin Minsky. “Steps toward Artificial Intelligence”. In: **Proceedings of the IRE** 49.1 (Jan.  
1164 1961), pp. 8–30. ISSN: 2162-6634. DOI: [10.1109/JRPROC.1961.287775](https://doi.org/10.1109/JRPROC.1961.287775).
- 1165 [63] Eberhard E. Fetz. “Operant Conditioning of Cortical Unit Activity”. In: **Science** 163.3870 (Feb.  
1166 1969), pp. 955–958. ISSN: 0036-8075, 1095-9203. DOI: [10.1126/science.163.3870.955](https://doi.org/10.1126/science.163.3870.955). (Visited  
1167 on 08/07/2020).
- 1168 [64] Aaron C. Koralek et al. “Corticostriatal Plasticity Is Necessary for Learning Intentional Neuro-  
1169 prosthetic Skills”. In: **Nature** 483.7389 (Mar. 2012), pp. 331–335. ISSN: 1476-4687. DOI: [10.1038/  
1170 nature10845](https://doi.org/10.1038/nature10845). (Visited on 07/22/2020).
- 1171 [65] Kelly B. Clancy et al. “Volitional Modulation of Optically Recorded Calcium Signals during Neuro-  
1172 prosthetic Learning”. In: **Nature Neuroscience** 17.6 (June 2014), pp. 807–809. ISSN: 1546-1726.  
1173 DOI: [10.1038/nn.3712](https://doi.org/10.1038/nn.3712). (Visited on 11/25/2019).

- 1174 [66] Vivek R. Athalye et al. “Evidence for a Neural Law of Effect”. In: **Science** 359.6379 (2018),  
1175 pp. 1024–1029.
- 1176 [67] Robert Legenstein, Dejan Pecevski, and Wolfgang Maass. “A Learning Theory for Reward-Modulated  
1177 Spike-Timing-Dependent Plasticity with Application to Biofeedback”. In: **PLOS Computational**  
1178 **Biology** 4.10 (Oct. 2008), e1000180. ISSN: 1553-7358. DOI: [10.1371/journal.pcbi.1000180](https://doi.org/10.1371/journal.pcbi.1000180). (Vis-  
1179 ited on 08/07/2020).
- 1180 [68] Peter C. Humphreys et al. **BCI Learning Phenomena Can Be Explained by Gradient-**  
1181 **Based Optimization**. Dec. 2022. DOI: [10.1101/2022.12.08.519453](https://doi.org/10.1101/2022.12.08.519453). (Visited on 05/02/2023).
- 1182 [69] Jordan A. Taylor, John W. Krakauer, and Richard B. Ivry. “Explicit and Implicit Contributions to  
1183 Learning in a Sensorimotor Adaptation Task”. In: **J. Neurosci.** 34.8 (Feb. 2014), pp. 3023–3032.  
1184 ISSN: 0270-6474, 1529-2401. DOI: [10.1523/JNEUROSCI.3619-13.2014](https://doi.org/10.1523/JNEUROSCI.3619-13.2014). (Visited on 07/21/2020).
- 1185 [70] Aaron L. Wong et al. “Explicit Knowledge Enhances Motor Vigor and Performance: Motivation  
1186 versus Practice in Sequence Tasks”. In: **Journal of Neurophysiology** 114.1 (July 2015), pp. 219–  
1187 232. ISSN: 0022-3077. DOI: [10.1152/jn.00218.2015](https://doi.org/10.1152/jn.00218.2015). (Visited on 01/26/2024).
- 1188 [71] Alexandre Payeur, Amy L. Orsborn, and Guillaume Lajoie. **Neural Manifolds and Gradient-**  
1189 **Based Adaptation in Neural-Interface Tasks**. Mar. 2023. DOI: [10.1101/2023.03.11.532146](https://doi.org/10.1101/2023.03.11.532146).  
1190 (Visited on 05/02/2023).
- 1191 [72] Jeffrey A. Kleim et al. “Cortical Synaptogenesis and Motor Map Reorganization Occur during Late,  
1192 But Not Early, Phase of Motor Skill Learning”. In: **J. Neurosci.** 24.3 (Jan. 2004), pp. 628–633.  
1193 ISSN: 0270-6474, 1529-2401. DOI: [10.1523/JNEUROSCI.3440-03.2004](https://doi.org/10.1523/JNEUROSCI.3440-03.2004). (Visited on 03/13/2020).
- 1194 [73] Xulu Sun et al. “Cortical Preparatory Activity Indexes Learned Motor Memories”. en. In: **Nature**  
1195 602.7896 (Feb. 2022), pp. 274–279. ISSN: 1476-4687. DOI: [10.1038/s41586-021-04329-x](https://doi.org/10.1038/s41586-021-04329-x).
- 1196 [74] Darby M. Losey et al. “Learning leaves a memory trace in motor cortex”. In: **Current Biology**  
1197 (2024). DOI: [10.1016/j.cub.2024.03.003](https://doi.org/10.1016/j.cub.2024.03.003).
- 1198 [75] James B. Heald, Máté Lengyel, and Daniel M. Wolpert. “Contextual Inference Underlies the Learn-  
1199 ing of Sensorimotor Repertoires”. In: **Nature** 600.7889 (Dec. 2021), pp. 489–493. ISSN: 1476-4687.  
1200 DOI: [10.1038/s41586-021-04129-3](https://doi.org/10.1038/s41586-021-04129-3). (Visited on 05/23/2023).
- 1201 [76] Ta-Chu Kao and Guillaume Hennequin. “Neuroscience out of Control: Control-Theoretic Perspec-  
1202 tives on Neural Circuit Dynamics”. en. In: **Current Opinion in Neurobiology**. Computational  
1203 Neuroscience 58 (Oct. 2019), pp. 122–129. ISSN: 0959-4388. DOI: [10.1016/j.conb.2019.09.001](https://doi.org/10.1016/j.conb.2019.09.001).
- 1204 [77] Peiran Gao and Surya Ganguli. “On Simplicity and Complexity in the Brave New World of Large-  
1205 Scale Neuroscience”. en. In: **Current Opinion in Neurobiology**. Large-Scale Recording Tech-  
1206 nology (32) 32 (June 2015), pp. 148–155. ISSN: 0959-4388. DOI: [10.1016/j.conb.2015.04.003](https://doi.org/10.1016/j.conb.2015.04.003).

- 1207 [78] Krishna V. Shenoy and Jose M. Carmena. “Combining Decoder Design and Neural Adaptation  
1208 in Brain-Machine Interfaces”. In: **Neuron** 84.4 (Nov. 2014), pp. 665–680. ISSN: 0896-6273. DOI:  
1209 [10.1016/j.neuron.2014.08.038](https://doi.org/10.1016/j.neuron.2014.08.038). (Visited on 10/07/2020).
- 1210 [79] Serafeim Perdikis and Jose del R. Millan. “Brain-Machine Interfaces: A Tale of Two Learners”. In:  
1211 **IEEE Systems, Man, and Cybernetics Magazine** 6.3 (July 2020), pp. 12–19. ISSN: 2333-942X.  
1212 DOI: [10.1109/MSMC.2019.2958200](https://doi.org/10.1109/MSMC.2019.2958200).
- 1213 [80] Jane X. Wang et al. “Prefrontal Cortex as a Meta-Reinforcement Learning System”. In: **Nature**  
1214 **Neuroscience** 21.6 (June 2018), pp. 860–868. ISSN: 1546-1726. DOI: [10.1038/s41593-018-0147-](https://doi.org/10.1038/s41593-018-0147-8)  
1215 [8](https://doi.org/10.1038/s41593-018-0147-8). (Visited on 07/14/2020).
- 1216 [81] Ryan M. Neely et al. “Volitional Modulation of Primary Visual Cortex Activity Requires the Basal  
1217 Ganglia”. In: **Neuron** 97.6 (Mar. 2018), 1356–1368.e4. ISSN: 0896-6273. DOI: [10.1016/j.neuron.](https://doi.org/10.1016/j.neuron.2018.01.051)  
1218 [2018.01.051](https://doi.org/10.1016/j.neuron.2018.01.051). (Visited on 11/25/2019).
- 1219 [82] N. Vendrell-Llopis et al. “Ventral Striatum Uses a Temporal Difference Rule for Prediction during  
1220 Neuroprosthetic Control”. In: **2019 9th International IEEE/EMBS Conference on Neural**  
1221 **Engineering (NER)**. Mar. 2019, pp. 562–565. DOI: [10.1109/NER.2019.8716982](https://doi.org/10.1109/NER.2019.8716982).
- 1222 [83] Vivek R Athalye, Jose M Carmena, and Rui M Costa. “Neural Reinforcement: Re-Entering and  
1223 Refining Neural Dynamics Leading to Desirable Outcomes”. In: **Current Opinion in Neurobi-**  
1224 **ology**. Neurobiology of Behavior 60 (Feb. 2020), pp. 145–154. ISSN: 0959-4388. DOI: [10.1016/j.](https://doi.org/10.1016/j.conb.2019.11.023)  
1225 [conb.2019.11.023](https://doi.org/10.1016/j.conb.2019.11.023). (Visited on 02/26/2020).
- 1226 [84] Barbara Feulner et al. “Small, Correlated Changes in Synaptic Connectivity May Facilitate Rapid  
1227 Motor Learning”. In: **Nat Commun** 13.1 (Sept. 2022), p. 5163. ISSN: 2041-1723. DOI: [10.1038/](https://doi.org/10.1038/s41467-022-32646-w)  
1228 [s41467-022-32646-w](https://doi.org/10.1038/s41467-022-32646-w). (Visited on 05/02/2023).
- 1229 [85] Ricky T. Q. Chen et al. “Neural Ordinary Differential Equations”. In: **Advances in Neural**  
1230 **Information Processing Systems 31**. Curran Associates, Inc., 2018, pp. 6571–6583. (Visited  
1231 on 08/02/2020).
- 1232 [86] Richard H. Byrd et al. “A Limited Memory Algorithm for Bound Constrained Optimization”. In:  
1233 **SIAM Journal on Scientific Computing** 16.5 (Sept. 1995), pp. 1190–1208. ISSN: 1064-8275.  
1234 DOI: [10.1137/0916069](https://doi.org/10.1137/0916069).
- 1235 [87] A. P. Georgopoulos, A. B. Schwartz, and R. E. Kettner. “Neuronal Population Coding of Movement  
1236 Direction”. en. In: **Science** 233.4771 (Sept. 1986), pp. 1416–1419. ISSN: 0036-8075, 1095-9203. DOI:  
1237 [10.1126/science.3749885](https://doi.org/10.1126/science.3749885).

1238

## Acknowledgments

1239 This work was supported by the Gatsby Charitable Foundation (J.A.M., P.E.L.), Wellcome Trust  
1240 110114/Z/15/Z (P.E.L.), University College London Research Excellence Scholarship (J.A.M.), NIH  
1241 K99/R00 MH121533 (M.D.G.), NIH R01 NS129584 (A.P.B., S.M.C., B.M.Y.), NSF NCS DRL 2124066  
1242 and 2123911 (B.M.Y., S.M.C., A.P.B.), Simons Foundation 543065 and NC-GB-CULM-00003241-05  
1243 (B.M.Y.).



## Supplementary Matrials

1244		
1245		
1246		
1247	S.1	Extended modeling results . . . . . 49
1248		
1249	S.1.1	Structured motor cortical connectivity . . . . . 49
1250	S.1.2	Analysis of WMP bias . . . . . 52
1251	S.1.3	Non-negative firing rates are necessary to replicate biases in WMP learning . . . . . 54
1252	S.1.4	Operant conditioning of ensembles of neurons . . . . . 56
1253	S.1.5	Changes in modulation depth of motor cortical tuning curves . . . . . 56
1254	S.1.6	Closed-loop feedback control . . . . . 57
1255	S.2	Mathematical derivations . . . . . 59
1256	S.2.1	Scale-invariance of RNN dynamics with rectified linear activation function . . . . . 59
1257	S.2.2	Large $M$ limit of quadratic metabolic cost . . . . . 60
1258	S.2.3	Reachable manifold moments for $\tilde{K} = 2$ . . . . . 61
1259	S.2.4	Reachable manifold moments for $\tilde{K} > 2$ . . . . . 64
1260	S.3	Extended methods . . . . . 65
1261	S.3.1	Estimating the intrinsic manifold . . . . . 65
1262	S.3.2	Construction of the baseline decoder . . . . . 66
1263	S.3.3	Subsampling WMPs and OMPs . . . . . 68
1264	References	. . . . . 70

### S.1 Extended modeling results

#### S.1.1 Structured motor cortical connectivity

In addition to the randomly connected network architecture used in the results presented in the main text, we simulated re-aiming in the task of Sadtler et al. (2014) with alternative motor cortical connectivity profiles, described below. In each case, we simulated the calibration task, sampled decoder perturbations, and computed re-aiming solutions as described in the main text, except for a few minor modifications noted below. Results of these simulations are shown in figure S1.

**Random excitatory/inhibitory (E/I) connectivity:** a random sparse and balanced E/I recurrent connectivity matrix was constructed following the sampling procedure described in.<sup>1</sup> In short, all excitatory weights had the same strength, all inhibitory had the same strength (re-scaled relative to the excitatory weights to account for the different number of excitatory and inhibitory neurons), and each row of the weight matrix was enforced to be 0 mean to enforce so-called E/I balance. We used a sparsity of 10% (i.e. only 10% of weights were non-zero), with 80% of the neurons in the population being

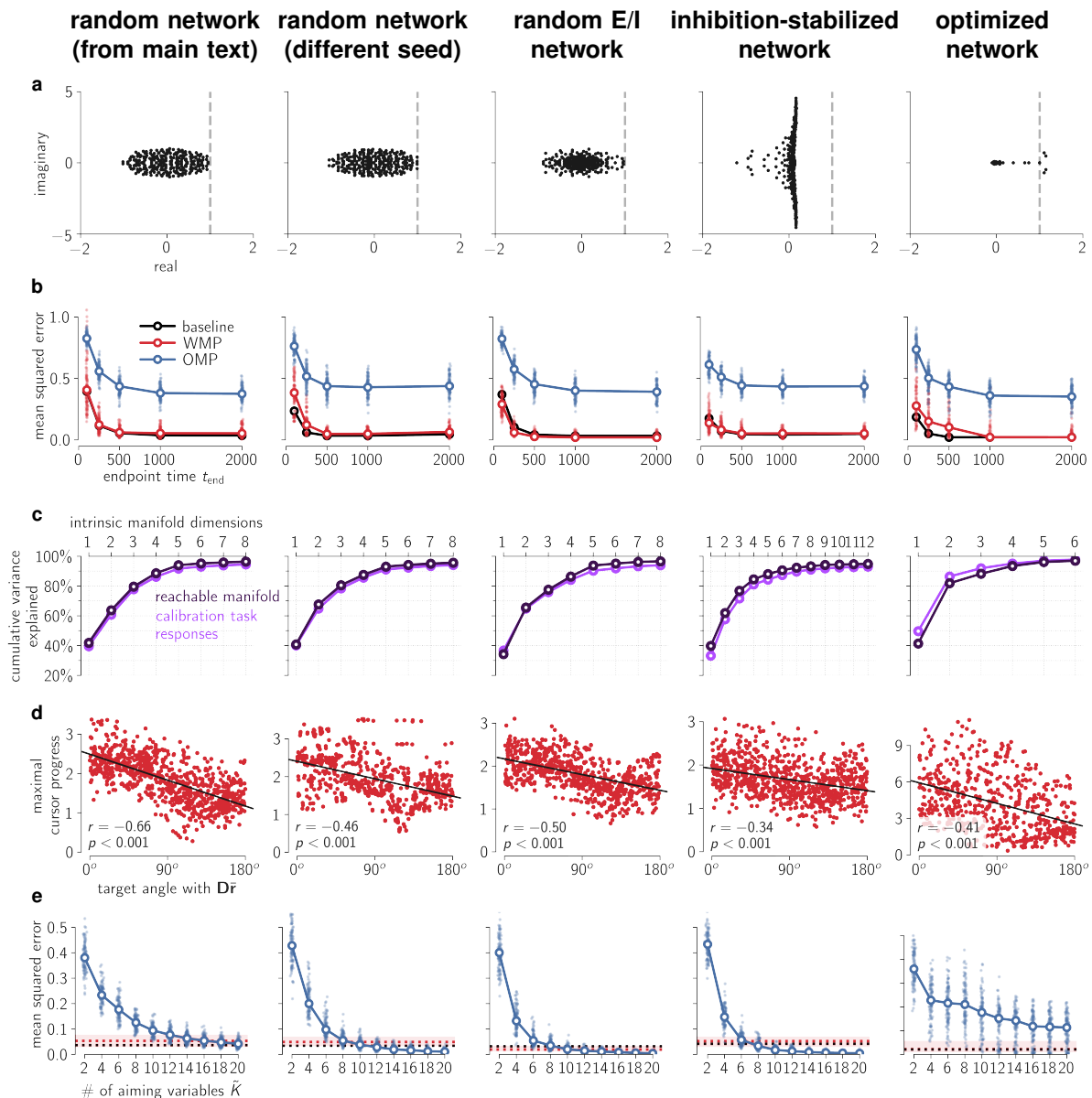


**Figure S1:** Each column shows simulation results for a different network: (1) the randomly connected network used in the main text; (2) another randomly connected network, with weights sampled in exactly the same way; (3) a network with random E/I connectivity; (4) a network with inhibition-optimized E/I connectivity; (5) network with connectivity optimized for delayed center-out reaching.

**a.** Eigenspectra of recurrent weight matrices of each network, plotted on the complex plane. Note that the optimized network has low-rank connectivity: almost all eigenvalues are clustered at 0. Dashed vertical line marks the linear stability boundary of a real value of 1.0.

**b.** Mean squared error achieved by re-aiming solutions for different endpoint times,  $t_{\text{end}}$ , for each decoder. Lighter markers correspond to individual decoders, darker open markers (connected by lines) show medians over all decoders. Note that the metabolic cost weight,  $\gamma$ , is fixed to the same value, which was picked to guarantee low error under the baseline decoder for  $t_{\text{end}} = 1000\text{ms}$  only (see Methods Section 4.3). Thus, the error rises as the endpoint time decreases below this, as higher magnitude motor commands are necessary to achieve low error faster. However, note that the difference between baseline decoder, WMPs, and OMPs remains the same even at these lower values of  $t_{\text{end}}$ .

**c.** Calibration task response and reachable manifold variance cumulatively accounted for by each dimension of the intrinsic manifold, as in fig. 3g. Intrinsic manifold was found to be about 12-dimensional with inhibition-optimized connectivity and about 6-dimensional with connectivity optimized for delayed center-out reaching.

**d.** Maximal cursor progress for each target and WMP as a function of target direction angle with  $\mathbf{D}\bar{\mathbf{r}}$ , as in fig. 4c.

**e.** Mean squared error achieved for each OMP by re-aiming with different numbers of command variables,  $\bar{K}$ , as in fig. 5a.

1278 excitatory. Input and encoding weights were sampled randomly as for the randomly connected network  
 1279 in the main text.

1280 **Inhibition-optimized excitatory/inhibitory connectivity:** a sparse and balanced E/I recurrent  
1281 connectivity matrix was constructed following the optimization procedure described in.<sup>2</sup> In short, the  
1282 excitatory weights were initialized to be very strong, and then inhibitory weights were optimized to  
1283 ensure the dynamics were stable (by minimizing the spectral abscissa of the full connectivity matrix).  
1284 Half of the neurons were assigned to be excitatory, and the inhibitory weights were enforced to be on  
1285 average three times stronger than the excitatory weights. The only difference with<sup>2</sup> was that the weight  
1286 matrices were initialized with a spectral radius of 5, rather than 10. This was necessary as we found  
1287 that an initial spectral radius of 10 lead to chaotic dynamics under constant input. Input and encoding  
1288 weights were sampled randomly as for the randomly connected network in the main text.

1289 Because of their highly non-normal dynamics, these networks were highly sensitive to changes in  
1290 initial conditions, even with the reduced initial spectral radius. We therefore reduced the standard  
1291 deviation of the initial conditions by half when simulating the calibration task (see Methods Section  
1292 4.7). These networks produced much higher-dimensional calibration task responses than the randomly  
1293 connected network, so a 12-dimensional intrinsic manifold was used for constructing WMP's and OMP's  
1294 (i.e.  $\ell = 12$ ).

1295 **Connectivity optimized for delayed center-out reaching:** network weights were optimized to  
1296 produce joint torques for performing delayed center-out reaches with a biomechanical arm model. The  
1297 architecture and optimization scheme followed that used by,<sup>3</sup> in which the recurrent network is driven by  
1298 two distinct inputs. The first input is a one-dimensional signal reflecting a go cue that indicates when the  
1299 reach should be performed (go time). This was built into our model by setting  $\theta_K$  to 1 at the start of the  
1300 trial and then setting it to 0 at go time, 1000ms after trial start. The other input is a two-dimensional  
1301 signal reflecting the visual presentation of the target to reach towards, presented prior to go time to  
1302 prepare the subject (or network) to perform the delayed center-out reach. This was built into our model  
1303 by setting  $\theta_1, \theta_2$  to the coordinates of the reach target at a randomly sampled target presentation time  
1304 before the go cue, and then setting it back to 0 at the same time the go cue input is shut off. All other  
1305 command variables are set to 0 ( $\theta_3 = \theta_4 = \dots = \theta_{K-1} = 0$ ). We chose to encode the go cude with  
1306 the very last command variable,  $\theta_K$ , to reflect the hypothesis that subjects would not re-aim with this  
1307 non-directional command variable, neither in  $\tilde{K} = 2$ -dimensional re-aiming nor in generalized re-aiming  
1308 with up to  $\tilde{K} = 20$  command variables.

1309 Two joint torques were read out from the network through a set of readout weights, which were  
1310 optimized along with the input, recurrent, and encoding weights. The weights were optimized to produce  
1311 the joint torques required to move the endpoint of a planar two-link arm model<sup>4</sup> to the cued reach target,  
1312 in 500ms with a bell-shaped speed profile. Following the methods of,<sup>5</sup> these target joint torques were  
1313 computed by backpropagating through the arm model dynamics to minimize mean squared error between

1314 the arm endpoint velocity and the desired velocity profile for each reach target. We then trained the  
1315 network weights so that in each trial it would produce 0 torque until go time, followed by the optimal  
1316 reaching torque corresponding to the reach target on that trial.

1317 The loss function used to optimize the network weights was a combination of the mean squared error  
1318 plus L2 regularization on all weights and on network firing rates, to encourage naturalistic solutions to  
1319 this task.<sup>3</sup> This was minimized via stochastic gradient descent using the Adam optimization algorithm  
1320 with learning rate set to .001.<sup>6</sup> Since only three command variables were non-zero during this task, only  
1321 the three corresponding columns of the encoding weights  $U_{ij}$  were optimized by this procedure. The  
1322 remaining columns were thus fixed to their random initialization, as for the randomly connected network  
1323 in the main text.

1324 As is often observed in networks trained to perform a single task,<sup>7</sup> the resulting optimized recurrent  
1325 connectivity matrix had low rank (Supplementary Figure S1a). Its activity was consequently constrained  
1326 to a much lower-dimensional subspace than that of the other networks.<sup>8</sup> This network thus produced  
1327 much lower-dimensional calibration task responses than the randomly connected networks did. We  
1328 therefore used a 6-dimensional intrinsic manifold for constructing WMP's and OMP's in simulations  
1329 with this network (i.e.  $\ell = 6$ ). This meant that only  $6! - 1 = 719$  possible decoder perturbations  
1330 existed (as opposed to 40,319), so far fewer decoder perturbations satisfied the stringent criteria outlined  
1331 in Methods Section 4.8 for sampling WMP's and OMP's. We thus loosened these criteria to include  
1332 WMP's and OMP's with mean squared error going up to 1.2. These networks were also found to be  
1333 highly sensitive to noise, so we reduced the standard deviation of the noise in the dynamics and in the  
1334 initial conditions during simulation of the calibration task to 0.02 and 0.005, respectively.

1335 Because of the low-rank recurrent connectivity, we found that re-aiming with even  $\tilde{K} = 20$  command  
1336 variables could not yield good solutions for OMP control with this network (Supplementary Figure S1e).  
1337 In other words, the low-rank connectivity did not permit the generation of activity patterns outside of  
1338 the intrinsic manifold, even when re-aiming with a large number of command variables. It is important  
1339 to keep in mind, however, that in reality motor cortical connectivity is likely optimized to perform  
1340 a wide variety of motor behaviors, rather than a single center-out reaching task. This assumption is  
1341 implicit in our choice of high-rank connectivity structure, as in several other recent models of motor  
1342 cortical function.<sup>2,5,9</sup> Note also that such high-rank connectivity was necessary for our model to produce  
1343 calibration task responses with dimensionality near the dimensionality of 10 observed by Sadtler et al.  
1344 (2014) (Supplementary Figure S1c).

### 1345 S.1.2 Analysis of WMP bias

1346 This section provides a more detailed analysis of why WMP reachable readouts are biased in the direction  
1347 of  $D\bar{\mathbf{r}}$  (fig. 4c). Specifically, we show that the reachabout readouts are centered away from the origin,

1348 and the direction of this displacement is dictated by the relationship between the reachable manifold  
1349 and the calibration task activity that the decoders are fit to, leading to the observed bias.

1350 We begin by calculating the centroid of the reachable readouts,  $\bar{\mathbf{y}}$ , which is given by the readout of  
1351 the reachable manifold centroid,  $\bar{\mathbf{r}}$ ,

$$\bar{\mathbf{y}} = \mathbf{D}(\bar{\mathbf{r}} - \mathbf{c}), \quad (36)$$

1352 where  $\mathbf{c}$  is the decoder centering vector (equation 3), set to the mean population response during the  
1353 calibration task (Methods Section 4.8). As long as the reachable readouts are somewhat symmetrically  
1354 distributed around their centroid, then they will be biased in the direction of their centroid. This equation  
1355 shows that the direction and magnitude of this bias thus depends on the difference between between the  
1356 mean calibration task response,  $\mathbf{c}$ , and the reachable manifold centroid,  $\bar{\mathbf{r}}$ .

1357 Because the calibration task responses are driven by a subset of the motor commands used to define  
1358 the reachable manifold (fig. 3e), these two directions are highly aligned. This is shown empirically for our  
1359 simulations in Supplementary Figure S2a, where we overlay the network's firing rates during individual  
1360 trials of the calibration task on top of the reachable manifold, along with the mean population response  
1361 and the reachable manifold centroid. Population activity during the calibration task evidently evolves  
1362 along the same directions in state space occupied by the reachable manifold, and thus its mean,  $\mathbf{c}$ , is  
1363 highly aligned with the manifold's centroid,  $\bar{\mathbf{r}}$ .

1364 Next, note that the reachable manifold centroid has a larger norm than the calibration task mean.  
1365 That is because the reachable manifold contains activity patterns generated by motor commands with  
1366 larger norms than those driving the calibration task responses (fig. 3e), so its centroid comprises higher  
1367 firing rates. The underlying reason for this is that, in our simulations, we selected the metabolic cost  
1368 weight,  $\gamma$ , such that it guaranteed high re-aiming performance with the baseline decoder (see Methods  
1369 Section 4.3). Because the baseline decoder fit is not perfect (due both to the noise and to the non-linear  
1370 mapping from calibration task stimuli to neural activity), stronger firing rates than those evoked by the  
1371 calibration task are required to achieve such high performance, so the resulting metabolic cost weight  
1372 permits stronger motor commands than the ones driving the calibration task.

1373 Putting these two observations together, we have that

$$\mathbf{c} \approx a\bar{\mathbf{r}} \Rightarrow \bar{\mathbf{y}} \approx (1 - a)\mathbf{D}\bar{\mathbf{r}}, \quad 0 < a < 1. \quad (37)$$

1374 In other words, the reachable readout centroid points in the direction of  $\mathbf{D}\bar{\mathbf{r}}$ . This explains why WMP  
1375 readouts are biased in that direction.

1376 An important remaining question, however, is why *baseline* decoder readouts are not biased in that  
1377 direction. The baseline decoder shares the same centering vector,  $\mathbf{c}$ , so, by the above logic, should inherit  
1378 the same bias. The reason it does not is that the reachable manifold centroid is orthogonal to the baseline

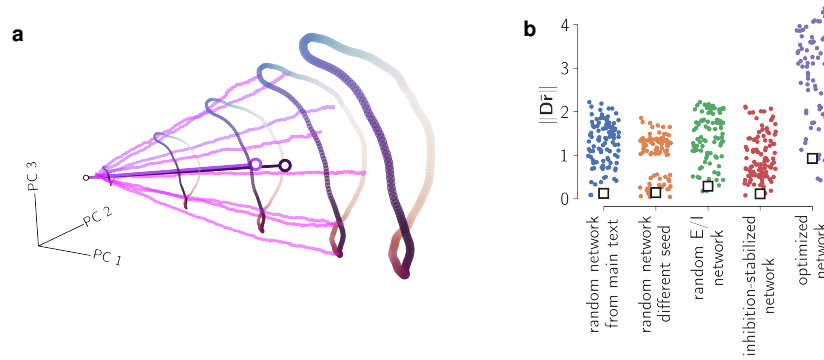


**Figure S2:** Analysis of WMP readout bias in the direction of  $\mathbf{D}\bar{\mathbf{r}}$ .

**a.** Simulated motor cortical responses in the calibration task, color-matched to the motor commands in fig. 3e driving these responses. These are plotted together with the same reachable manifold activity patterns from fig. 3f, projected onto the same three principal components. The open circles in the interior of this conical structure show the calibration task mean,  $\mathbf{c}$ , in light purple and the reachable manifold centroid,  $\bar{\mathbf{r}}$ , in dark purple, each connected to the origin by a line for visualization purposes. Note that, by definition, the calibration task neural responses at time  $t_{\text{end}} = 1000\text{ms}$  (the last point in each trajectory) lie almost exactly on the reachable manifold, slightly offset only because of noise in the response dynamics (see Methods Section 4.7).

**b.** Norm of  $\mathbf{D}\bar{\mathbf{r}}$  for each sampled WMP decoder,  $\mathbf{D}$ , for each simulated model motor cortical network (see Supplementary Materials Section S.1.1). Overlaid with an open black square is the norm of  $\mathbf{D}\bar{\mathbf{r}}$  for the baseline decoder of each corresponding simulation.

1379 decoder,  $\mathbf{D}\bar{\mathbf{r}} \approx \mathbf{0}$ , so the reachable readouts are centered at the origin despite equation 37 holding true.  
 1380 Because the baseline decoder is fit to predict the calibration task stimuli from the neural responses they  
 1381 elicit (Methods Section 4.8), by construction it ignores any directions of calibration task activity that  
 1382 do not provide information about the stimulus. One such direction is their mean,  $\mathbf{c} \approx a\bar{\mathbf{r}}$ . This can be  
 1383 appreciated from Supplementary Figure S2a, where it is evident that the trajectories of activity during  
 1384 different trials of the calibration task all evolve identically along this direction, despite being evoked  
 1385 by different stimuli. Thus, decoding from this direction is useless for decoding the stimulus identity,  
 1386 so the baseline decoder ignores it by spanning an orthogonal subspace. However, while this direction  
 1387 may not contain information about the calibration task stimuli, it does contain a lot of the variance of  
 1388 the calibration task neural responses. Consequently, it resides within the intrinsic manifold, and thus  
 1389 WMP's – which are essentially randomly oriented within the intrinsic manifold – are likely to be aligned  
 1390 with it by chance.

1391 This is confirmed empirically in fig. S2b, where we plot the norm of  $\mathbf{D}\bar{\mathbf{r}}$  for the baseline decoder  
 1392 and each of the sampled WMPs for each simulation we studied. The norm is evidently much higher for  
 1393 WMP decoders than for the baseline decoder in each simulation, explaining why the reachable readout  
 1394 bias manifests itself in WMP decoders but not in the baseline decoder.

### 1395 S.1.3 Non-negative firing rates are necessary to replicate biases in WMP learning

1396 Here we demonstrate that removing the non-negativity constraint on firing rates precludes our model  
 1397 from reproducing the behavioral biases in WMP reachable readouts. We test this by replacing the  
 1398 activation function with the identity function,  $\phi(x) = x$ , and repeating the analysis of fig. 4c to check if

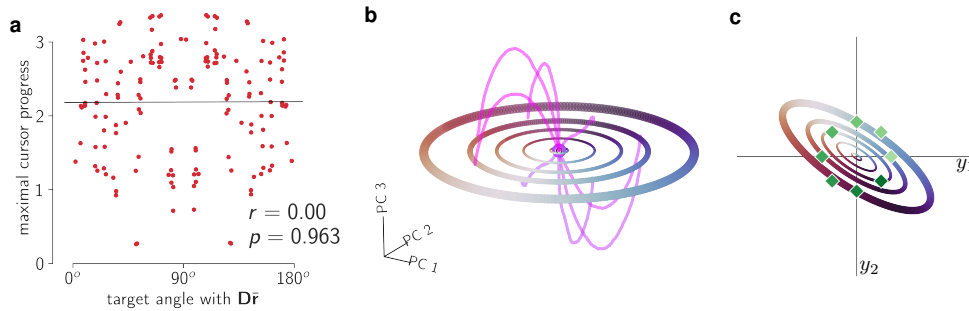


**Figure S3:** Removing the non-negativity constraint fails to reproduce experimentally observed biases in WMP learning. **a.** Maximal cursor progress in each target direction as a function of angle with  $D\bar{r}$ , for 20 sampled WMPs. Only 20 WMP's were used as we found that the intrinsic manifold of the linear network was only  $\ell = 5$ -dimensional, so we correspondingly adjusted the criteria for subsampling WMP's and OMP's (cf. Supplementary Materials Section S.3.3) and found that only 20 WMP's and 60 OMP's satisfied them. As was done in fig. 4c, the reachable manifold centroid,  $\bar{\mathbf{r}}$ , is estimated using simulated mean firing rates during baseline decoder control (see Methods Section 4.6). Maximal cursor progress was calculated exactly as in equation 6, following the same procedure as in the main text for selecting  $s_{\text{max}}$  (cf. Methods Section 4.4). A total of 8 target directions  $\times$  20 sampled WMPs = 160 points are plotted. **b.** Activity patterns in the reachable manifold at endpoint time  $t_{\text{end}} = 1000\text{ms}$ , with  $\tilde{K} = 2$  non-zero command variables. Calibration task responses to each of the eight radial reach stimuli are overlaid in shades of pink, following exactly the same conventions as in Supplementary Figure S2a. These  $N$ -dimensional activity patterns are projected onto the top two principal components of the reachable manifold (PC1 and PC2) and the orthogonal dimension capturing the most calibration task response variance (PC3). Because the network dynamics are linear, the reachable manifold is exactly  $\tilde{K} = 2$ -dimensional, so PC1 and PC2 capture 100% of the variance in activity patterns within it. The small open black circle at the center marks the origin of the state space. The light and dark purple open circles at the origin mark the calibration task mean  $\mathbf{c}$  the reachable manifold centroid  $\bar{\mathbf{r}}$  in purple, respectively. The latter is barely visible because they overlap almost completely. **c.** Readouts reachable through an example WMP, following the same color conventions as in fig. 3c. The green diamonds show the eight target readouts from the radial cursor reaching task.

1399 the maximal cursor progress under each WMP is highest in the direction of  $D\bar{r}$ . We find that they in  
 1400 fact are not (Supplementary Figure S3a)

1401 The reason why can again be gleaned from looking at the relationship between the reachable repertoire  
 1402 centroid,  $\bar{\mathbf{r}}$ , the mean calibration task response,  $\mathbf{c}$ . In this case, because firing rates are allowed to be  
 1403 negative, both the reachable manifold and the calibration task neural responses are centered near the  
 1404 origin, and thus the reachable readouts are as well (equation 36),

$$\bar{\mathbf{r}} \approx \mathbf{0}, \mathbf{c} \approx \mathbf{0} \Rightarrow \bar{\mathbf{y}} = \mathbf{D}(\bar{\mathbf{r}} - \mathbf{c}) \approx \mathbf{0}. \quad (38)$$

1405 We can see this empirically in Supplementary Figure S3b, where we plot a projection of the reachable  
 1406 manifold with the calibration task neural responses overlaid (analogous to Supplementary Figure S2a).  
 1407 We see that both are centered around the origin, with their means exactly on top of each other. The  
 1408 reachable readouts through a representative WMP are shown in Supplementary Figure S3c, illustrating  
 1409 the fact that they are consequently also centered at the origin. The maximal cursor progress is higher  
 1410 in some directions than in others (in this case in the NW and SE directions), but the bias is not  
 1411 unidirectional as it is in the model with non-negative firing rates (fig. 4a, fig. 4c) or in the experimental  
 1412 data (fig. 4d).

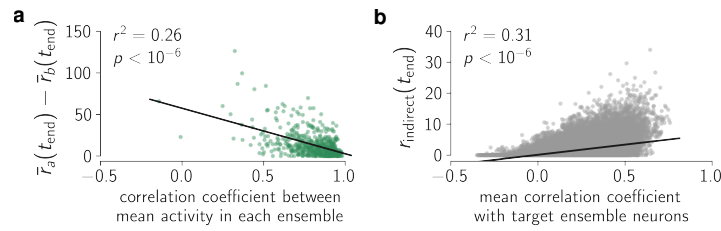


**Figure S4:** Operant conditioning of ensembles of 10 neurons by re-aiming.

**a.** Difference in ensembles' summed firing rates (at  $t_{\text{end}} = 1000$  ms) produced by the re-aiming solutions optimized for ensemble  $a$  being the target, for 500 randomly sampled ensembles of 10 neurons, plotted as a function of the correlation between the two ensembles' summed firing rates during simulated spontaneous behavior. Here,  $\bar{r}_a$  and  $\bar{r}_b$  denote the summed firing rates of neurons in ensemble  $a$  and  $b$ , respectively.

**b.** Activity of indirect neurons (at  $t_{\text{end}} = 1000$  ms) for the same ensembles and re-aiming solutions in previous panel, plotted as a function of mean correlation coefficient with neurons in ensemble  $a$  during simulated spontaneous behavior.

#### 1413 S.1.4 Operant conditioning of ensembles of neurons

1414 Clancy et al. (2014) conditioned ensembles of up to 10 neurons, rather than only pairs of neurons.  
1415 Here we repeat our simulations of operant conditioning but with a pair of target/distractor *ensembles*  
1416 of 10 neurons, rather than a pair of single neurons. We simulate re-aiming in exactly the same way via  
1417 equation 29, but where now the decoding vector  $\mathbf{d}$  is a vector with a +1 for each target ensemble neuron  
1418 and a -1 for each distractor ensemble neuron, and 0's everywhere else. Selection of neurons used for  
1419 operant conditioning and simulation of spontaneous behavior was done exactly as described in Methods  
1420 Section 4.10.

1421 We find that the main results from the main text are replicated in this setting as well: (1) the  
1422 correlation coefficient of ensembles' mean firing rates during simulated spontaneous behavior is corre-  
1423 lated with the difference in mean firing rates achieved by the optimal re-aiming solutions (Supplementary  
1424 Figure S4a); and (2) indirect neuron firing rates produced by these optimal re-aiming solutions are corre-  
1425 lated with their mean correlation coefficient with target ensemble neurons during simulated spontaneous  
1426 behavior (Supplementary Figure S4b).

#### 1427 S.1.5 Changes in modulation depth of motor cortical tuning curves

1428 In a study employing credit assignment rotation perturbations in a 3D cursor reaching task, it was ob-  
1429 served that both non-rotated and rotated neurons reduced their modulation depth after learning the  
1430 perturbed decoder, and that rotated neurons reduced their modulation depth more<sup>10</sup> (see text surround-  
1431 ing Methods Section 4.9, equation 26 for how modulation depth is defined and measured). Figure S5a  
1432 reveals that our model of generalized re-aiming does not reproduce this result, at least for the values of  
1433  $\tilde{K}$  we tested. Generalized re-aiming with up to 6 command variables seems to lead to slight *increases*  
1434 in the modulation depths of both rotated and non-rotated neurons, with marginal differences between  
1435 rotated and non-rotated neurons.

1436 While we did not simulate re-aiming with  $\tilde{K} > 6$  command variables in the context of credit as-



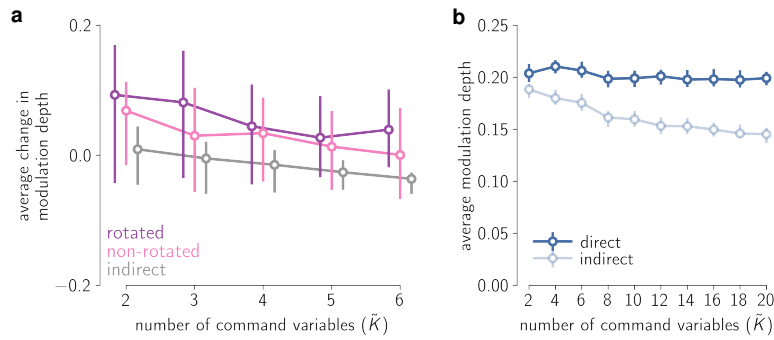


**Figure S5:** Changes in modulation depth under generalized re-aiming.

**a.** Average change in modulation depth of rotated, non-rotated, and indirect neurons between simulated reaches with the baseline decoder and each perturbed decoder, plotted as a function of the number of command variables used for re-aiming ( $\tilde{K}$ ). As in fig. 6e, the changes in modulation depth are averaged over all neurons in each sub-population, and the median over all 100 sampled credit assignment rotation perturbations is plotted. Error bars mark the upper and lower quartiles.

**b.** Average modulation depth of direct neurons (neurons recorded by the BCI, with non-zero decoding weights in **D**) and indirect neurons (neurons not recorded by the BCI) under generalized re-aiming solutions for OMP's. Modulation depths are averaged over all neurons in each sub-population, and the median over all 100 sampled OMP's is plotted. Error bars mark the upper and lower quartiles.

1437 signment rotation perturbations, we did simulate this in the context of OMP learning, where we found  
1438 that modulation depths of indirect neurons decreased as  $\tilde{K}$  increased (figure S5b). The fact that only  
1439 generalized re-aiming with a large number of command variables – but not regular re-aiming with only  
1440  $\tilde{K} = 2$  variables – can reproduce selective changes in modulation depth is consistent with the separate  
1441 observation that indirect neurons show selective decreases in modulation depth only after days of practice  
1442 with a given BCI decoder, but not within a single session.<sup>11</sup>

### 1443 S.1.6 Closed-loop feedback control

1444 All of the models we have considered so far are models of *open-loop* control: once the optimal motor  
1445 command is specified, it is used to drive the motor cortical population for the duration of the movement,  
1446 unchanged until the pre-specified endpoint time  $t_{\text{end}}$ . Any errors encountered along the way – either  
1447 due to noise or suboptimal motor commands – are thus ignored. A better strategy would be *closed-loop*  
1448 control, wherein errors observed via sensory feedback are used to adaptively modify the motor command  
1449 online. Under this strategy, errors that are encountered along the way can be corrected, thus improving  
1450 the accuracy of the desired BCI output. Such closed-loop feedback control strategies are well known to  
1451 be optimal in the presence of noise,<sup>12,13</sup> and substantial evidence exists that non-human primates utilize  
1452 them during BCI control.<sup>14–16</sup>

1453 In this section, we consider a re-aiming-based model of closed-loop feedback control in which the  
1454 motor command is continuously updated in response to sensory feedback. We evaluate this model on  
1455 the Sadtler et al. (2014) BCI learning task, and confirm that closed-loop re-aiming suffers from the same  
1456 limitations as open-loop re-aiming: the set of reachable activity patterns is limited by the number of  
1457 command variables used for control, such that OMP's cannot be learned with a small number of them.

1458 We assume an error feedback controller architecture of the following form,

$$\boldsymbol{\theta}(t; \mathbf{y}^*) = \mathbf{G}(\mathbf{y}^* - \mathbf{y}(t)) + \mathbf{b}, \quad (39)$$

1459 where the command variables,  $\boldsymbol{\theta}(t) = [\theta_1 \ \theta_2 \ \dots \ \theta_{\tilde{K}}]$ , vary continuously in time according to an  
1460 affine transformation of the instantaneous error,  $\mathbf{y}^* - \mathbf{y}(t)$ . As in the open-loop control simulations,  
1461 all additional command variables beyond the first  $\tilde{K}$  are fixed to 0. For simplicity, we assume a linear  
1462 encoding of the motor command in the upstream inputs,

$$\mathbf{u}(\boldsymbol{\theta}) = \mathbf{U}\boldsymbol{\theta}, \quad (40)$$

1463 For a given decoder,  $\mathbf{D}$ , we postulate that the subject learns a feedback controller,  $(\hat{\mathbf{G}} \in \mathbb{R}^{\tilde{K} \times 2}, \hat{\mathbf{b}} \in \mathbb{R}^{\tilde{K}})$ ,  
1464 that minimizes the following loss function:

$$\hat{\mathbf{G}}, \hat{\mathbf{b}} = \arg \min_{\mathbf{G}, \mathbf{b}} \frac{1}{8} \sum_{i=1}^8 \frac{1}{T} \int_0^T \|\mathbf{y}(t; \mathbf{G}, \mathbf{b}) - \mathbf{y}_i^*\|^2 dt + \gamma (\|\mathbf{b}\|^2 + \|\mathbf{G}\|_{\mathcal{F}}^2), \quad (41)$$

1465 where  $\mathbf{y}(t; \mathbf{G}, \mathbf{b})$  denotes the readout produced at time  $t$  under the closed-loop dynamics,  $\|\mathbf{G}\|_{\mathcal{F}}^2 =$   
1466  $\sum_{i=1}^{\tilde{K}} \sum_{j=1}^2 G_{ij}^2$  is the squared Frobenius norm, and  $\mathbf{y}_1^*, \dots, \mathbf{y}_8^*$  are the eight radial reach targets in the  
1467 BCI cursor control task. The time window of control was set to  $T = 1000$ ms.

1468 To compute  $\hat{\mathbf{G}}$  and  $\hat{\mathbf{b}}$ , we used gradient descent on the above loss function, using the Adam optimiza-  
1469 tion algorithm<sup>6</sup> with a initial learning rate of .01. To facilitate numerical optimization, deterministic  
1470 dynamics were used (no noise in the dynamics or in the initial conditions, which were fixed to 0). To  
1471 avoid poor local optima (which was often a problem with WMPs in particular), we ran gradient descent  
1472 from five different random initializations and used the best solution from these five runs.

1473 We computed  $(\hat{\mathbf{G}}, \hat{\mathbf{b}})$  for the randomly connected non-linear network analyzed in the main text  
1474 (equation 1), for each of the sampled baseline/WMP/OMP decoders used in the simulations presented  
1475 in the main text. For the baseline decoder we performed this optimization over multiple values of the  
1476 metabolic cost weight  $\gamma$  so as to identify the largest value of  $\gamma$  that permitted a time-averaged squared  
1477 error of less than .05 for all eight target readouts under this decoder (analogous to how  $\gamma$  was set in the  
1478 open-loop simulations in the main text, Methods Section 4.3). We then fixed  $\gamma$  to this value for all the  
1479 decoder perturbations.

1480 Simulations of cursor control with  $\tilde{K} = 2$  command variables are shown in Supplementary Figure S6a,  
1481 where we plot the mean squared error over target readouts as a function of time. Each trace corresponds  
1482 to the mean squared error achieved by the optimal feedback controller for a given decoder, with one  
1483 trace for the baseline decoder and one for each of the 100 sampled WMPs and OMPs. We find that for  
1484 almost all decoders, the mean squared error decreases to a certain level and remains low for the rest of

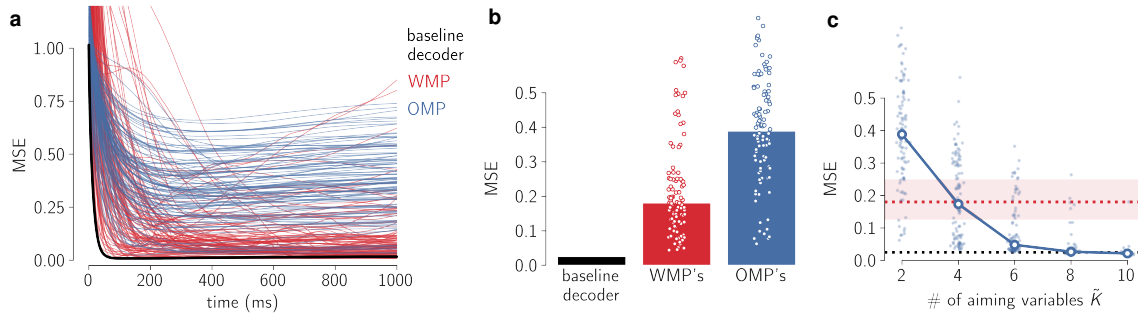


**Figure S6:** Closed-loop re-aiming reproduces the differences in WMP and OMP learning.

**a.** Mean squared error (mean over target readouts) achieved by closed loop control with  $\tilde{K} = 2$  command variables, as a function of time. Each line corresponds to performance on a different decoder, with a correspondingly optimized feedback controller,  $(\tilde{\mathbf{G}}, \tilde{\mathbf{b}})$  (equation 41).

**b.** Mean squared error (mean over target readouts and over time) achieved by error feedback controllers with  $\tilde{K} = 2$  command variables. Each point corresponds to a different decoder, with medians over all decoders in each class marked by the height of the bars.

**c.** Mean squared error (mean over target readouts and over time) achieved by error feedback controllers optimized for each OMP, with  $\tilde{K} = 2, 4, 6, 8,$  and  $10$  command variables. Light blue points denote this quantity for individual OMP's, larger open circles on top show the median. For reference, dotted horizontal lines show the mean squared error achieved by optimized error feedback with  $\tilde{K} = 2$  command variables for the baseline decoder (black) and WMP's (red); the red dotted line shows the median over all sampled WMP's with shading marking the upper and lower quartiles.

1485 this time window of 1000ms. However, this asymptotic error value is typically higher for OMP's than for  
 1486 WMP's (Supplementary Figure S6b), replicating the analogous result observed for the open-loop control  
 1487 model presented in the main text (fig. 3d).

1488 This again reflects the limitations of re-aiming with only  $\tilde{K} = 2$  command variables. In this case, this  
 1489 manifests itself in restricting how the error can be fed back into the network: the error gets mapped to  
 1490 a  $\tilde{K}$ -dimensional vector through equation 39 before being fed back into the network. As we saw occurs  
 1491 for the open-loop controller, this results in a restriction of how population activity can be modulated,  
 1492 making it difficult to generate the patterns of activity required to produce the target readouts under  
 1493 OMP's. Supplementary Figure S6c shows that these restrictions can be relaxed by increasing the number  
 1494 of command variables used for re-aiming,  $\tilde{K}$ . In this case, re-aiming with only  $\tilde{K} = 6$  command variables  
 1495 suffices to obtain a mean squared error less than 0.1 with OMP's. Interestingly, this is substantially less  
 1496 than the  $\tilde{K} > 10$  command variables that are necessary to achieve the same level of performance with  
 1497 open-loop re-aiming (fig. 5a).

## 1498 S.2 Mathematical derivations

### 1499 S.2.1 Scale-invariance of RNN dynamics with rectified linear activation function

1500 Here we prove that, whenever  $x_i(0) = 0$ ,

$$\forall s > 0 \quad \mathbf{r}(t; s\boldsymbol{\theta}) = s\mathbf{r}(t; \boldsymbol{\theta}), \quad (42)$$

1501 where  $\mathbf{r}(t; s\boldsymbol{\theta}) = \phi(\mathbf{x}(t; s\boldsymbol{\theta}))$  and  $\mathbf{x}(t; s\boldsymbol{\theta})$  is the solution to equation 1 with inputs defined by equation 2.

1502 The function  $\phi(\cdot)$  is the rectified linear activation function defined in equation 1.

1503 We begin by demonstrating that, when  $x_i(0) = 0$ ,

$$\forall s > 0 \quad \mathbf{x}(t; s\boldsymbol{\theta}) = s\mathbf{x}(t; \boldsymbol{\theta}). \quad (43)$$

We prove this by showing that the dynamics of  $s\mathbf{x}(t; \boldsymbol{\theta})$  are the same as those of  $\mathbf{x}(t; s\boldsymbol{\theta})$ :

$$\begin{aligned} \frac{d}{dt} [s\mathbf{x}(t; \boldsymbol{\theta})] &= s \frac{d}{dt} \mathbf{x}(t; \boldsymbol{\theta}) \\ &= -s\mathbf{x}(t; \boldsymbol{\theta}) + s\mathbf{W}^{\text{rec}} \phi(\mathbf{x}(t; \boldsymbol{\theta})) + s\mathbf{W}^{\text{in}} \phi(\mathbf{U}\boldsymbol{\theta}) \\ &= -s\mathbf{x}(t; \boldsymbol{\theta}) + \mathbf{W}^{\text{rec}} \phi(s\mathbf{x}(t; \boldsymbol{\theta})) + \mathbf{W}^{\text{in}} \phi(s\mathbf{U}\boldsymbol{\theta}) \quad \forall s > 0, \end{aligned} \quad (44)$$

1504 where in the second line we plugged in equation 1 and equation 2 for the dynamics and upstream inputs,

1505 respectively, and in the third line we used the scale-invariance of the rectified linear activation function,

$$\forall s \geq 0 \quad \phi(sx) = s\phi(x), \quad (45)$$

1506 It is easy to see that equation 44 exactly matches equation 1 but with  $s\mathbf{x}$  substituted in for  $\mathbf{x}$ ; that is,

1507 the dynamics of these two quantities are the same. Therefore, whenever the initial conditions match,

1508  $s\mathbf{x}(0; \boldsymbol{\theta}) = \mathbf{x}(0; s\boldsymbol{\theta})$ , then their trajectories will too. It is easy to see that this condition holds for any  $s$

1509 if  $x_i(0) = 0$ , thus proving equation 43.

1510 Along with the scale invariance of the activation function (equation 45), equation 43 implies equation

1511 42:

$$\mathbf{r}(t; s\boldsymbol{\theta}) = \phi(\mathbf{x}(t; s\boldsymbol{\theta})) = \phi(s\mathbf{x}(t; \boldsymbol{\theta})) = s\phi(\mathbf{x}(t; \boldsymbol{\theta})) = s\mathbf{r}(t; \boldsymbol{\theta}), \quad (46)$$

1512 thus completing our proof.

## 1513 S.2.2 Large $M$ limit of quadratic metabolic cost

1514 Here we derive the large  $M$  limit of the quadratic metabolic cost term in the remaining objective function

1515 (equation 4),

$$\lim_{M \rightarrow \infty} \frac{1}{M} \sum_{i=1}^M u_i(\boldsymbol{\theta})^2 \quad (47)$$

1516 We first note that each term in the sum depends on a sum over the randomly sampled encoding

1517 weights (equation 2),

$$u_i(\boldsymbol{\theta})^2 = \phi \left( \sum_{j=1}^K U_{ij} \theta_j \right)^2. \quad (48)$$

1518 If the encoding weights,  $U_{ij}$ , are independent and identically distributed, then each of the terms in this

1519 sum is also independent and identically distributed. By the law of large numbers, then, as  $M \rightarrow \infty$  their  
 1520 sum will approach an expectation over this distribution,

$$\lim_{M \rightarrow \infty} \frac{1}{M} \sum_{i=1}^M u_i(\boldsymbol{\theta})^2 = \langle u_i(\boldsymbol{\theta})^2 \rangle_{U_{ij}}, \quad (49)$$

1521 where  $\langle \cdot \rangle_{U_{ij}}$  denotes an expectation over the probability distribution of the encoding weights,  $U_{ij}$ .

1522 This expectation can be evaluated by first defining the random variable  $z = \sum_{j=1}^K U_{ij} \theta_j$  to express the  
 1523 expectation as an integral over  $z$ , and then exploiting the rectified linear activation function (equation  
 1524 1) to simplify this integral,

$$\langle u_i(\boldsymbol{\theta})^2 \rangle_{U_{ij}} = \langle \phi(z)^2 \rangle_z = \int_{-\infty}^{\infty} \phi(z)^2 p(z) dz = \int_{-\infty}^0 \phi(z)^2 p(z) dz + \int_0^{\infty} \phi(z)^2 p(z) dz = \int_0^{\infty} z^2 p(z) dz, \quad (50)$$

1525 where we simply exploited the fact that  $\phi(z) = 0$  when  $z < 0$  and  $\phi(z) = z$  when  $z \geq 0$ . If the distribution  
 1526 of the encoding weights  $U_{ij}$  is symmetric around 0, then the distribution of  $z$  is as well and we have that

$$\int_0^{\infty} z^2 p(z) dz = \frac{1}{2} \langle z^2 \rangle. \quad (51)$$

1527 Finally, if the encoding weights are zero-mean and independent, we have that

$$\langle z^2 \rangle = \sum_{j=1}^K \sum_{k=1}^K \langle U_{ij} U_{ik} \rangle \theta_j \theta_k = \sum_{j=1}^K \langle U_{ij}^2 \rangle \theta_j^2. \quad (52)$$

1528 If  $U_{ij}$  additionally have unit variance,  $\langle U_{ij}^2 \rangle = 1 \Rightarrow \langle z^2 \rangle = \|\boldsymbol{\theta}\|^2$ . Putting this all together, we arrive at  
 1529 the equality in equation 9:

$$\lim_{M \rightarrow \infty} \frac{1}{M} \sum_{i=1}^M u_i(\boldsymbol{\theta})^2 = \langle u_i(\boldsymbol{\theta})^2 \rangle_{U_{ij}} = \int_0^{\infty} z^2 p(z) dz = \frac{1}{2} \langle z^2 \rangle = \frac{\|\boldsymbol{\theta}\|^2}{2}. \quad (53)$$

### 1530 S.2.3 Reachable manifold moments for $\tilde{K} = 2$

1531 In our analysis of the reachable manifold, we characterized its location and shape via its centroid and  
 1532 covariance, which were evaluated as expectations over a uniform distribution on the manifold. Here we  
 1533 derive the probability density function of this distribution and use it to calculate these expectations.

1534 We begin with the case of  $\tilde{K} = 2$  non-zero command variables, which we parameterize by their polar  
 1535 coordinates,

$$\begin{bmatrix} \theta_1 \\ \theta_2 \end{bmatrix} = s \begin{bmatrix} \cos \varphi \\ \sin \varphi \end{bmatrix}. \quad (54)$$

1536 We then formally define the reachable manifold as follows:

$$\mathcal{R} = \{\mathbf{r}(t_{\text{end}}; s, \varphi) : s \in [0, s_{\text{max}}], \varphi \in [0, 2\pi]\}. \quad (55)$$

1537 where  $\mathbf{r}(t_{\text{end}}; s, \varphi)$  is the motor cortical activity pattern at time  $t_{\text{end}}$  produced by a pair of command  
 1538 variables  $\theta_1, \theta_2$  with angle  $\varphi$  and norm  $s$ , with all other command variables set to 0 ( $\theta_3 = \theta_4 = \dots =$   
 1539  $\theta_K = 0$ ). The function  $\mathbf{r}(t_{\text{end}}; s, \varphi)$  can be thought of as a function mapping 2D command variables,  
 1540  $(s, \varphi) \in [0, s_{\text{max}}] \times [0, 2\pi]$ , to activity patterns,  $\mathbf{r} \in \mathbb{R}^N$ , on the 2D surface constituting the reachable  
 1541 manifold (the conical surface shown in fig. 3f).

1542 The probability density function of the uniform distribution on this 2D surface in  $\mathbb{R}^N$  is given by its  
 1543 area element,  $dV(s, \varphi)$ , divided by its total area,

$$p(\mathbf{r}(t_{\text{end}}; s, \varphi)) = \frac{dV(s, \varphi)}{V}. \quad (56)$$

The area element and total area are given by

$$dV(s, \varphi) = \sqrt{\det[\mathbf{J}(s, \varphi)^T \mathbf{J}(s, \varphi)]} \quad (57)$$

$$V = \int_0^{s_{\text{max}}} \int_0^{2\pi} dV(s, \varphi) d\varphi ds, \quad (58)$$

1544 where  $\det[\cdot]$  denotes the matrix determinant and  $\mathbf{J}$  denotes the  $N \times 2$  Jacobian of the mapping from  
 1545 command variables to the reachable manifold,

$$\mathbf{J}(s, \varphi) = \begin{bmatrix} \frac{\partial}{\partial s} \mathbf{r}(t_{\text{end}}; s, \varphi) & \frac{\partial}{\partial \varphi} \mathbf{r}(t_{\text{end}}; s, \varphi) \end{bmatrix}. \quad (59)$$

1546 To evaluate the probability density function, we must first calculate these derivatives.

1547 To do so, we again resort to the scale invariance property of the rectified linear activation function  
 1548 (equation 45),

$$\mathbf{r}(t_{\text{end}}; s, \varphi) = s \underbrace{\mathbf{r}(t_{\text{end}}; 1, \varphi)}_{\mathbf{r}_0(\varphi)} := s \mathbf{r}_0(\varphi), \quad (60)$$

1549 where we have defined  $\mathbf{r}_0(\varphi)$  to be the activity generated by a pair of command variables with angle  $\varphi$   
 1550 and unit norm. The Jacobian is thus given by

$$\mathbf{J}(s, \varphi) = \begin{bmatrix} \mathbf{r}_0(\varphi) & s \mathbf{r}'_0(\varphi) \end{bmatrix} = \begin{bmatrix} \mathbf{r}_0(\varphi) & \mathbf{r}'_0(\varphi) \end{bmatrix} \begin{bmatrix} 1 & 0 \\ 0 & s \end{bmatrix}, \quad (61)$$

where  $\mathbf{r}'_0(\varphi) := \frac{\partial}{\partial \varphi} \mathbf{r}_0(\varphi)$ . Plugging this into equation 57, we have that the area element is given by

$$\begin{aligned}
 dV(s, \varphi) &= \sqrt{\det \begin{bmatrix} 1 & 0 \\ 0 & s \end{bmatrix} \det \begin{bmatrix} \mathbf{r}_0(\varphi)^T \\ \mathbf{r}'_0(\varphi)^T \end{bmatrix} \det \begin{bmatrix} \mathbf{r}_0(\varphi) & \mathbf{r}'_0(\varphi) \\ 1 & 0 \\ 0 & s \end{bmatrix}} \\
 &= \sqrt{\det \begin{bmatrix} 1 & 0 \\ 0 & s \end{bmatrix} \det \begin{bmatrix} \|\mathbf{r}_0(\varphi)\|^2 & \mathbf{r}_0(\varphi) \cdot \mathbf{r}'_0(\varphi) \\ \mathbf{r}_0(\varphi) \cdot \mathbf{r}'_0(\varphi) & \|\mathbf{r}'_0(\varphi)\|^2 \end{bmatrix} \det \begin{bmatrix} 1 & 0 \\ 0 & s \end{bmatrix}} \\
 &= s \sqrt{\|\mathbf{r}_0(\varphi)\|^2 \|\mathbf{r}'_0(\varphi)\|^2 - (\mathbf{r}_0(\varphi) \cdot \mathbf{r}'_0(\varphi))^2} \\
 &= s \|\mathbf{r}_0(\varphi)\| \|\mathbf{r}'_0(\varphi)\| \sqrt{1 - \cos^2 \omega(\varphi)} \\
 &= s \|\mathbf{r}_0(\varphi)\| \|\mathbf{r}'_0(\varphi)\| |\sin \omega(\varphi)|, \tag{62}
 \end{aligned}$$

where  $\omega(\varphi)$  is the angle between  $\mathbf{r}_0(\varphi)$  and its derivative at  $\varphi$ ,  $\mathbf{r}'_0(\varphi)$ . The total area of the manifold is thus

$$\begin{aligned}
 V &= \int_0^{s_{\max}} \int_0^{2\pi} s \|\mathbf{r}_0(\varphi)\| \|\mathbf{r}'_0(\varphi)\| |\sin \omega(\varphi)| d\varphi ds \\
 &= \frac{1}{2} s_{\max}^2 \int_0^{2\pi} \|\mathbf{r}_0(\varphi)\| \|\mathbf{r}'_0(\varphi)\| |\sin \omega(\varphi)| d\varphi. \tag{63}
 \end{aligned}$$

With these two expressions in hand, we can analytically express expectations over the probability density function in equation 56. The mean, corresponding to the manifold centroid,  $\bar{\mathbf{r}}$ , is given by

$$\begin{aligned}
 \bar{\mathbf{r}} &:= \int_0^{s_{\max}} \int_0^{2\pi} \mathbf{r}(t_{\text{end}}; s, \varphi) p(\mathbf{r}(t_{\text{end}}; s, \varphi)) ds d\varphi \\
 &= \int_0^{s_{\max}} \int_0^{2\pi} s \mathbf{r}_0(\varphi) p(\mathbf{r}(t_{\text{end}}; s, \varphi)) ds d\varphi \\
 &= \frac{1}{V} \int_0^{s_{\max}} s^2 ds \int_0^{2\pi} \mathbf{r}_0(\varphi) \|\mathbf{r}_0(\varphi)\| \|\mathbf{r}'_0(\varphi)\| |\sin \omega(\varphi)| d\varphi \\
 &= \frac{2}{3} s_{\max} \frac{\int_0^{2\pi} \mathbf{r}_0(\varphi) \|\mathbf{r}_0(\varphi)\| \|\mathbf{r}'_0(\varphi)\| |\sin \omega(\varphi)| d\varphi}{\int_0^{2\pi} \|\mathbf{r}_0(\varphi)\| \|\mathbf{r}'_0(\varphi)\| |\sin \omega(\varphi)| d\varphi} \tag{64}
 \end{aligned}$$

1551 Its covariance,  $\Sigma_r$ , is given by

$$\Sigma_r = \overline{\mathbf{r}\mathbf{r}^T} - \bar{\mathbf{r}}\bar{\mathbf{r}}^T, \tag{65}$$

where  $\overline{\mathbf{r}\mathbf{r}^T}$  is the matrix of second moments,

$$\begin{aligned}
 \overline{\mathbf{r}\mathbf{r}^T} &:= \int_0^{s_{\max}} \int_0^{2\pi} \mathbf{r}(t_{\text{end}}; s, \varphi) \mathbf{r}(t_{\text{end}}; s, \varphi)^T p(\mathbf{r}(t_{\text{end}}; s, \varphi)) \, ds \, d\varphi \\
 &= \int_0^{s_{\max}} \int_0^{2\pi} s^2 \mathbf{r}_0(\varphi) \mathbf{r}_0(\varphi)^T p(\mathbf{r}(t_{\text{end}}; s, \varphi)) \, ds \, d\varphi \\
 &= \frac{1}{V} \int_0^{s_{\max}} s^3 \, ds \int_0^{2\pi} \mathbf{r}_0(\varphi) \mathbf{r}_0(\varphi)^T \|\mathbf{r}_0(\varphi)\| \|\mathbf{r}'_0(\varphi)\| |\sin \omega(\varphi)| \, d\varphi \\
 &= \frac{1}{2} s_{\max}^2 \frac{\int_0^{2\pi} \mathbf{r}_0(\varphi) \mathbf{r}_0(\varphi)^T \|\mathbf{r}_0(\varphi)\| \|\mathbf{r}'_0(\varphi)\| |\sin \omega(\varphi)| \, d\varphi}{\int_0^{2\pi} \|\mathbf{r}_0(\varphi)\| \|\mathbf{r}'_0(\varphi)\| |\sin \omega(\varphi)| \, d\varphi} \tag{66}
 \end{aligned}$$

1552 Because the integrals and derivatives in these expressions are all univariate, we can estimate them  
 1553 accurately with discrete approximations.

#### 1554 S.2.4 Reachable manifold moments for $\tilde{K} > 2$

1555 Analogous expressions can be derived for the case of  $\tilde{K} > 2$ , but in these cases good estimates of the  
 1556 integrals and derivatives quickly become numerically intractable as the number of variables increases.  
 1557 For these cases, we therefore resorted to moments with respect to the probability distribution of activity  
 1558 patterns *generated by uniformly distributed motor commands*, instead of the probability distribution of  
 1559 activity patterns *uniformly distributed on the reachable manifold*.

We can express the covariance of this simpler distribution, which we denote by  $\Sigma_\theta$ , by parameterizing the non-zero command variables,  $\tilde{\boldsymbol{\theta}} = \begin{bmatrix} \theta_1 & \theta_2 & \dots & \theta_{\tilde{K}} \end{bmatrix}$ , in terms of a magnitude and direction,  $\tilde{\boldsymbol{\theta}} = s\tilde{\boldsymbol{\theta}}_0$ , where  $0 \leq s \leq s_{\max}$  and  $\|\tilde{\boldsymbol{\theta}}_0\| = 1$ . This allows us to factorize the uniform distribution over motor commands into a scalar uniform distribution for the magnitude,  $s \sim \text{Unif}[0, s_{\max}]$ , and a uniform distribution over the unit radius  $(\tilde{K} - 1)$ -sphere for the direction,  $\tilde{\boldsymbol{\theta}}_0$ . The expectations in the covariance thus factorize as follows:

$$\begin{aligned}
 \Sigma_\theta &= \left\langle \left\langle \mathbf{r}(t_{\text{end}}; s\tilde{\boldsymbol{\theta}}_0) \mathbf{r}(t_{\text{end}}; s\tilde{\boldsymbol{\theta}}_0)^T \right\rangle_s \right\rangle_{\tilde{\boldsymbol{\theta}}_0} - \left\langle \left\langle \mathbf{r}(t_{\text{end}}; s\tilde{\boldsymbol{\theta}}_0) \right\rangle_s \right\rangle_{\tilde{\boldsymbol{\theta}}_0} \left\langle \left\langle \mathbf{r}(t_{\text{end}}; s\tilde{\boldsymbol{\theta}}_0) \right\rangle_s \right\rangle_{\tilde{\boldsymbol{\theta}}_0}^T \\
 &= \langle s^2 \rangle_s \left\langle \mathbf{r}(t_{\text{end}}; \tilde{\boldsymbol{\theta}}_0) \mathbf{r}(t_{\text{end}}; \tilde{\boldsymbol{\theta}}_0)^T \right\rangle_{\tilde{\boldsymbol{\theta}}_0} - \langle s \rangle_s^2 \left\langle \mathbf{r}(t_{\text{end}}; \tilde{\boldsymbol{\theta}}_0) \right\rangle_{\tilde{\boldsymbol{\theta}}_0} \left\langle \mathbf{r}(t_{\text{end}}; \tilde{\boldsymbol{\theta}}_0) \right\rangle_{\tilde{\boldsymbol{\theta}}_0}^T \\
 &= \frac{s_{\max}^2}{3} \left\langle \mathbf{r}(t_{\text{end}}; \tilde{\boldsymbol{\theta}}_0) \mathbf{r}(t_{\text{end}}; \tilde{\boldsymbol{\theta}}_0)^T \right\rangle_{\tilde{\boldsymbol{\theta}}_0} - \frac{s_{\max}^2}{4} \left\langle \mathbf{r}(t_{\text{end}}; \tilde{\boldsymbol{\theta}}_0) \right\rangle_{\tilde{\boldsymbol{\theta}}_0} \left\langle \mathbf{r}(t_{\text{end}}; \tilde{\boldsymbol{\theta}}_0) \right\rangle_{\tilde{\boldsymbol{\theta}}_0}^T, \tag{67}
 \end{aligned}$$

1560 where we used the scale invariance of the motor cortical dynamics (equation 8) to write  $\mathbf{r}(t_{\text{end}}; s\tilde{\boldsymbol{\theta}}_0) =$   
 1561  $s\mathbf{r}(t_{\text{end}}; \tilde{\boldsymbol{\theta}}_0)$  in the second line, and in the third line we simply inserted expressions for the first and second  
 1562 moments of  $s$ . The expectations over  $\tilde{\boldsymbol{\theta}}_0$  can be approximated using Monte Carlo methods by uniformly  
 1563 sampling vectors from the corresponding unit radius  $(\tilde{K} - 1)$ -sphere.



### 1564 S.3 Extended methods

#### 1565 S.3.1 Estimating the intrinsic manifold

1566 To estimate the intrinsic manifold, we fit a Probabilistic PCA (PPCA) model<sup>17</sup> to the mixed and z-scored  
1567 calibration task responses (see Methods Section 4.8),

$$\mathbf{r}_i^{\text{mixed}} = \mathbf{S}_r^{-1} \mathbf{H}(\mathbf{r}_i - \mathbf{c}). \quad (68)$$

Here,  $i$  indexes a particular timestep and trial during the calibration task. The PPCA generative model assumes that each of these data points are generated from a corresponding set of  $\ell$  uncorrelated latent variables  $\mathbf{z}_i = \begin{bmatrix} z_{i1} & z_{i2} & \dots & z_{i\ell} \end{bmatrix}$  as follows,

$$\mathbf{z}_i \sim \mathcal{N}(\mathbf{0}, \mathbf{I}), \quad (69a)$$

$$\mathbf{r}_i^{\text{mixed}} | \mathbf{z}_i \sim \mathcal{N}(\mathbf{F}\mathbf{z}_i, \sigma^2 \mathbf{I}). \quad (69b)$$

The model thus assumes that the activity patterns  $\mathbf{r}_i^{\text{mixed}}$  are concentrated within the column space of the factor loading matrix  $\mathbf{F}$  – it is the columns of this matrix that define the intrinsic manifold. These parameters are fit to the mixed and z-scored calibration task data,  $\{\mathbf{r}_i^{\text{mixed}}\}$ , by maximum likelihood:

$$\begin{aligned} \mathbf{F}, \sigma^2 &= \arg \max_{\mathbf{F}, \sigma^2} \log P(\{\mathbf{r}_i^{\text{mixed}}\}) = \arg \max_{\mathbf{F}, \sigma^2} \log \mathcal{N}(\mathbf{0}, \mathbf{F}\mathbf{F}^T + \sigma^2 \mathbf{I}) \\ &\Rightarrow \mathbf{F} = \begin{bmatrix} \sqrt{\lambda_1 - \sigma^2} \mathbf{v}_1 & \sqrt{\lambda_2 - \sigma^2} \mathbf{v}_2 & \dots & \sqrt{\lambda_\ell - \sigma^2} \mathbf{v}_\ell \end{bmatrix} \\ &\Rightarrow \sigma^2 = \frac{1}{N_r - \ell} \sum_{i=\ell+1}^{N_r} \lambda_i, \end{aligned}$$

1568 where  $\lambda_1, \lambda_2, \dots, \lambda_{N_r}$  are the eigenvalues of the sample covariance of the calibration task activity,  $\{\mathbf{r}_i^{\text{mixed}}\}$ ,  
1569 ordered from largest to smallest (i.e.  $\lambda_1$  is the largest eigenvalue), and  $\mathbf{v}_1, \mathbf{v}_2, \dots, \mathbf{v}_{N_r}$  are their associated  
1570 eigenvectors (i.e. the principal components, ordered from most to least variance explained).

Note, however, that the columns of  $\mathbf{F}$  define the dimensions of the intrinsic manifold in mixed and z-scored neural activity space (i.e. the space defined by the coordinates of the  $\mathbf{r}_i^{\text{mixed}}$  vectors). To convert these to dimensions of the full  $N$ -dimensional state space, where each coordinate corresponds to the activity of an individual neuron (i.e. the space defined by the coordinates of the  $\mathbf{r}_i$  vectors), we invert equation 68 to obtain

$$\mathbf{r}_i = \mathbf{H}^{-1} \mathbf{S}_r \mathbf{r}_i^{\text{mixed}} + \mathbf{c},$$

where we define  $\mathbf{H}^{-1}$  as the  $N \times N_r$  matrix containing the inverse of the tri-diagonal component of  $\mathbf{H}$  in its first  $N_r$  rows and 0's filling all subsequent rows. We then apply this linear transformation to the

columns of  $\mathbf{F}$  to obtain an analogous  $N \times \ell$  factor loading matrix  $\mathbf{F}_r$  defined in the full  $N$ -dimensional state space,

$$\mathbf{F}_r = \mathbf{H}^{-1} \mathbf{S}_r \mathbf{F}.$$

1571 Note that, since the bottom  $N - N_r$  rows of  $\mathbf{H}^{-1}$  are filled with 0's, those same rows of  $\mathbf{F}_r$  are also filled  
 1572 with 0's. This reflects the fact that the intrinsic manifold is orthogonal to the dimensions of activity  
 1573 corresponding to neurons not recorded in the experiment. Finally, we defined an orthonormal basis  
 1574  $\mathbf{f}_1, \mathbf{f}_2, \dots, \mathbf{f}_\ell \in \mathbb{R}^N$  for the intrinsic manifold by taking the left singular vectors of  $\mathbf{F}_r$ . These are the  
 1575 vectors used in equation 25 for figure 3g.

1576 This method for estimating the intrinsic manifold is almost the same as that used by Sadtler et al.,  
 1577 which differs only in that a Factor Analysis model was used instead of a PPCA model. In that case, the  
 1578 maximum likelihood estimates of the model parameters cannot be evaluated in closed form and must be  
 1579 computed via an iterative optimization algorithm (the Expectation Maximization algorithm). We found  
 1580 that using a Factor Analysis model instead of PPCA had no noticeable effects on our results (data not  
 1581 shown), so we reported only results with the more easily fit PPCA model.

### 1582 S.3.2 Construction of the baseline decoder

As described in the Methods section, the baseline decoder has the following form

$$\mathbf{D}_0^{\text{base}} = \mathbf{K} \mathbf{L}$$

$$\mathbf{K} \in \mathbb{R}^{2 \times \ell}, \quad \mathbf{L} \in \mathbb{R}^{\ell \times N_r}.$$

1583 We term  $\mathbf{L}$  the *dimensionality reduction matrix* and  $\mathbf{K}$  the *velocity readout matrix*. Here we describe in  
 1584 greater detail how these two matrices are fit to the calibration task data. Unless otherwise noted, these  
 1585 procedures are exactly as those described in<sup>18</sup> and<sup>19</sup>

The dimensionality reduction matrix  $\mathbf{L}$  is derived from the mode of the posterior distribution of the PPCA model (equation 69),

$$P(\mathbf{z}_i | \mathbf{r}_i^{\text{mixed}}) = \mathcal{N}(\mathbf{z}_i | \boldsymbol{\mu}_{\mathbf{z}_i | \mathbf{r}_i^{\text{mixed}}}, \boldsymbol{\Sigma}_{\mathbf{z}_i | \mathbf{r}_i^{\text{mixed}}}) \quad (70a)$$

$$\boldsymbol{\mu}_{\mathbf{z}_i | \mathbf{r}_i^{\text{mixed}}} = \underbrace{(\mathbf{F}^T \mathbf{F} + \sigma^2 \mathbf{I})^{-1} \mathbf{F}^T}_{\hat{\mathbf{L}}} \mathbf{r}_i^{\text{mixed}}. \quad (70b)$$

1586 The  $N_r \times \ell$  matrix  $\hat{\mathbf{L}}$  thus yields a linear transformation from  $N_r$  dimensions to  $\ell$  dimensions. The  $z$ -  
 1587 scored and mixed activity patterns  $\{\mathbf{r}_i^{\text{mixed}}\}$  from the calibration task can thus be reduced to  $\ell$  dimensions  
 1588 via multiplication with  $\hat{\mathbf{L}}$ , resulting in a corresponding set of dimensionality-reduced activity patterns  
 1589  $\{\hat{\mathbf{z}}_i\}$  (as above, here and in the rest of this section the index  $i$  jointly indexes a timestep and trial of the

1590 calibration task).

1591 To complete the construction of the dimensionality reduction matrix  $\mathbf{L}$ , these dimensionality-reduced  
 1592 activity patterns are then z-scored. The standard deviations of each component of the  $\hat{\mathbf{z}}_i$  vectors are  
 1593 calculated over all timesteps and trials of the calibration task, and collected in a diagonal matrix  $\mathbf{S}_z$ .  
 1594 Note that mean subtraction is not necessary since the activity vectors  $\mathbf{r}_i^{\text{mixed}}$  have already been z-scored  
 1595 so are mean 0. The final dimensionality reduction matrix is then given by

$$\mathbf{L} = \mathbf{S}_z^{-1} \hat{\mathbf{L}} \quad (71)$$

1596 This second z-scoring step is necessary to ensure that controlling the BCI does not require neurons to  
 1597 produce firing rates beyond the range exhibited during the calibration task.

1598 The dimensionality reduction matrix used by Sadtler et al. differed from ours in that  $\hat{\mathbf{L}}$  was con-  
 1599 structed from the posterior distribution under a Factor Analysis generative model, rather than a PPCA  
 1600 generative model. Like in PPCA, the mode of the posterior distribution of a Factor Analysis model can  
 1601 also be expressed as a linear transformation of  $\mathbf{r}_i^{\text{mixed}}$ , yielding a very similar expression for  $\hat{\mathbf{L}}$ .

The velocity readout matrix  $\mathbf{K}$  is also chosen by maximum likelihood fit of a generative model. In  
 this case, we assume that the z-scored dimensionality-reduced activity patterns from the calibration task,  
 $\hat{\mathbf{z}}_i^{\text{z-scored}} = \mathbf{L} \mathbf{r}_i^{\text{mixed}}$ , depend on the observed cursor velocities,  $\mathbf{y}_i$ , via the following latent Gaussian state  
 space model,

$$\begin{aligned} \mathbf{y}_i | \mathbf{y}_{i-1} &\sim \mathcal{N}(\mathbf{y}_{i-1}, \mathbf{Q}) \\ \hat{\mathbf{z}}_i^{\text{z-scored}} | \mathbf{y}_i &\sim \mathcal{N}(\mathbf{B} \mathbf{y}_i, \mathbf{R}) \end{aligned}$$

where  $i-1$  indexes the previous timestep in the same trial. Note that the cursor velocities  $\mathbf{y}_i$  are constant  
 within each trial of the calibration task, so within a given trial  $\mathbf{y}_i = \mathbf{y}_{i-1}$ . As was done in the original  
 experiment of Sadtler et al., we set

$$\mathbf{Q} = 2k^2 \mathbf{I},$$

where  $k = 1/.15$  denotes the ratio of the cursor speeds used in our simulation ( $\|\mathbf{y}_i\| = 1$ ) and the cursor  
 speeds used in the original experiment ( $\|\mathbf{y}_i\| = .15$  m/s). Maximum likelihood estimates of the remaining  
 parameters are given by

$$\begin{aligned} \mathbf{B} &= \left( \sum_i \hat{\mathbf{z}}_i^{\text{z-scored}} \mathbf{y}_i^T \right) \left( \sum_i \mathbf{y}_i \mathbf{y}_i^T \right)^{-1} \\ \mathbf{R} &= \frac{1}{T} \sum_i \hat{\mathbf{z}}_i^{\text{z-scored}} \hat{\mathbf{z}}_i^{\text{z-scored}T} - \hat{\mathbf{z}}_i^{\text{z-scored}} (\mathbf{B} \mathbf{y}_i)^T \end{aligned}$$

1602 where  $T$  denotes the total number of data points in the calibration task data: the number of timesteps

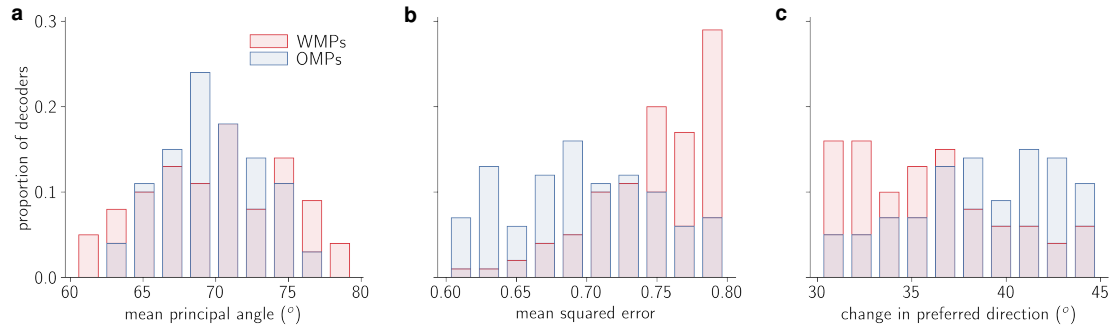


**Figure S7:** Differences between sampled decoder perturbations and the baseline decoder.

**a.** Distribution of mean principal angle between row space of baseline decoder and row space of each perturbed decoder.  
**b.** Distribution of mean squared error achieved by mean calibration task responses under each perturbed decoder.  
**c.** Distribution of minimal absolute change in preferred direction needed to produce the same readouts with each perturbed decoder as with the baseline decoder.

1603 in each trial times the total number of trials.

The velocity readout matrix is then derived from the mode of the of the posterior distribution  $P(\mathbf{y}_i | \hat{\mathbf{z}}_i^{z\text{-scored}}, \hat{\mathbf{z}}_{i-1}^{z\text{-scored}}, \hat{\mathbf{z}}_{i-2}^{z\text{-scored}}, \dots)$ , where the ellipses go back to the first timestep of the given trial. We use the posterior distribution at steady state, whose mode is given by

$$\hat{\mathbf{y}}_i = (\mathbf{I} - \mathbf{K}\mathbf{B}) \hat{\mathbf{y}}_{i-1} + \mathbf{K} \hat{\mathbf{z}}_i^{z\text{-scored}},$$

1604 where  $\mathbf{K}$  is the so-called steady-state Kalman gain matrix. This matrix is given by

$$\mathbf{K} = \Sigma_{ss} \mathbf{B}^T (\mathbf{B} \Sigma_{ss} \mathbf{B}^T + \mathbf{R})^{-1} \quad (72)$$

where  $\Sigma_{ss}$  is the steady-state posterior covariance, given by the solution to the discrete-time algebraic Riccati equation

$$\mathbf{0} = \Sigma_{ss} \mathbf{B}^T (\mathbf{B} \Sigma_{ss} \mathbf{B}^T + \mathbf{R})^{-1} \mathbf{B} \Sigma_{ss} - \mathbf{Q}$$

1605 The  $2 \times \ell$  velocity readout matrix used for the baseline decoder is thus set to the steady-state Kalman  
 1606 gain matrix,  $\mathbf{K}$ .

### 1607 S.3.3 Subsampling WMPs and OMPs

1608 As mentioned in the methods, we attempted to minimize any differences between within- and outside-  
 1609 manifold perturbations that would go beyond their opposing relationship to the intrinsic manifold. To do  
 1610 this, we first calculated every possible WMP and OMP, corresponding to each  $\ell$ -dimensional permutation.  
 1611 Since we set  $\ell = 8$ , this resulted in  $\ell! - 1 = 40,319$  decoder perturbations of each type (minus 1 to exclude  
 1612 the identity permutation). We then quantified how different each of these perturbations were from the  
 1613 baseline decoder with three different metrics, and eliminated all decoder perturbations for which one or  
 1614 more of these metrics fell outside a specific range.

1615 The first metric is the angle between the perturbed decoder's row space and the baseline decoder's.  
 1616 For each decoder perturbation,  $\mathbf{D}_0^{\text{WMP}}$  or  $\mathbf{D}_0^{\text{OMP}}$ , we calculated the two principal angles<sup>20</sup> between its row  
 1617 space and that of the baseline decoder effective decoding matrix,  $\mathbf{D}_0^{\text{base}}$ , and averaged these two angles.  
 1618 Any decoder perturbations for which this mean principal angle was greater than  $80^\circ$  or less than  $60^\circ$  was  
 1619 eliminated (fig. S7a).

The second metric is the mean squared error that would be achieved if the subject were to simply reproduce the neural activity from the calibration task. Analogous to the procedure followed by Sadtler et al., we averaged the calibration task responses over time and over trials for each reach target,

$$\bar{\mathbf{r}}_j^{\text{calib}} = \langle \mathbf{r}_i \rangle_{i \in \text{time points in calibration task trials with reach target } j}$$

1620 and then computed the readouts from these time- and trial- averaged firing rate vectors under each  
 1621 decoder perturbation,  $\mathbf{D}_0^{\text{WMP}}$  or  $\mathbf{D}_0^{\text{OMP}}$ . We then discarded all decoder perturbations where the mean  
 1622 squared error between these readouts and the target readouts was greater than 0.8 or less than 0.6 (fig.  
 1623 S7b).

The third metric is to ask how much the mean calibration task responses would have to change to produce the same readouts under the perturbed decoder as under the baseline decoder. We first calculated the time- and trial- averaged z-scored and mixed firing rates from the calibration task

$$\bar{\mathbf{r}}_j^{\text{mixed}} = \mathbf{S}_r^{-1} \mathbf{H}(\bar{\mathbf{r}}_j^{\text{calib}} - \mathbf{c}).$$

For each perturbed decoder,  $\tilde{\mathbf{D}}_0 = \mathbf{D}_0^{\text{WMP}}$  or  $\mathbf{D}_0^{\text{OMP}}$ , we then computed the activity patterns closest to  $\bar{\mathbf{r}}_j^{\text{mixed}}$  that would produce the same readouts through that decoder as the original activity patterns would through the baseline decoder,  $\mathbf{D}_0^{\text{base}}$ ,

$$\begin{aligned} \hat{\mathbf{r}}_j^{\text{mixed}}(\tilde{\mathbf{D}}_0) &= \arg \min_{\mathbf{r}} \|\mathbf{r} - \bar{\mathbf{r}}_j^{\text{mixed}}\|^2 \quad \text{subject to} \quad \tilde{\mathbf{D}}_0 \mathbf{r} = \mathbf{D}_0^{\text{base}} \bar{\mathbf{r}}_j^{\text{mixed}} \\ &= \bar{\mathbf{r}}_j^{\text{mixed}} + \tilde{\mathbf{D}}_0^T (\tilde{\mathbf{D}}_0 \tilde{\mathbf{D}}_0^T)^{-1} (\mathbf{D}_0^{\text{base}} - \tilde{\mathbf{D}}_0) \bar{\mathbf{r}}_j^{\text{mixed}}. \end{aligned}$$

1624 We then quantified the difference between  $\bar{\mathbf{r}}_j^{\text{mixed}}$  and  $\hat{\mathbf{r}}_j^{\text{mixed}}(\tilde{\mathbf{D}}_0)$  by fitting tuning curves and asking how  
 1625 much the preferred direction changed. Tuning curves were fit by least-squares regression, exactly as  
 1626 described in Methods Section 4.9 equation 26 (but with  $\bar{\mathbf{r}}_j^{\text{mixed}}$  or  $\hat{\mathbf{r}}_j^{\text{mixed}}(\tilde{\mathbf{D}}_0)$  plugged in for  $\bar{\mathbf{r}}_j$ ), and  
 1627 preferred directions were extracted from the fitted tuning weights as described in that section. For each  
 1628 decoder perturbation, we then computed the mean absolute difference of the preferred directions of the  
 1629 computed activity patterns  $\{\hat{\mathbf{r}}_j^{\text{mixed}}(\tilde{\mathbf{D}}_0)\}_{j=1}^8$  from those of the observed calibration task mean responses  
 1630  $\{\bar{\mathbf{r}}_j^{\text{mixed}}\}_{j=1}^8$ . Any perturbed decoders that resulted in a mean absolute difference of more than  $45^\circ$  or less  
 1631 than  $30^\circ$  were discarded (fig. S7c).

1632 We typically found that about 100-200 permutations out all possible decoder perturbations satisfied  
1633 these criteria. We then randomly sampled 100 of them. The distributions of these three metrics for the  
1634 100 sampled WMPs and OMPs used in the main text are shown in figures [S7a](#), [S7b](#), and [S7c](#).

## 1635 References

- 1636 [1] Guillaume Hennequin, Tim P. Vogels, and Wulfram Gerstner. “Non-Normal Amplification in Ran-  
1637 dom Balanced Neuronal Networks”. In: **Phys. Rev. E** 86.1 (July 2012), p. 011909. DOI: [10.1103/  
1638 PhysRevE.86.011909](https://doi.org/10.1103/PhysRevE.86.011909). (Visited on 04/15/2020).
- 1639 [2] Guillaume Hennequin, Tim P. Vogels, and Wulfram Gerstner. “Optimal Control of Transient Dy-  
1640 namics in Balanced Networks Supports Generation of Complex Movements”. en. In: **Neuron** 82.6  
1641 (June 2014), pp. 1394–1406. ISSN: 0896-6273. DOI: [10.1016/j.neuron.2014.04.045](https://doi.org/10.1016/j.neuron.2014.04.045).
- 1642 [3] David Sussillo et al. “A Neural Network That Finds a Naturalistic Solution for the Production of  
1643 Muscle Activity”. In: **Nature Neuroscience** 18.7 (July 2015), pp. 1025–1033. ISSN: 1546-1726.  
1644 DOI: [10.1038/mn.4042](https://doi.org/10.1038/mn.4042). (Visited on 04/22/2020).
- 1645 [4] E. Todorov and W. Li. “Optimal Control Methods Suitable for Biomechanical Systems”. In: **Pro-  
1646 ceedings of the 25th Annual International Conference of the IEEE Engineering in  
1647 Medicine and Biology Society (IEEE Cat. No.03CH37439)**. Vol. 2. Sept. 2003, 1758–1761  
1648 Vol.2. DOI: [10.1109/IEMBS.2003.1279748](https://doi.org/10.1109/IEMBS.2003.1279748).
- 1649 [5] Ta-Chu Kao, Mahdiah S. Sadabadi, and Guillaume Hennequin. “Optimal Anticipatory Control as  
1650 a Theory of Motor Preparation: A Thalamo-Cortical Circuit Model”. en. In: **Neuron** 109.9 (May  
1651 2021), 1567–1581.e12. ISSN: 0896-6273. DOI: [10.1016/j.neuron.2021.03.009](https://doi.org/10.1016/j.neuron.2021.03.009).
- 1652 [6] Diederik P. Kingma and Jimmy Ba. “Adam: A Method for Stochastic Optimization”. In: **arXiv:1412.6980**  
1653 [**cs**] (Jan. 2017). arXiv: [1412.6980 \[cs\]](https://arxiv.org/abs/1412.6980). (Visited on 03/13/2021).
- 1654 [7] Friedrich Schuessler et al. “The Interplay between Randomness and Structure during Learning in  
1655 RNNs”. In: **Advances in Neural Information Processing Systems**. Vol. 33. Curran Asso-  
1656 ciates, Inc., 2020, pp. 13352–13362. (Visited on 01/26/2024).
- 1657 [8] Francesca Mastroggiuseppe and Srdjan Ostojic. “Linking Connectivity, Dynamics, and Computa-  
1658 tions in Low-Rank Recurrent Neural Networks”. In: **Neuron** 99.3 (Aug. 2018), 609–623.e29. ISSN:  
1659 0896-6273. DOI: [10.1016/j.neuron.2018.07.003](https://doi.org/10.1016/j.neuron.2018.07.003). (Visited on 01/24/2020).
- 1660 [9] Laureline Logiaco, L. F. Abbott, and Sean Escola. “Thalamic Control of Cortical Dynamics in a  
1661 Model of Flexible Motor Sequencing”. en. In: **Cell Reports** 35.9 (June 2021), p. 109090. ISSN:  
1662 2211-1247. DOI: [10.1016/j.celrep.2021.109090](https://doi.org/10.1016/j.celrep.2021.109090).

- 1663 [10] Beata Jarosiewicz et al. “Functional Network Reorganization during Learning in a Brain-Computer  
1664 Interface Paradigm”. In: **Proceedings of the National Academy of Sciences** 105.49 (Dec.  
1665 2008), pp. 19486–19491. ISSN: 0027-8424, 1091-6490. DOI: [10.1073/pnas.0808113105](https://doi.org/10.1073/pnas.0808113105). (Visited on  
1666 02/04/2020).
- 1667 [11] Karunesh Ganguly et al. “Reversible Large-Scale Modification of Cortical Networks during Neu-  
1668 roprosthetic Control”. In: **Nature Neuroscience** 14.5 (May 2011), pp. 662–667. ISSN: 1546-1726.  
1669 DOI: [10.1038/nn.2797](https://doi.org/10.1038/nn.2797). (Visited on 04/13/2020).
- 1670 [12] Huibert Kwakernaak and Raphael Sivan. **Linear Optimal Control Systems**. Vol. 1. Wiley-  
1671 interscience New York, 1972.
- 1672 [13] Emanuel Todorov and Michael I. Jordan. “Optimal Feedback Control as a Theory of Motor Coordi-  
1673 nation”. en. In: **Nature Neuroscience** 5.11 (Nov. 2002), pp. 1226–1235. ISSN: 1546-1726. DOI:  
1674 [10.1038/nn963](https://doi.org/10.1038/nn963).
- 1675 [14] Matthew D Golub, Byron M Yu, and Steven M Chase. “Internal Models for Interpreting Neu-  
1676 ral Population Activity during Sensorimotor Control”. In: **eLife** 4 (Dec. 2015). Ed. by Timothy  
1677 Behrens, e10015. ISSN: 2050-084X. DOI: [10.7554/eLife.10015](https://doi.org/10.7554/eLife.10015). (Visited on 01/21/2020).
- 1678 [15] Sergey D. Stavisky et al. “Motor Cortical Visuomotor Feedback Activity Is Initially Isolated  
1679 from Downstream Targets in Output-Null Neural State Space Dimensions”. In: **Neuron** 95.1  
1680 (July 2017), 195–208.e9. ISSN: 0896-6273. DOI: [10.1016/j.neuron.2017.05.023](https://doi.org/10.1016/j.neuron.2017.05.023). (Visited on  
1681 04/28/2020).
- 1682 [16] Maryam M. Shanechi et al. “Rapid Control and Feedback Rates Enhance Neuroprosthetic Con-  
1683 trol”. In: **Nature Communications** 8.1 (Jan. 2017), p. 13825. ISSN: 2041-1723. DOI: [10.1038/  
1684 ncomms13825](https://doi.org/10.1038/ncomms13825). (Visited on 10/27/2020).
- 1685 [17] Michael E. Tipping and Christopher M. Bishop. “Probabilistic Principal Component Analysis”. In:  
1686 **Journal of the Royal Statistical Society: Series B (Statistical Methodology)** 61.3 (1999),  
1687 pp. 611–622. ISSN: 1467-9868. DOI: [10.1111/1467-9868.00196](https://doi.org/10.1111/1467-9868.00196). (Visited on 11/12/2020).
- 1688 [18] Patrick T. Sadtler et al. “Neural Constraints on Learning”. In: **Nature** 512.7515 (Aug. 2014),  
1689 pp. 423–426. ISSN: 1476-4687. DOI: [10.1038/nature13665](https://doi.org/10.1038/nature13665). (Visited on 02/13/2020).
- 1690 [19] Matthew D. Golub et al. “Learning by Neural Reassociation”. In: **Nature Neuroscience** 21.4  
1691 (Apr. 2018), pp. 607–616. ISSN: 1546-1726. DOI: [10.1038/s41593-018-0095-3](https://doi.org/10.1038/s41593-018-0095-3). (Visited on  
1692 11/11/2019).
- 1693 [20] Ake Björck and Gene H. Golub. “Numerical Methods for Computing Angles between Linear Sub-  
1694 spaces”. en. In: **Mathematics of Computation** 27.123 (1973), pp. 579–594. ISSN: 0025-5718,  
1695 1088-6842. DOI: [10.1090/S0025-5718-1973-0348991-3](https://doi.org/10.1090/S0025-5718-1973-0348991-3).